

UCLA

UCLA Electronic Theses and Dissertations

Title

The Study of Mechanical Properties of Cells as a Biomarker for Cancer Diagnostics

Permalink

<https://escholarship.org/uc/item/36f9678t>

Author

Tse, Henry Tat Kwong

Publication Date

2012

Peer reviewed|Thesis/dissertation

UNIVERSITY OF CALIFORNIA

Los Angeles

The Study of Mechanical Properties of Cells as a
Biomarker for Cancer Diagnostics

A dissertation submitted in partial satisfaction
of the requirements for the degree
Doctor of Philosophy in Biomedical Engineering

by

Henry Tat Kwong Tse

2012

© Copyright by
Henry Tat Kwong Tse

2012

ABSTRACT OF THE DISSERTATION

The Study of Mechanical Properties of Cells as a
Biomarker for Cancer Diagnostics

by

Henry Tat Kwong Tse

Doctor of Philosophy in Biomedical Engineering

University of California, Los Angeles, 2012

Professor Dino Di Carlo, Chair

The measurement of cellular mechanical properties can be impactful in many areas of biosciences due to the interdependencies of mechanics and cell state or function. Mechanical cues communicated via mechanosensing and mechanotransduction can regulate cellular behavior leading to biochemical and structural modifications; conversely, native cellular processes such as differentiation, activation, and malignant transformation triggered by biochemical cues have also shown to elicit significant changes to the cellular architecture. Measurement of these mechanical biophysical changes can therefore be used to infer cell state or function. To date, there are numerous approaches used to measure the mechanical properties of cells for biophysics research, yet these are limited in their translational ability as general research or clinical tools. The biggest challenges facing successful translation of these mechanical phenotyping tools are due to the technological complexity, manual sample handling and preparation requirements, and limited

sample throughput. This dissertation focuses on developing a high-throughput, label-free alternative for mechano phenotyping termed *deformability cytometry*. For the first time in the biophysics field, the *deformability cytometry* platform achieves throughputs of more than 1,000 cells/second; a rate that is three orders of magnitude greater than previous techniques. Additionally, initial work involving platform validation and proof-of-concept applications for stem cell differentiation, leukocyte activation, and cancer diagnostics are explored. The dissertation also undertakes a major engineering challenge of this system - large dataset image processing - which has led to the development of process efficient image analysis algorithms to increase the utility and robustness of this mechano phenotyping technique. Lastly, a clinical proof-of-concept study consisting of 119 patient pleural effusion samples were collected and assayed using the *deformability cytometry* platform to determine the diagnostic performance of mechanical biomarkers for malignant effusions. Briefly, the result of this clinical study achieved an area-under-the-curve of 0.91 with sensitivity and specificity of 100% and 69%, respectively. The high diagnostic accuracy combined with the ease-of-use, minimal sample preparations needs, and large sample sizes, satisfies many translational hurdles for a label-free mechano phenotyping platform for applications in the biosciences community.

The dissertation of Henry Tat Kwong Tse is approved.

Jianyu Rao

Michael Alan Teitell

Benjamin M. Wu

Dino Di Carlo, Committee Chair

University of California, Los Angeles

2012

DEDICATION

Elaine, Mom and Dad

TABLE OF CONTENTS

Abstract of the Dissertation	ii-iii
Committee Page	iv
Dedication	v
Table of Contents	vi
Acknowledgements	vii-ix
Vita	x-xii
Chapter 1	1-11
<i>Cell Mechanics: Origins and the Motivation Towards Mechano Phenotyping</i>	
Chapter 2	
<i>Increased Asymmetric and Multi-daughter Cell Division in Mechanically Confined Microenvironments</i>	
	12-35
Chapter 3	
<i>Hydrodynamic Stretching of Single Cells for Large Population Mechanical Phenotyping</i>	
	36-84
Chapter 4	
<i>Strategies for Implementing Hardware Assisted High-throughput Image Analysis</i>	
	85-108
Chapter 5	
<i>Mechano Phenotyping for the Diagnosis of Malignant Pleural Effusions</i>	
	109-143

ACKNOWLEDGEMENTS

Chapter 1

This chapter is an adaptation and expansion of the introduction sections of Chapters 2 and 3.

Dr. Elaine Wang edited this chapter.

Chapter 2

Increased asymmetric and multi-daughter cell division in mechanically confined

microenvironments has been reprinted with minor adaptations with permission from (Tse HTK, Weaver WM, and Di Carlo D (2012) Increased asymmetric and multi-daughter cell division in mechanically confined microenvironments. Public Library of Science ONE. DOI:

10.1371/journal.pone.0038986.) Copyright (2012) Public Library of Science. H.T.K.T, W.M.W, AND D.D.C. designed research; H.T.K.T. and W.M.W. performed research and analyzed data; H.T.K.T. W.M.W, AND D.D.C. wrote the paper. Professor Dino Di Carlo is the principal investigator of this work.

Chapter 3

Hydrodynamic stretching of single cells for large population mechanical phenotyping has been reprinted with minor adaptations with permission from (Gossett DR, Tse HTK, Lee SA, Ying Y, Lindgren AG, Yang OO, Rao J, Clark AT, and Di Carlo D (2012) Hydrodynamic stretching of single cells for large population mechanical phenotyping. *Proceedings of the National Academy of Sciences USA*. DOI:10.1073/pnas.1200107109.) Copyright (2012) National Academy of Sciences, USA. D.R.G., H.T.K.T., O.O.Y., J.R., A.T.C., and D.D.C. designed research; D.R.G., H.T.K.T., S.A.L., Y.Y., and A.G.L. performed research; O.O.Y., J.R., and A.T.C. contributed

new reagents/analytic tools; D.R.G., H.T.K.T., S.A.L., Y.Y., A.G.L., O.O.Y., J.R., A.T.C., and D.D.C. analyzed data; and D.R.G., H.T.K.T., S.A.L., O.O.Y., J.R., A.T.C., and D.D.C. wrote the paper. Professor Dino Di Carlo is the principal investigator of this work. This project received funds from the Eli and Edythe Broad Center of Regenerative Medicine and Stem Cell Research (A.T.C.), the David and Lucile Packard Foundation Fellowship (D.D.C.), and a Defense Advanced Research Projects Agency Young Faculty Award (D.D.C.).

Chapter 4

Strategies for implementing hardware assisted high-throughput image analysis has been reprinted with minor adaptations with permission from (Tse HTK, Meng P, Gossett DR, Irturk A, Kastner R, Di Carlo D (2011) Strategies for implementing hardware assisted high-throughput image analysis. *Journal of Laboratory Automation* 16(6):422-430 doi:10.1016/j.jala.2011.08.001.) Copyright (2012) Sage Journals, USA. H.T.K.T., P.M., D.R.G., A.I., R.K., and D.D.C. designed research; H.T.K.T., P.M., D.R.G., and A.I. performed research; H.T.K.T., P.M., D.R.G., A.I., R.K., and D.D.C. wrote the paper.

Chapter 5

Mechanophenotyping for diagnosis of malignant pleural effusions is a version of work in preparation for publication by Henry Tat Kwong Tse, Daniel R. Gossett, Yong Ying, Kimberley Mislick, Jianyu Rao, and Dino Di Carlo. Professor Dino Di Carlo is the principal investor of this work. This work is supported by the David and Lucile Packard Foundation Fellowship (D.D.C.), and a Defense Advanced Research Projects Agency Young Faculty Award (D.D.C.).

Additional Acknowledgements:

I am grateful for the support of the following people in engaging intellectual discussions in research as well as building lifelong friendships on this journey of science:

Professor Dino Di Carlo, Dr. Daniel R. Gossett, Dr. Soojung Claire Hur, Westbrook Weaver, Hamed Amini, Albert J. Mach, Mahdokht Masaeli, Coleman Murray, Dr. Elodie Sollier, Professor Wonhee Lee, Dr. Oladunni Adeyiga, Dr. Aram Chung, Dr. Anja Kunze, Dr. Peter Tseng, Dr. Michael Masterman-Smith, James Che, Janay Kong, Dianne Pulido, Patrick Sandoz, Jaideep Dudani, Derek Go, Andy Lee, and other Di Carlo lab affiliates past, present, and future.

Lastly, I am incredibly thankful for the support of my family:

Chiu Sim Chan, Wai Ching Tse, James Tse, Brandee Tran Ma, and Dr. Elaine Wang for their always uplifting words and acts of encouragement.

VITA

Education

University of California Los Angeles, Los Angeles, CA Sep. 2008 - June 2011
Henry Samueli School of Engineering and Applied Sciences (HSSEAS)
Biomedical Engineering Interdepartmental Program
Master of Science

University of California San Diego, La Jolla, CA Sep. 2004 - June 2008
Jacobs School of Engineering
Bioengineering: Biotechnology
Bachelor of Science

Publications

Journal Publications

Gossett DR*, **Tse HTK***, Lee S, Ying Y, Lindgren, AG, Yang OO, Rao J, Clark AT, Di Carlo D. Hydrodynamic stretching of single cells for large population mechanical phenotyping. **Proceedings of the National Academy of Sciences USA** (2012); 109(20):7630-7635 doi: 10.1073/pnas.1200107109. *First Authors

Tse HTK*, Weaver WM*, Di Carlo D. Increased asymmetric and multi-daughter cell division in mechanically confined microenvironments. **Public Library of Science ONE** (2012); 7(6) doi: 10.1371/journal.pone.0038986. *First Authors

Tse HTK, Meng P, Gossett DR, Irturk A, Kastner R, Di Carlo D. Strategies for implementing hardware-assisted high-throughput cellular image analysis. **Journal of Laboratory Automation** (2011); 16(6):422-430 doi:10.1016/j.jala.2011.08.001.

Hur SC, **Tse HTK**, Di Carlo D. Sheathless inertial cell ordering for extreme through flow cytometry. **Lab on a Chip** (2010); 10:274-280 doi:10.1039/B919495A.

Gossett DR, **Tse HTK**, Dudani JS, Goda K, Woods TA, Graves SW, Di Carlo D. Inertial manipulation and transfer of microparticles across laminar fluid streams. **Small** (2012); doi: 10.1002/smll.201200588.

Gossett DR, Weaver WM, Mach AJ, Hur SC, **Tse HTK**, Lee W, Amini H, Di Carlo D. Label-free cell separation and sorting in microfluidic systems. **Analytical and Bioanalytical Chemistry** (2010); 397(8):3249-67 doi:10.1007/s00216-010-3721-9.

Publication in Submission

Tse HTK, Gossett DR, Ying Y, Mislick K, Rao J, Di Carlo D. Mechanophenotyping for diagnosis of malignant pleural effusions.

Book Chapter

Di Carlo D, **Tse HTK**, Gossett DR. "Introduction: why analyze single cells?" Methods in Molecular Biology: Single-cell analysis Editor: S. Lindstrom, H. Andersson-Svahn. New York: Springer, 2012. 853(1-10). DOI: 10.1007/978-1-61779-567-1_1.

Patents

Di Carlo D, Ozcan A, Bahram J, Hur S, **Tse HTK**. Inertial particle focusing flow cytometer. Patent number: US/2012/0063664; 13/231,570 (signee: Erin Bowers).

Di Carlo D, Gossett DR, **Tse HTK**. Method and device for high throughput deformability measurements. Patent number: WO/2012/040067; 61/385,268 (signee: Michael S. Davidson).

Proceedings

Tse HTK, Gossett DR, and Di Carlo, D. Deformability cytometry: Applications in clinical cancer diagnostics. **Oral Presentation. MicroTAS 2011.** Seattle, WA. October 2011.

Tse HTK, Gossett DR, Lee S, Clark AT, Di Carlo D. A novel, high-Throughput, single-Cell deformability measurement technique for diagnostics and therapeutics. **Oral Presentation. Biomedical Engineering Society Annual Meeting.** Austin, TX. October 2010.

Tse HTK, Weaver WM, Di Carlo D. Confined microenvironments on tumor cell behavior. **Poster Presentation. Biomedical Engineering Society Annual Meeting.** Pittsburgh PA. September 2009.

Gossett DR, **Tse HTK**, Dudani J, and Di Carlo, D. High-Throughput Cellular Sample Preparation Via Ultrafast Solution Exchange. **Oral Presentation. MicroTAS 2011.** Seattle, WA. October 2011.

Gossett DR, **Tse HTK**, Lee S, Clark AT, Di Carlo D. Deformability cytometry: High-throughput, continuous measurement of cell mechanical properties in extensional flow. **Oral Presentation. MicroTAS 2010.** Groningen, Netherlands. October 2010. Cited by 3.

Gossett DR, **Tse HTK**, Lee S, Adeyiga O, Yang O, Clark AT, Di Carlo D. Clinical applications of high-throughput single-cell deformability measurements. **Poster Presentation. Biomedical Engineering Society Annual Meeting.** Hartford, CT. October 2011.

Gossett DR, **Tse HTK**, Lee S, Clark AT, Di Carlo D. A powerful new high-throughput tool for measuring the deformability of single cells. **Oral Presentation. Gordon-Kenan Research Seminar on the Physics and Chemistry of Microfluidics.** Waterville Valley, NH. June 2011.

Gossett DR, **Tse HTK**, Lee S, Clark AT, Di Carlo D. A powerful new high-throughput tool for measuring the deformability of single cells. **Poster Presentation. Laboratory Automation.** Palm Springs, CA. January 2011.

Gossett DR, **Tse HTK**, Dudani J, and Di Carlo D. High-throughput, continuous, millisecond, solution exchange for particle suspensions. **Oral Presentation. American Physical Society's Division of Fluid Dynamics (DFD).** Long Beach, CA. November 2010.

Chapter 1

Cell Mechanics: Origins and the Motivation Towards Mechano Phenotyping

The knowledge in the field of cell biology is largely contributed by the research of understanding complex biochemical networks and observation of its biochemical response. While biochemical reactions are of immense importance in cell biology, cells are not isolate reaction pots. Cells are physical entities where the presence of structural mechanics is evident. Indeed, cellular structural architecture have shown to be integral parts both in dictating and facilitating biological processes^{1,2}.

Cellular components such as tubulin, actin, and intermediate filaments are known contributors to the overall structural mechanics of a cell. Recent research reveals additional roles in cellular processes such as intra-cellular transport, mechanical sensing and transduction, motility, and facilitating cell cycle proceses³⁻⁹. For example, regulation of the cycle depends on the constant production and degradation of proteins and the activation or deactivation of the complexes responsible for targeting these proteins for degradation via ubiquitination. While environmental cues such as soluble factors have long been implicated in the cell cycle control system, the past decade has revealed a new perspective based on mechanical cues, adding another dimension to our understanding of the cell as a whole. Consideration of both soluble and mechanical cues will be necessary to gain a more thorough comprehension of cell biology and the cell cycle. Mechanosensing is an important component in the physiology of the cell and tissue homeostasis. Direct linkages between the extracellular matrix (ECM) and the intracellular environment allow external mechanical cues to alter the cellular state and structural architecture

in response¹⁰⁻¹². Conversely, these same linkages enable the cell to transmit forces extracellularly, altering the mechanical micro-environment itself¹³. This mechanical balance can result in cellular differentiation^{2,14-16}, morphological modifications^{17,18} and motility changes^{18,19}, as well as alterations in cell cycle control²⁰.

Structural and mechanical modifications in cellular processes

Structural changes of cells can be indicative of the cell state or function. Native cellular processes, such as differentiation of stem cells²¹ and extravasation of lymphocytes¹⁸, or non-native processes, such as intravasation in malignant progression²², have recently been discovered to undergo massive structural changes upon changes in the cell state or function. For instance, the process of successful stem cell differentiation is highly dependent on regulation of lamins A/C and B²³. Lamins, intermediate filament proteins, create a mesh network of structural and organizational support to the nuclear envelope, where only lamin B is found in undifferentiated stem cells. Upon differentiation, stem cells increase transcription level of lamin A/C which increases rigidity of the nuclei²¹. This structural modification to the nucleus contributes to the silencing of pluripotency genes and the maintenance of its differentiated state. Other native processes, such as lymphocyte extravasation, also elicit structural reorganization. Lymphocytes are continuously circulating in the blood vessels and thus require sufficient rigidity for protection from damage in circulation. However, upon activation by a signaling chemokine, a rapid conversion from a rigid architecture to a highly deformable state allows for extravasation through the endothelial cells to the injury site. This activation processes involves cytoskeletal reorganization of microfilaments, microtubules, and intermediate filaments¹⁸ to enable migration as well as evidence for nuclear changes needed for gene transcription and differentiation²⁴. This

change from a rigid sphere to a highly deformable state exemplifies where mechanical properties can be used as a predictor of cell state. The mechanical changes seen in extravasation of lymphocytes can also be envisioned to play a similar role in the malignant transformation of tumors during intravasate and extravasate events. Establishing a measure of malignancy or tumor progression could be instrumental for treatment decisions.

Influences of microenvironment mechanics on cellular behavior

The recent developments in cancer biology on the existence and relevance of 'stem-cell like cancer cells' or cancer stem cells is controversial^{25,26}. This is due to numerous reports for evidence of rare, self-renewing, cancer progenitors subpopulations existing in tumors²⁷⁻³⁰ and equal number of reports against the rarity of the cancer stem cell population³¹, and whether "terminally differentiated cancer cells" are locked into this fate or can spontaneously return to stem-like cancer cells^{32,33}. As such, the cancer biology field is at a deadlock about these conflicting cancer stem cells reports. A major challenge in cancer stem cell biology is finding effective stem-like biomarkers to identify cancer stem cells. Currently, the markers used are biochemical labels adopted from traditional stem cell biology markers including: Oct3/4, Nanog, CD133, nestin, Bmi-1, and c-kit³⁴. As these markers are analyzed by flow cytometry, the variability between samples - but more importantly between research groups - due to the inherent relativity of intensity based label biochemical markers (and batch to batch label variations) ultimately leads to a limited value of these markers in cancer stem cell identification. Interestingly, recent work examining culturing tumors spheroids in soft mechanical environment to enrich for tumorigenic cancer stem cell populations have had success³⁴. By using soft mechanical environment on tumor spheroid, spheroid cells were notably softer with increased

traction forces when compared to control cells. These phenotypic and biophysical changes are similar to stem-cell spheroids, but lack expression of conventional stem-cell biochemical markers. Along a similar trajectory, the second chapter in the dissertation is focused on exploring mechanical stresses of tumor microenvironments at the single-cell level in generating mechanically unstable cells. This work aims to further the understanding of the interactions of mechanical microenvironment cues affecting inherently mechanical cellular processes.

Biophysics research tools to probe mechanical properties of cells

Over the past decade, enormous advances in our understanding of the importance of mechanical sensitivity and responsiveness of cells has led to the rapid development of biophysical research tools to measure and interpret these mechanical changes. In the 1930s, initial biophysical experiments by Harvey and Danielli first used methods such as centrifugation, plate compression, capillary aspiration, and sessile drops to study surface tension and viscosity of cells³⁵. In the last 20 years, a wide variety of biophysical measurement platforms have been engineered to perform mechanical measurements on cells³⁶. Generally, these analysis techniques can be divided into two categories based on the samples they act on: bulk and single-cell³⁷. Bulk platforms, such as microfiltration, tend to have high throughput at the cost of [being unable to elucidate cellular function/state], yielding only one endpoint measurement without taking into account heterogeneity or size differences within the sample population of cells. Single-cell platforms that can assay this heterogeneity, but at lower throughputs, include micropipette aspiration³⁸, atomic force microscopy (AFM)³⁹, magnetic bead-based rheology, microfluidic optical stretching⁴⁰, and biophysical flow cytometry³⁷. The rapid development of these biophysical tools has led to numerous scientific findings associating cellular mechanical

properties to different cell states including metastatic potential³⁹⁻⁴¹, mechanics of stem cell differentiation^{15,38}, and leukocyte activation⁴². Clinically, a measure of malignancy and metastatic potential in tissues or biological fluids could guide treatment decisions, while a measure of the degree of differentiation could prevent transplantation of undifferentiated, tumorigenic stem cells in regenerative therapies. For drug discovery and personalized medicine, a simple measure of cytoskeletal integrity could allow screening for cytoskeletal-acting drugs or evaluation of cytoskeletal drug resistance in biopsied samples. Additionally, measures of leukocyte activation are strong predictors of disease prognosis and response to treatment in persons with HIV-1 infection⁴³ or rejection of allografts⁴⁴. As the application areas are broad, biophysical mechanical markers are poised to potentially be impactful biomarkers as cell identifiers indicative of disease for applications in general research and clinical settings.

Biophysical techniques (specifically mechanical-properties-based measurement tools) are primed to have significant impact in both research and clinical settings. The attractiveness of biophysical measurements such as surface tension, viscosity, impedance, density, volume, mass, and mechanical stiffness is that these are intrinsic physical properties. These measurements are absolute as opposed to relative values (i.e. fluorescent intensity of a biochemical labeled marker). This readily enables creating universal standards without the need to recalibrate as is required for label-based biochemical detection; this advantage could lead to the development of highly efficient techniques. However, given the limited dynamic range of intrinsic physical properties compared to fluorescent intensity-based biochemical labels, it is unlikely that biophysical tools will have the same level of specificity as conventional flow cytometry. Yet, given a defined problem universe, biophysical measurements can potentially have the same or better sensitivity while realizing benefits of time, cost, and accuracy advantages.

Research need: An alternative high-throughput label-free mechanophenotyping platform

A simple, label-free, mechanical measurement in which cells are minimally handled has the potential to greatly reduce costs and allow routine cell screening and classification in clinical and research applications. Current cell deformability measurements have been too low throughput or inconsistent to have a significant clinical impact. Further, disease may develop from abnormalities in a single cell³⁷ or small subset, such that accurately detecting rare events or small populations is important, and bulk measurement may result in misleading averages⁴⁵. Yet, current single cell techniques, usually optimized for biophysics research, operate at low rates from 1 cell/min (AFM and optical stretching) to ~1-5 cells/sec (biophysical flow cytometry, electroporative flow cytometry⁴⁶). For the translation of mechanical properties based biomarkers, a need exists for a high-throughput single-cell approach. Further, a clinically applicable platform will require simple operations, rapid assays, and quick data turnover. These needs are further explored and addressed in the subsequent chapters.

Bibliography

1. Wang, N., Butler, J. P. & Ingber, D. E. (1993). Mechanotransduction across the cell surface and through the cytoskeleton. *Science* 260:1124–1127. DOI:10.1126/science.7684161
2. Engler, A. J., Sen, S., Sweeney, H. L. & Discher, D. E. (2006). Matrix Elasticity Directs Stem Cell Lineage Specification. *Cell* 126:677–689. DOI:10.1016/j.cell.2006.06.044
3. Houben, F., Ramaekers, F. C. S., Snoeckx, L. H. E. H. & Broers, J. L. V. (2007). Role of nuclear lamina-cytoskeleton interactions in the maintenance of cellular strength. *Biochimica et Biophysica Acta (BBA) - Molecular Cell Research* 1773:675–686. DOI:10.1016/j.bbamcr.2006.09.018
4. Compton, D. A. (2000). Spindle Assembly in Animal Cells. *Annual Review of Biochemistry* 69:95–114. DOI:10.1146/annurev.biochem.69.1.95
5. Hirokawa, N., Noda, Y. & Okada, Y. (1998). Kinesin and dynein superfamily proteins in organelle transport and cell division. *Current Opinion in Cell Biology* 10:60–73. DOI:10.1016/S0955-0674(98)80087-2
6. Helfand, B. T., Chang, L. & Goldman, R. D. (2004). Intermediate filaments are dynamic and motile elements of cellular architecture. *J Cell Sci* 117:133–141. DOI:10.1242/jcs.00936
7. Chang, L. & Goldman, R. D. (2004). Intermediate filaments mediate cytoskeletal crosstalk. *Nature Reviews Molecular Cell Biology* 5:601–613. DOI:10.1038/nrm1438
8. Stamenović, D. (2005). Microtubules may harden or soften cells, depending of the extent of cell distension. *Journal of Biomechanics* 38:1728–1732. DOI:10.1016/j.jbiomech.2004.07.016
9. Gardel, M. L., Shin, J. H., MacKintosh, F. C., Mahadevan, L., Matsudaira, P. & Weitz, D. A. (2004). Elastic Behavior of Cross-Linked and Bundled Actin Networks. *Science* 304:1301–1305. DOI:10.1126/science.1095087
10. Shyy, J. Y.-J. & Chien, S. (2002). Role of integrins in endothelial mechanosensing of shear stress. *Circ. Res* 91:769–775
11. Bershadsky, A. D., Balaban, N. Q. & Geiger, B. (2003). Adhesion-dependent cell mechanosensitivity. *Annu. Rev. Cell Dev. Biol* 19:677–695. DOI:10.1146/annurev.cellbio.19.111301.153011

12. Ingber, D. E. (2008). Can cancer be reversed by engineering the tumor microenvironment? *Semin Cancer Biol* 18:356–364. DOI:10.1016/j.semcancer.2008.03.016
13. Lelièvre, S. A., Weaver, V. M., Nickerson, J. A., Larabell, C. A., Bhaumik, A., Petersen, O. W. & Bissell, M. J. (1998). Tissue phenotype depends on reciprocal interactions between the extracellular matrix and the structural organization of the nucleus. *PNAS* 95:14711–14716
14. Kilian, K. A., Bugarija, B., Lahn, B. T. & Mrksich, M. (2010). Geometric cues for directing the differentiation of mesenchymal stem cells. *Proc. Natl. Acad. Sci. U.S.A* 107:4872–4877. DOI:10.1073/pnas.0903269107
15. Chowdhury, F., Na, S., Li, D., Poh, Y.-C., Tanaka, T. S., Wang, F. & Wang, N. (2010). Material properties of the cell dictate stress-induced spreading and differentiation in embryonic stem cells. *Nat Mater* 9:82–88. DOI:10.1038/nmat2563
16. Gilbert, P. M. *et al.* (2010). Substrate Elasticity Regulates Skeletal Muscle Stem Cell Self-Renewal in Culture. *Science* 329:1078–1081. DOI:10.1126/science.1191035
17. Kumar, S. & Weaver, V. M. (2009). Mechanics, malignancy, and metastasis: The force journey of a tumor cell. *Cancer Metastasis Rev* 28:113–127. DOI:10.1007/s10555-008-9173-4
18. Brown, M. J., Hallam, J. A., Colucci-Guyon, E. & Shaw, S. (2001). Rigidity of Circulating Lymphocytes Is Primarily Conferred by Vimentin Intermediate Filaments. *J Immunol* 166:6640–6646
19. Alexander, N. R., Branch, K. M., Parekh, A., Clark, E. S., Iwueke, I. C., Guelcher, S. A. & Weaver, A. M. (2008). Extracellular matrix rigidity promotes invadopodia activity. *Curr Biol* 18:1295–1299. DOI:10.1016/j.cub.2008.07.090
20. Assoian, R. K. & Klein, E. A. (2008). Growth control by intracellular tension and extracellular stiffness. *Trends Cell Biol* 18:347–352. DOI:10.1016/j.tcb.2008.05.002
21. Pajerowski, J. D., Dahl, K. N., Zhong, F. L., Sammak, P. J. & Discher, D. E. (2007). Physical Plasticity of the Nucleus in Stem Cell Differentiation. *PNAS* 104:15619–15624. DOI:10.1073/pnas.0702576104

22. Kedrin, D., van Rheenen, J., Hernandez, L., Condeelis, J. & Segall, J. (2007). Cell Motility and Cytoskeletal Regulation in Invasion and Metastasis. *Journal of Mammary Gland Biology and Neoplasia* 12:143–152. DOI:10.1007/s10911-007-9046-4
23. Constantinescu, D., Gray, H. L., Sammak, P. J., Schatten, G. P. & Csoka, A. B. (2006). Lamin A/C Expression Is a Marker of Mouse and Human Embryonic Stem Cell Differentiation. *STEM CELLS* 24:177–185. DOI:10.1634/stemcells.2004-0159
24. Festenstein, R., Pagakis, S. N., Hiragami, K., Lyon, D., Verreault, A., Sekkali, B. & Kioussis, D. (2003). Modulation of Heterochromatin Protein 1 Dynamics in Primary Mammalian Cells. *Science* 299:719–721. DOI:10.1126/science.1078694
25. Gupta, P. B., Chaffer, C. L. & Weinberg, R. A. (2009). Cancer stem cells: mirage or reality? *Nature Medicine* 15:1010–1012. DOI:10.1038/nm0909-1010
26. Shipitsin, M. & Polyak, K. (2008). The cancer stem cell hypothesis: in search of definitions, markers, and relevance. *Laboratory Investigation* 88:459–463. DOI:10.1038/labinvest.2008.14
27. Bonnet, D. & Dick, J. E. (1997). Human acute myeloid leukemia is organized as a hierarchy that originates from a primitive hematopoietic cell. *Nature Medicine* 3:730–737. DOI:10.1038/nm0797-730
28. Schmidt, P., Kopecky, C., Hombach, A., Zigrino, P., Mauch, C. & Abken, H. (2011). Eradication of melanomas by targeted elimination of a minor subset of tumor cells. *PNAS* 108:2474–2479. DOI:10.1073/pnas.1009069108
29. Civenni, G. *et al.* (2011). Human CD271-Positive Melanoma Stem Cells Associated with Metastasis Establish Tumor Heterogeneity and Long-term Growth. *Cancer Res* 71:3098–3109. DOI:10.1158/0008-5472.CAN-10-3997
30. Dieter, S. M. *et al.* (2011). Distinct Types of Tumor-Initiating Cells Form Human Colon Cancer Tumors and Metastases. *Cell Stem Cell* 9:357–365. DOI:10.1016/j.stem.2011.08.010
31. Quintana, E., Shackleton, M., Sabel, M. S., Fullen, D. R., Johnson, T. M. & Morrison, S. J. (2008). Efficient tumour formation by single human melanoma cells. *Nature* 456:593–598. DOI:10.1038/nature07567

32. Gupta, P. B., Fillmore, C. M., Jiang, G., Shapira, S. D., Tao, K., Kuperwasser, C. & Lander, E. S. (2011). Stochastic State Transitions Give Rise to Phenotypic Equilibrium in Populations of Cancer Cells. *Cell* 146:633–644. DOI:10.1016/j.cell.2011.07.026
33. Chaffer, C. L. *et al.* (2011). Normal and neoplastic nonstem cells can spontaneously convert to a stem-like state. *PNAS* 108:7950–7955. DOI:10.1073/pnas.1102454108
34. Liu, J. *et al.* (2012). Soft fibrin gels promote selection and growth of tumorigenic cells. *Nature Materials* 11:734–741. DOI:10.1038/nmat3361
35. Harvey, E. N. & Danielli, J. F. (1938). PROPERTIES OF THE CELL SURFACE. *Biological Reviews* 13:319–341. DOI:10.1111/j.1469-185X.1938.tb00520.x
36. Kim, D.-H., Wong, P. K., Park, J., Levchenko, A. & Sun, Y. (2009). Microengineered Platforms for Cell Mechanobiology. *Annu. Rev. Biomed. Eng.* 11:203–233. DOI:10.1146/annurev-bioeng-061008-124915
37. Rosenbluth, M. J., Lam, W. A. & Fletcher, D. A. (2008). Analyzing cell mechanics in hematologic diseases with microfluidic biophysical flow cytometry. *Lab Chip* 8:1062. DOI:10.1039/b802931h
38. Pajerowski, J. D., Dahl, K. N., Zhong, F. L., Sammak, P. J. & Discher, D. E. (2007). Physical plasticity of the nucleus in stem cell differentiation. *Proceedings of the National Academy of Sciences* 104:15619–15624. DOI:10.1073/pnas.0702576104
39. Cross, S. E., Jin, Y.-S., Rao, J. & Gimzewski, J. K. (2007). Nanomechanical analysis of cells from cancer patients. *Nat Nano* 2:780–783. DOI:10.1038/nnano.2007.388
40. Guck, J. *et al.* (2005). Optical Deformability as an Inherent Cell Marker for Testing Malignant Transformation and Metastatic Competence. *Biophysical Journal* 88:3689–3698. DOI:10.1529/biophysj.104.045476
41. Suresh, S., Spatz, J., Mills, J. P., Micoulet, A., Dao, M., Lim, C. T., Beil, M. & Seufferlein, T. (2005). Connections between single-cell biomechanics and human disease states: gastrointestinal cancer and malaria. *Acta Biomater* 1:15–30. DOI:10.1016/j.actbio.2004.09.001
42. Khismatullin, D. B. (2009). Chapter 3 The Cytoskeleton and Deformability of White Blood Cells. *Current Topics in Membranes* Volume 64:47–111

43. Liu, Z., Cumberland, W. G., Hultin, L. E., Kaplan, A. H., Detels, R. & Giorgi, J. V. (1998). CD8+ T-lymphocyte activation in HIV-1 disease reflects an aspect of pathogenesis distinct from viral burden and immunodeficiency. *J. Acquir. Immune Defic. Syndr. Hum. Retrovirol* 18:332–340
44. Gregson, A. L. *et al.* (2008). Bronchoalveolar immunologic profile of acute human lung transplant allograft rejection. *Transplantation* 85:1056–1059.
DOI:10.1097/TP.0b013e318169bd85
45. Di Carlo, D. & Lee, L. P. (2006). Dynamic Single-Cell Analysis for Quantitative Biology. *Analytical Chemistry* 78:7918–7925. DOI:10.1021/ac069490p
46. Bao, N., Zhan, Y. & Lu, C. (2008). Microfluidic Electroporative Flow Cytometry for Studying Single-Cell Biomechanics. *Analytical Chemistry* 80:7714–7719.
DOI:10.1021/ac801060t

Chapter 2

Increased Asymmetric and Multi-daughter Cell Division in Mechanically Confined Microenvironments

This chapter explores the contributory effects of tumor microenvironment mechanical stresses on an inherently mechanical biological process: mitosis. As the microenvironment of a cell changes, associated mechanical cues may lead to the breakdown of biochemical signaling pathways, creating positive feedback to further propagate tumorigenesis.

An immense amount of past and current research is dedicated to understanding the control systems that govern the complex network of chemical reactions that dictate cell biology. Perhaps the most complex and most extensively studied cellular control system is the cell cycle regulatory system. Cell cycle regulation controls the progression of the life cycle of a cell and the growth of tissues, and is ultimately a significant contributor to the physiological homeostasis of complex multicellular organisms. However, recent research has shown that non-conventional mitosis events contribute to natural genetic variation¹, as well as tumor progression²⁻⁵.

Over half a century of research, sparked by Howard and Pelc's observation that radio-labeled phosphorous incorporates differentially into cells not undergoing mitosis⁶, has resulted in an increasingly complex understanding of cell cycle regulation. Regulation of the cycle depends on the constant production and degradation of proteins, and the activation or deactivation of the complexes responsible for targeting these proteins for degradation via ubiquitination. Environmental cues such as soluble factors have long been implicated in the cell cycle control system, however the past decade has given a new perspective on mechanical cues involved in

cell biology. In order to gain a more complete understanding of cell biology and the cell cycle, considering both soluble and mechanical cues will be necessary.

Mechanosensing is an important component of the physiology of the cell, as well as tissue homeostasis. Direct linkages between the extracellular matrix (ECM) and the intracellular environment allow external mechanical cues to alter the cellular state⁷⁻⁹. Conversely, these same linkages enable the cell to transmit forces extracellularly, altering the mechanical micro-environment itself¹⁰. Tipping this mechanical balance can result in cellular differentiation¹¹, morphology¹² and motility changes¹³, as well as alterations in cell cycle control¹⁴.

Mitosis is a highly regulated stage of the cell cycle, both biochemically and, more increasingly suspected, mechanically. The overall spherical shape that cells adopt during this phase and the internal organization of the cytoskeleton are directly implicated in influencing the progression through mitosis¹⁵. The Spindle Assembly Checkpoint (SAC) has been identified as the major checkpoint responsible for ensuring correct chromosomal alignment during metaphase¹⁶. The SAC requires specific mechanical cues to proceed through mitosis, including microtubule-kinetochore attachments as well as sufficient tension in microtubules themselves¹⁷, the satisfaction of which results ultimately in cytokinesis and mitotic exit¹⁸.

The cell division axis is also dependent on the orientation of ECM near the dividing cell and this effect requires an intact actin cytoskeleton¹⁹. This link between the ECM orientation, cytoskeleton, and condensed DNA is further supported by the co-localization of cytoskeletal binding proteins and the spindle apparatus during mitosis²⁰. Centrosome number and polarity has been shown to depend not only on an intact cytoskeleton²¹, but also on the phosphorylation state of focal adhesion kinase (FAK), further implicating a delicate force balance during mitosis²².

We propose that aberrant mitotic outcomes, possibly due to altered cytoskeletal mechanics during mitosis, can be directed by an altered mechanical microenvironment. To explore this hypothesis, we have developed a novel microfluidic platform to confine a population of proliferating HeLa cells. This novel culture platform allows for both alterations in the geometry of the microenvironment, specifically the space in which the cell is allowed to grow and divide, as well as the elasticity of the substrate on which the cell is dividing. Figure 1 illustrates the device, with an example of a mitotic cell directly interacting with the elastic substrate (Fig 1a). By using a microfluidic device to compress the cells, we minimize cell death due to lack of nutrients, as media is constantly perfused through the compression chamber. The device also allows for facile imaging of cells, as they are in a single focal plane.

Results and Discussion

Cells in confined 3D cultures exhibit drastic changes in size, shape, and symmetry of daughter cells when compared to unconfined 2D cultures. The height confinement also readily allowed visualization of condensed chromosomes at the mitotic plane. Within a $600 \mu\text{m}^2$ field-of-view cells are observed under time lapse bright-field microscopy for mitosis events. In the unconfined device control, with posts in the up position (Fig. 2a), cells attain a spherical geometry during mitosis and complete the mitosis process within 140 minutes. However, in confined conditions, tri-daughter cytokinesis (Fig. 2b & 2c), daughter cells with drastically different sizes (Fig. 2c), tetra-daughter cytokinesis (Fig. 2d), and mitosis resulting in cell death (Fig. 2e) are commonly observed events that increase in frequency with increasing compression (decreasing Δy) and increasing stiffness (E). Since multi-polar divisions have previously been classified as divisions containing multiple centrosomes ($N > 2$) during mitosis, to avoid confusion

we refer to multi-daughter divisions as observable division events resulting in more than 2 daughter cells (including observations of tri-daughter through penta-daughter cytokinesis).

Multi-daughter divisions induced by confinement lead to viable daughter cells with increased chances of chromosomal abnormalities. Interestingly, in figure 2b sequential tri-daughter divisions in consecutive cell cycles are observed for the high confinement, low stiffness condition ($\Delta y = 3 \mu\text{m}$, $E = 130 \text{ kPa}$). In this case and others (Fig. 2d) we note that cells dividing in this manner will sometimes “re-fuse” after division before the next cell cycle. Further investigation is warranted to determine whether this behavior is indicative of a new class of checkpoint control programs that acts post-cytokinesis. Even considering potential corrective measures (re-fusion) that cells may employ, tri-daughter divisions (Fig. 2b & 2c), divisions resulting in unevenly sized daughter cells (Fig. 2c) and tetra-daughter divisions (Fig. 2d) are likely to result in increased susceptibility to abnormal chromosome segregation. As the HeLa cell line is a 3N+ karyotype, the amount of assembly of mitotic spindles from each centrosome is increased by at least 50% when compared to diploid cells. With extra centrosomes ($N > 2$) and their associated mitotic spindles, metaphase and anaphase events are highly complex with respect to chromosome segregation to the poles even for bi-polar divisions. Even higher rates of missegregation are expected when cells divide in a multi-daughter fashion⁵.

The degree of mechanical confinement affects the daughter cell size ratio in normal and multi-daughter cell divisions. Figure 3 illustrates the highly altered mitosis division shape and asymmetry under varied conditions of confinement. Upon the completion of telophase, cells in control conditions are $\sim 20 \mu\text{m}$ in width and highly uniform (Fig. 3a), whereas in the extreme case of high confinement the daughter cells span between 40-80 μm in width and are highly asymmetric (Fig. 3d). For intermediate conditions, both increased stiffness and confinement act

to increase division asymmetry, as observed in the average traces (Fig. 3b, c). Quantification of daughter cell traces (Fig. 3e) demonstrates that the difference in area between daughter cells increases for all cases compared to control, where statistical significance ($p < 0.001$) is observed between both low confinement high stiffness and high confinement low stiffness compared to the control.

Interestingly, a marked difference in type of multi-daughter division was observed when maintaining confinement, and changing only the substrate stiffness (Fig. 3a-d). Under low compression ($\Delta y = 7 \mu\text{m}$) when substrate stiffness is 130 KPa, multi-daughter divisions result primarily in three progeny (90%, Fig. 3b), however upon increasing substrate stiffness to 1 MPa the multi-daughter division mode shifts primarily to four progeny (85%, Fig. 3c). Assuming cell volume remains similar, the smaller cross-sectional cell area observed for softer 130 KPa substrates indicates that cells are able to apply significant force to deform the PDMS substrate and adopt a more rounded form. Note that a similar force is presumably applied by the cell to the stiffer 1 MPa substrate but this leads to less deformation. In both cases the force applied by the cell, and therefore the equal and opposite force applied by the substrate to the cell are similar, but the cell shape differs. Therefore, cell shape during mitosis may be a dominant factor in directing multi-daughter divisions (in which a more spherical shape is achievable for the softer substrates). A tendency towards tri- or tetra- daughter divisions may be due to spatial limits of chromosome assembly at the metaphase plane(s) in a confined shape, which is dependent on substrate stiffness. Alternatively, the location of mechanical loads may direct the geometry of these multi-daughter divisions, perhaps acting through cortical cues sensitive to environmental force magnitudes²³.

Along with possible effects of the uneven size of daughter cells and multi-daughter divisions on chromosomal segregation, alteration in cell shape with confinement may also pose difficulties in critical mitotic processes such as spindle assembly, signaling, and targeting processes during check point regulation and may be responsible for the increase in abnormal mitosis behavior. For example, signaling relying on either diffusion or active transport may proceed slower or be more error prone over the longer distances in an enlarged discoid shaped cell compared to a tight spherical cell. Additionally, different cytoskeletal filaments have a characteristic persistence length over which they are effective (i.e. able to transmit force between protein complexes)²⁴. It is reasonable to postulate that by dramatically changing the shape of the cell from spherical to discoid, the lengths of force transmission (e.g. along microtubules from centrosome to kinetochore or from actin-based cortical cues to centrosomal microtubules^{5,23}) become anisotropic in varying directions of division, which may result in the underlying multi-polar and asymmetric divisions. Similarly, nonmuscle myosin II (NMM-II) distribution and contractility, necessary to create a uniform cleavage furrow during cytokinesis, may be affected by the non-spherical shape and anisotropic mechanical stress in these confined conditions. Fundamentally, these results suggest a role for adoption of a spherical shape during mitosis in maintaining bipolar division events.

Mechanical confinement leads to statistically significant differences in the frequency of mitotic abnormalities. A summary of the abnormalities observed per cell cycle is shown in figure 4a. Here we define the total abnormalities per cell cycle as the combined frequency of multi-daughter divisions, divisions resulting in unevenly sized daughter cells, divisions resulting in cell death, and completed mitosis in greater than 140 minutes. Increasing both the geometric confinement of cells and substrate stiffness, leads to increasing frequencies of mitotic

abnormalities (Fig. 4a). It should be noted that in the $E=1$ MPa high confinement case no successful cell divisions were observed, but observable mitosis events (prophase, metaphase) were observed.

Increased frequencies of multi-daughter divisions are observed in highly confined environments. A summary of multi-daughter divisions per cell cycle is shown in figure 4b. In the unconfined control condition less than 1% of cell divisions generate more than two daughter cells. In contrast, under low confinement ($\Delta y = 7 \mu\text{m}$) slight increases in the frequency of multi-daughter divisions are observed, and in high confinement cases ($\Delta y = 3 \mu\text{m}$) a drastic increase to 50% of all divisions are observed to lead to multi-daughter generation. Further, cells which have undergone 1 to 3 divisions remain viable and produce progeny of their own. Figure 2b shows a cell undergoing a 1 to 3 division, and subsequently one of the original daughter cells undergoing a second 1 to 3 division. This high frequency of multi-daughter divisions under confinement is unexpected, given that it is 17 times higher than the rate of multi-polar division events reported in standard 2D culture by Ganem et al.⁴, and suggests a fundamental relationship where confinement and elasticity of the environment can control the geometry of the cell division plane(s).

Unevenly sized daughter cells, cell death rates, and mitosis duration increase with increasing confinement. Of the cells completing mitosis, the rate of unevenly sized ($>15\%$ difference) daughter cells produced per mitosis event significantly increased with both stiffness and confinement: up to 100% of all divisions under the highest confinement (Fig. 4c). In control conditions, mitosis resulting in cell death, possibly due to intact checkpoint failures, is observed in less than 1% of all division events. Cell death increases significantly to 4% and 8% at low

confinement at $E = 130$ kPa and 1 MPa, respectively, and up to 70% under high confinement $E = 130$ kPa (Fig. 4d).

The duration of mitosis shown in figure 4e & 4f suggests increasing confinement is sufficient to increase mitotic duration. This corroborates previous observations by Kwon et al.²¹ and Maresca et al.¹⁷ that mitotic processes are dependent on correct orientation of, and force balance in, the cytoskeleton in order to achieve the proper signaling state to proceed through mitotic checkpoints in a timely manner.

A unique mitotic event resulting in five daughter cells under partial confinement was observed in which confinement was not complete such that the gap size was between 3-7 μm with $E = 130$ kPa (Fig. 5a). The cell in metaphase is 60 μm in diameter, 4 times wider than the 15 μm spherical cells undergoing mitosis during unconfined division. The metaphase lineup of chromosomes is highly abnormal as visual inspection suggests (Fig. 5a, left image) with at least 4 centrosome pole regions. Yet during anaphase (middle image), chromosome segregation seems to move toward 5 poles, leading to 5 daughter cells. Although the quantification of chromosome content is not available for these cells, it is reasonable to postulate that the chromosomes were incorrectly and unevenly segregated in this division, as with the other multi-daughter divisions (specifically to three daughter cells). In the case of the three daughter divisions, one replication cycle (S-phase), cannot be properly split into three without an extra half S-phase. In the case of the penta-daughter division, the same logic remains, however the mitotic planes appear to be even more complex. Although these penta-daughter division events are rare (observed twice over 500 single-cell observations), our single-cell analysis platform enables the capture of these rare atypical biological processes.

Conclusion

To elucidate the effects of confined mechanical microenvironments on cell behavior and mitotic processes, the microfluidic platform described here successfully creates confined culture environments that may mimic aspects of *in vivo* tumor mechanical properties. The data presented shows high instances of abnormal multi-daughter division events induced simply by increasing the confinement of a cell (i.e. decreasing the available volume to divide in) and by increasing the substrate stiffness. Further, the frequencies at which these abnormalities occur is found at much higher rates than previously observed. The ability to induce these abnormal divisions to drastically higher rates (half of all divisions in some cases) suggests a fundamental interaction between the extracellular mechanical environment and the overall orientation and the multipolarity of the cellular division axis.

The ability of this highly confined microenvironment to induce aberrant divisions, specifically multi-daughter divisions, is an intriguing finding in itself. Previously, work has been done to elucidate the biomolecular players involved in multi-centrosome divisions by Ganem et al.⁴, however here we contribute by supporting the hypothesis that multi-daughter divisions may be due, at least in part, to abnormal mechanical interactions between the cell and the immediate environment.

The observations made and metrics analyzed here are purely phenotypic. While chromosome quantification is not presented here, these abnormal phenotypic divisions strongly suggest aberrations in chromosome segregation, and should be investigated molecularly. These results provide strong initial evidence for the dependence of the mitotic geometry and polarity on the extracellular mechanical environment, and warrants dedicated in-depth molecular characterization of the phenomena.

Materials and Methods

Microdevice design

To simulate aspects of a compliant confinement microenvironment we designed a perfusable microfluidic device with a compressible assay chamber (4 mm x 6 mm) (Fig. 1). This setup allows for ease of observation while simulating a pseudo-3D environment. The device's low fluidic resistance allows uniform high density cell seeding and low shear stress during perfusion. The device operates under continuous perfusion with a total chamber volume exchange every two minutes to maintain the cells during assays. The array of 20 μm x 80 μm posts spaced 40 μm apart within the chamber provides control of the confinement height, structural support to resist sagging, and a pseudo-3D confined environment. In contrast to 3D culture in hydrogel systems our system provides precise control of the confinement volume, active uniform delivery of nutrients to each cell, and a single imaging plane.

Microfluidic chip fabrication

The master molds for the mechanical micro-confinement culture device were fabricated using negative photoresist (SU-5, Microchem Corporation). The base layer was spun on at 950 RPM to yield a 15 μm channel height, and the post heights (Δy) were 7 μm and 3 μm , corresponding to 1750 RPM and 3300 RPM, respectively. Poly(dimethylsiloxane) (PDMS) was prepared with varying (v/v) ratios of crosslinker to base (1:10 for $E=1$ MPa and 1:20 for $E=130$ kPa)²⁵. The elastomer devices were cured at 65°C overnight, then cut from the mold, punched, and bonded to clean glass slides (Fisher Scientific) after treatment of both the glass and PDMS with Oxygen Plasma (0.5 Torr, 35 W) for 20 seconds.

Cell culture & experimental setup

Human cervical carcinoma (HeLa) cells were purchased from American Type Culture Collection (ATCC, Manassas, VA, catalog CCL-2). Cells were maintained in high glucose Dulbecco's modified Eagle's medium (DMEM), 100 $\mu\text{g mL}^{-1}$ penicillin, 100 $\mu\text{g mL}^{-1}$ streptomycin, and 10% fetal bovine serum (Gibco). Cell synchronization was performed by a two day serum starve followed by a 2 mM double thymidine block²⁶. Prior to the assay, the device was primed and flushed with ethanol at 20 $\mu\text{L min}^{-1}$ for 15 minutes, followed by a PBS flush at 20 $\mu\text{L min}^{-1}$ for 15 minutes. The device was then coated with bovine fibronectin (Invitrogen) 50 $\mu\text{g mL}^{-1}$ adsorbed nonspecifically for 90 minutes at room temperature. Cells were loaded as a suspension of 1 million cells mL^{-1} to achieve a final in-device density of approximately 100 cells per $600 \mu\text{m}^2$ in the confinement assay area (Fig. 1a). Cells were then placed in a microscope incubator for 20 minutes to allow for attachment.

For confinement assays, the device was compressed via a calibrated weight. To determine the proper mass to use for each confinement and stiffness case, a separate device, not containing cells, perfused with blue dye was used to determine when the posts came in contact with the glass substrate (i.e. the posts became optically clear). This process is graphically represented in figure 1b. The mass of calibration weights (80-100 g) were also confirmed by streak imaging of 2.2 μm beads which allowed tracking of compression progress (Fig. S1). Once the beads were no longer transiting under the posts, an effective calibration weight was arrived at. The heights of the devices were kept approximately constant by pouring an equal volume of PDMS:crosslinker each time a new device was molded from the master to achieve a bulk height of approximately 5 mm. Upon confinement, cells are subjected to a confinement force that is

equal to the force exerted by the cell onto the substrate. This confinement force is dependent on the confinement height but not the substrate elasticity.

The perfusion of supplemented DMEM media began at one half of a volume exchange of the chamber per minute (750 nL min^{-1}). Live-cell imaging was performed in a microscope incubator (temperature and CO_2 controlled) with an inverted microscope (Nikon Eclipse TI). Images were captured with a Coolsnap HQ2 camera on the Nikon Advance Research software (Nikon) every five minutes with experiments lasting up to six days.

The mechanical microenvironment of the cell is defined by the spatial confinement volume and elastic modulus of the substrate. As the PDMS membrane is approximately 5 mm thick for each device, a large damping of the applied force to lower the chamber is expected such that the total effective force at the chamber cell interface is dependent on the elasticity of the polymer matrix with minimal dependence on the force used to lower the chamber. In the case of a thin PDMS membrane the applied force would have a significant impact on the total effective force on the cell, however this is not the case in this system. In figure S2, we further investigate this by examining whether the load used to compress the cells affects the cell's ability to deform the PDMS substrate. The numerical simulations do not show a difference between load and no-load conditions.

Analysis

Before extracting quantitative data on cell morphology the completeness of confinement was confirmed for each cell video by observing that no cells in the FOV transited under posts. In this way we ensured an expected and repeatable height of confinement was achieved. ImageJ was used to perform analysis on the images obtained experimentally. Specifically, the area

function was used to calculate the areas of daughter cells after cytokinesis by manually outlining each daughter cell, after a complete cleavage furrow and separation was observed. Each mitosis event was manually identified and characterized. The onset of mitosis was defined as the point at which the cell lost its spindled morphology and became completely rounded. It should be noted that in highly confined cases, mitosis onset was identified by the appearance of a well defined circular cell edge, as most of the cells did not adopt the classical spindled morphology under high confinement.

For statistical analysis, the population number (n) used corresponds to the total number of events observed in a single category of abnormality (e.g. multi-daughter divisions, uneven divisions, etc). These sample sizes were created by repeating each experimental condition two times, meaning two separate devices. The standard errors of the ‘per division’ metrics were found using the standard error of the estimate of a proportion. Confidence intervals between the mitotic duration times were performed with the Welch t-test, as the distributions did not have the same standard deviations. The confidence intervals in comparing proportions, such as abnormalities per cell cycle, etc were calculated using the z statistic for proportions.

Solid mechanics numerical simulation was performed using COMSOL v4.2 (Los Angeles, CA, USA).

Figures

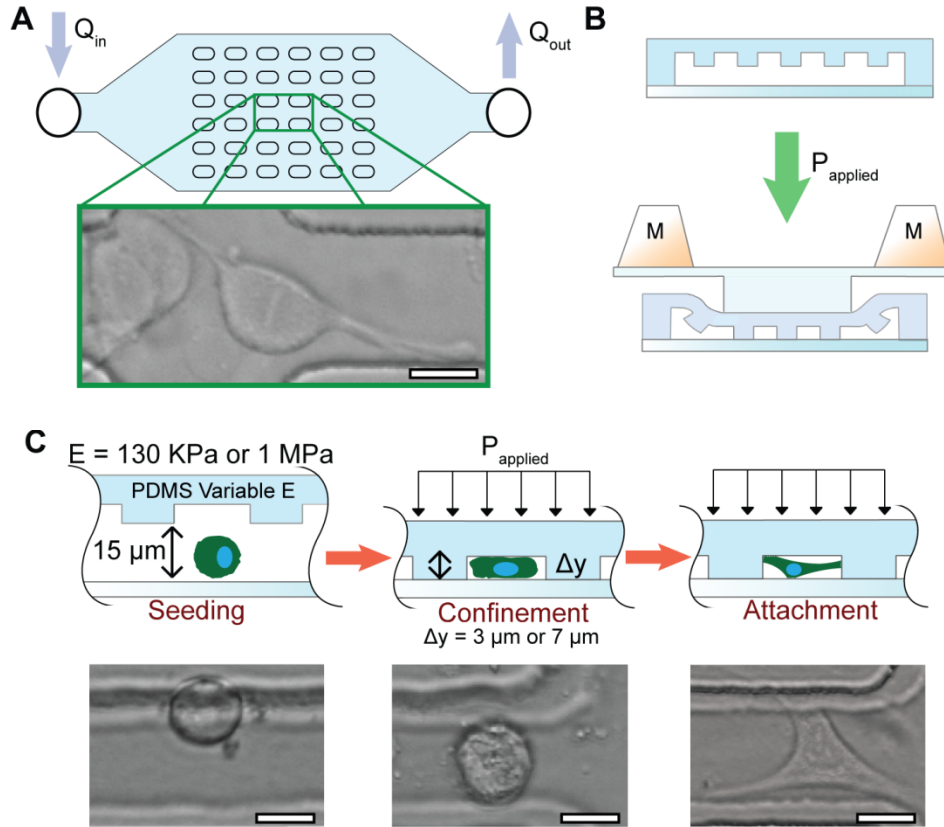


Figure 1 Microfluidic cell confinement device. (A) Device schematic with inset of confinement assay. The posts are $20 \times 80 \mu\text{m}$ spaced equally $40 \mu\text{m}$ apart. (B) In the unconfined state, the posts are raised from the glass substrate (top), upon applying pressure the confinement chamber is compressed such that the posts are in contact with the glass substrate. (C) Seeding cells in the confinement chamber (left), when the posts are lowered the cell is confined to 3 or $7 \mu\text{m}$ height and is squeezed out from the post area (middle). Cells spread and attach in the confined volume (right).

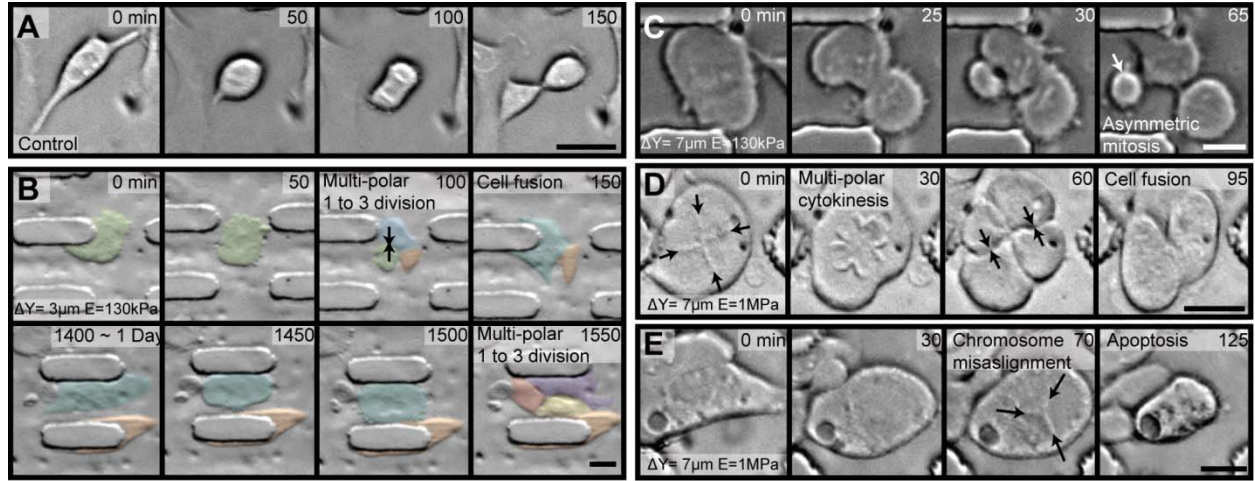


Figure 2 Abnormal cell divisions under mechanical confinement. (A) In an unconfined device control, mitosis occurs within 150 minutes. (B) A confinement condition ($\Delta y = 3 \mu\text{m}$, $E = 130 \text{ kPa}$) showing sequential tri-daughter divisions with viable daughter cells. The first tri-daughter division is seen at 100 minutes, with cell fusion labeled by black arrows. The second tri-polar division is seen at 1550 minutes along with the viable 2nd daughter cell labeled in orange. (C) A confinement condition ($\Delta y = 7 \mu\text{m}$, $E = 130 \text{ kPa}$) showing an asymmetric multi-daughter division of cytoplasm after mitosis (cell with arrow receives disproportionate cytoplasmic volume). (D) A confinement condition ($\Delta y = 7 \mu\text{m}$, $E = 1 \text{ MPa}$) showing a tetra-daughter division with a cross geometry chromosome alignment (marked by black arrows at 0 minutes) and cell fusion at 60 minutes (labeled by black arrows). (E) A confinement condition ($\Delta y = 7 \mu\text{m}$, $E = 1 \text{ MPa}$) showing a triangular chromosome arrangement (marked by black arrows) leading to cell death. All scale bars are $20 \mu\text{m}$.

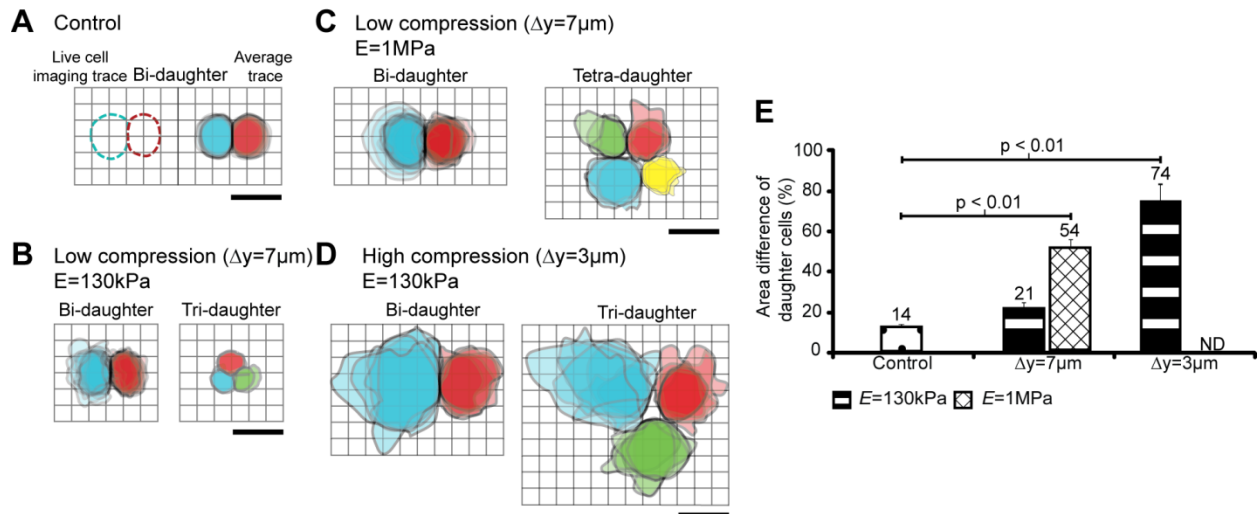


Figure 3 Daughter cell asymmetry and multi-daughter division increases with confinement and stiffness. Overlaid cell traces for control and all experimental conditions are shown. (A) Cell traces are analyzed 5 minutes post-telophase. Average control divisions are shown. (B,C) Low confinement average traces show increased size and asymmetry in stiffer environments. Notably, multi-daughter division type (tri- vs. tetra-daughter) depends on microenvironment mechanical properties. (D) In high confinement states, the daughter cells are more spread out and highly asymmetric when compared to both low compression and control cases. (e) Area difference between daughter cells in each test case demonstrating asymmetry differences. Error bars are SEM. All scale bars are 20 μm .

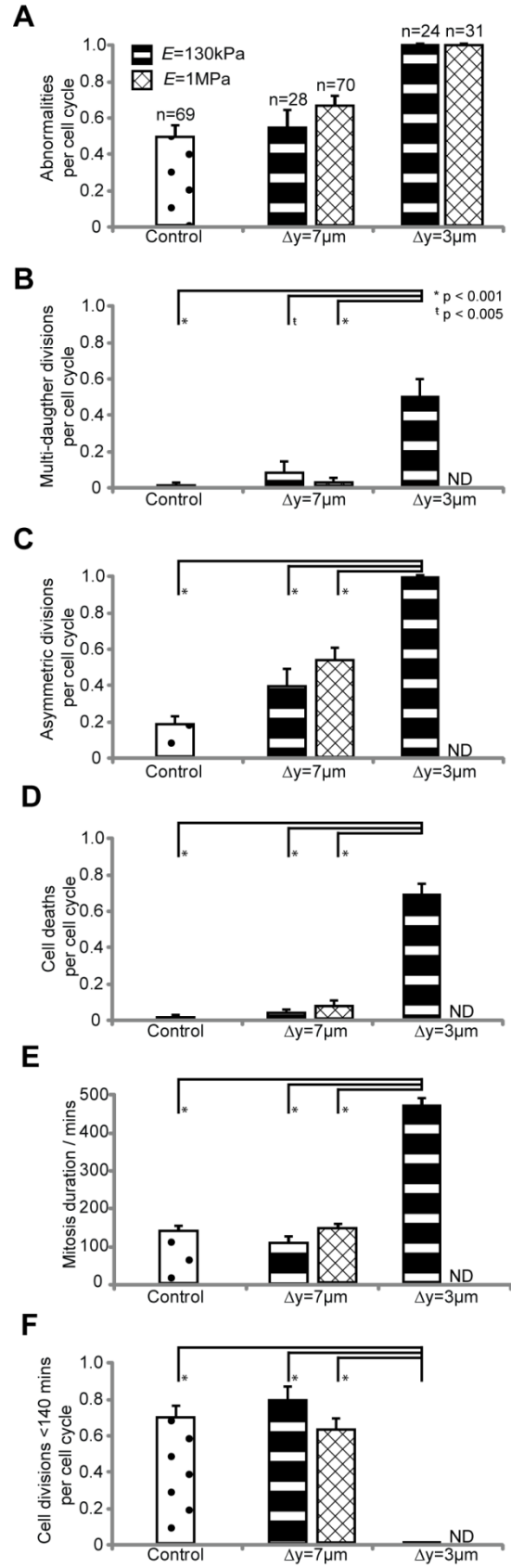


Figure 4 Quantitative effects of confinement on cell-cycle abnormalities. (A) Summary of experimental data in terms of abnormalities per cell cycle characterized by: multi-daughter divisions, asymmetric divisions, apoptotic divisions, and divisions lasting for more than 140 minutes. (B) Multi-daughter divisions per cell cycle characterized as divisions producing more than two daughter cells. Error bars are SEP. (C) Asymmetric divisions are characterized by daughter cells having a difference greater than 15% in area. Error bars are SEP. (D) Cell deaths per cell cycle are characterized by cells that cease activity and contract prior to completion of mitosis. Error bars are SEP. (E) Comparing the mitosis duration of the high confinement ($\Delta y = 3 \mu\text{m}$, $E=130 \text{ kPa}$) condition to control and both low confinement conditions. Error bars are SEM. (F) Summary of divisions in each case completing division within 140 minutes. For high confinement $E=1\text{MPa}$, no data (ND) was available as no completed mitosis events was observed. Error bars are SEP.

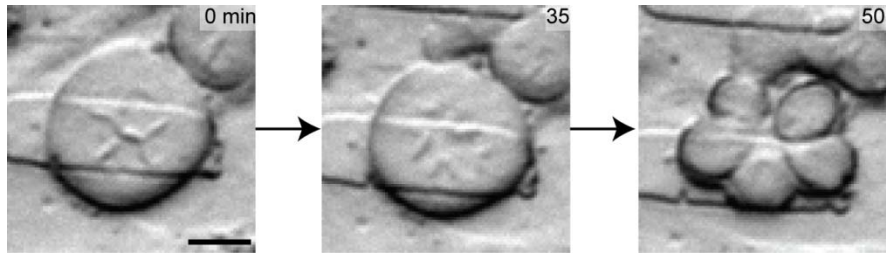


Figure 5 A penta-daughter cell division may lead to aneuploid daughter cells. As a qualitative example, this cell is in a partially confined state between 3 – 7 μm . Extreme confinement conditions observed here can lead to aberrant mitotic orientation resulting in highly asymmetric divisions. These microscopic images show the time lapse of a cell undergoing a single 1 \rightarrow 5 successful mitosis. Scale bar: 20 μm .

Supplementary Figures

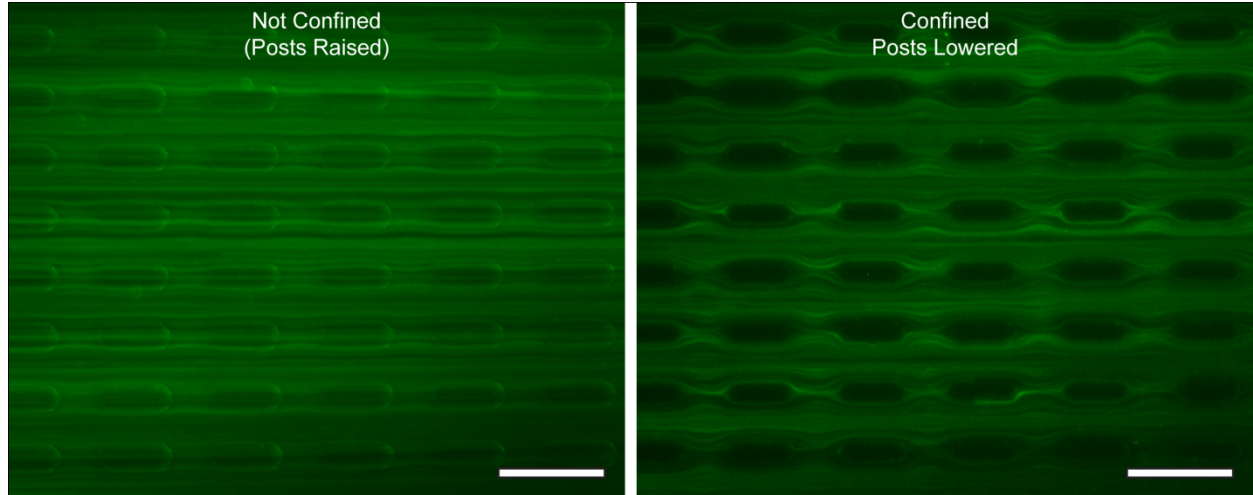


Figure S1: Device compression as qualified by streak imaging of 2.2 μm beads. Uncompressed 7 μm device (left), fully compressed 7 μm device (right). Scale bars 50 μm .

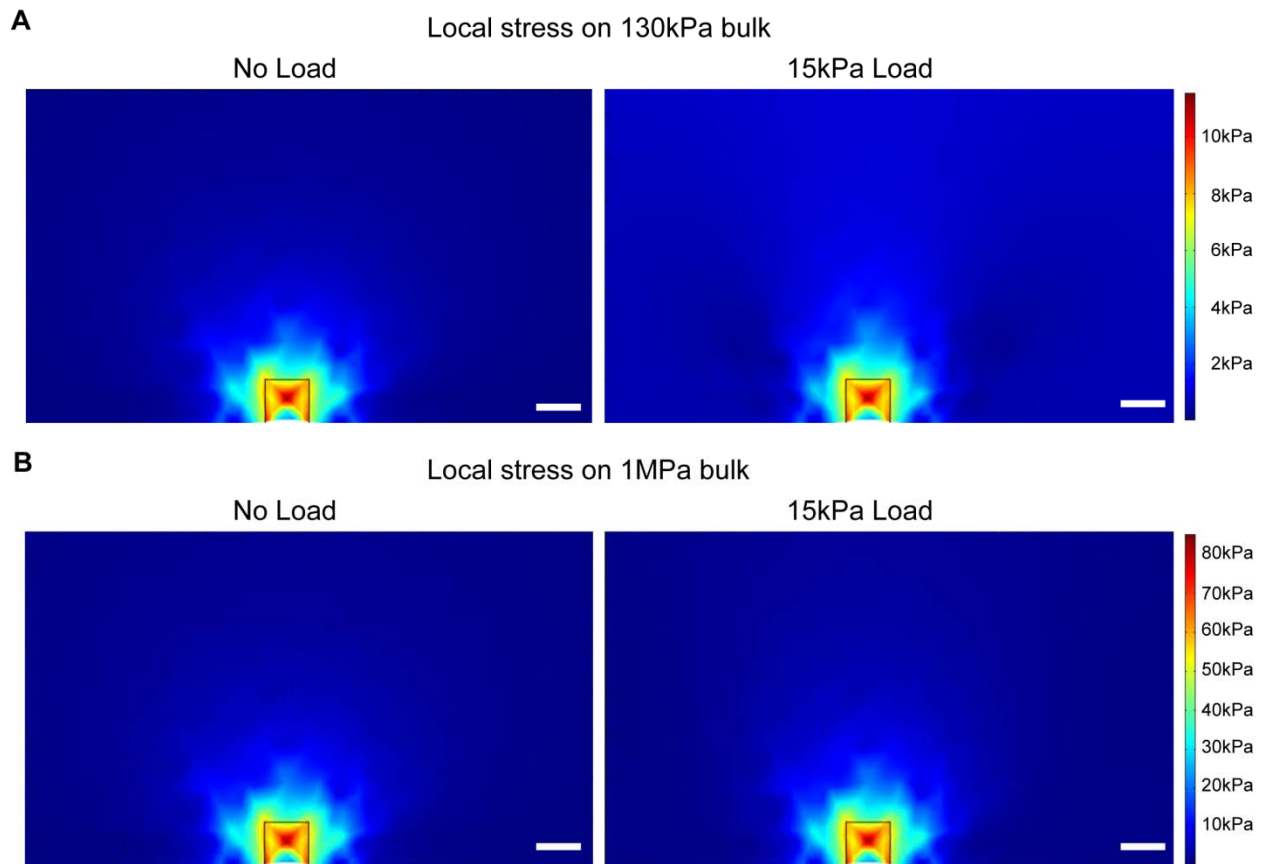


Figure S2: COMSOL simulation of effective force at the cell interface. Numerical simulations comparing a 1 μm substrate deformation and the resulting stresses between no-load and a calibrated 15 kPa load with a 5 mm bulk PDMS layer. (A) Simulation setup for no load and 15kPa load. (B) Interfacial stresses at the cell interface and substrate. Scale bars 10 μm .

Bibliography

1. Duncan AW, Taylor MH, Hickey RD, Hanlon Newell AE, Lenzi ML, et al. (2010) The ploidy conveyor of mature hepatocytes as a source of genetic variation. *Nature* 467: 707–710. DOI:10.1038/nature09414.
2. Erenpreisa J, Cragg MS (2010) MOS, aneuploidy and the ploidy cycle of cancer cells. *Oncogene* 29: 5447–5451. DOI:10.1038/onc.2010.310.
3. Vitale I, Senovilla L, Jemaà M, Michaud M, Galluzzi L, et al. (2010) Multipolar mitosis of tetraploid cells: inhibition by p53 and dependency on Mos. *EMBO J* 29: 1272–1284. DOI:10.1038/emboj.2010.11.
4. Ganem NJ, Godinho SA, Pellman D (2009) A Mechanism Linking Extra Centrosomes to Chromosomal Instability. *Nature* 460: 278–282. DOI:10.1038/nature08136.
5. Kops GJPL, Weaver BAA, Cleveland DW (2005) On the road to cancer: aneuploidy and the mitotic checkpoint. *Nat Rev Cancer* 5: 773–785. DOI:10.1038/nrc1714.
6. Howard A, Pelc SR (1956) A difference between spermatogonia and somatic tissues of mice in the incorporation of [8-14C]-adenine into deoxyribonucleic acid. *Exp Cell Res* 11: 128–134.
7. Shyy JY-J, Chien S (2002) Role of integrins in endothelial mechanosensing of shear stress. *Circ Res* 91: 769–775.
8. Bershadsky AD, Balaban NQ, Geiger B (2003) Adhesion-dependent cell mechanosensitivity. *Annu Rev Cell Dev Biol* 19: 677–695. DOI:10.1146/annurev.cellbio.19.111301.153011.
9. Ingber DE (2008) Can cancer be reversed by engineering the tumor microenvironment? *Semin Cancer Biol* 18: 356–364. DOI:10.1016/j.semcancer.2008.03.016.
10. Lelièvre SA, Weaver VM, Nickerson JA, Larabell CA, Bhaumik A, et al. (1998) Tissue phenotype depends on reciprocal interactions between the extracellular matrix and the structural organization of the nucleus. *Proc Natl Acad Sci U S A* 95: 14711–14716.
11. Kilian KA, Bugarija B, Lahn BT, Mrksich M (2010) Geometric cues for directing the differentiation of mesenchymal stem cells. *Proc Natl Acad Sci USA* 107: 4872–4877. DOI:10.1073/pnas.0903269107.
12. Kumar S, Weaver VM (2009) Mechanics, malignancy, and metastasis: The force journey of a tumor cell. *Cancer Metastasis Rev* 28: 113–127. DOI:10.1007/s10555-008-9173-4.

13. Alexander NR, Branch KM, Parekh A, Clark ES, Iwueke IC, et al. (2008) Extracellular matrix rigidity promotes invadopodia activity. *Curr Biol* 18: 1295–1299. DOI:10.1016/j.cub.2008.07.090.
14. Assoian RK, Klein EA (2008) Growth control by intracellular tension and extracellular stiffness. *Trends Cell Biol* 18: 347–352. DOI:10.1016/j.tcb.2008.05.002.
15. Théry M, Bornens M (2008) Get round and stiff for mitosis. *HFSP J* 2: 65–71. DOI:10.2976/1.2895661.
16. Musacchio A, Salmon ED (2007) The spindle-assembly checkpoint in space and time. *Nat Rev Mol Cell Biol* 8: 379–393. DOI:10.1038/nrm2163.
17. Maresca TJ, Salmon ED (2010) Welcome to a new kind of tension: translating kinetochore mechanics into a wait-anaphase signal. *J Cell Sci* 123: 825–835. DOI:10.1242/jcs.064790.
18. Peters J-M (2006) The anaphase promoting complex/cyclosome: a machine designed to destroy. *Nat Rev Mol Cell Biol* 7: 644–656. DOI:10.1038/nrm1988.
19. Théry M, Racine V, Pépin A, Piel M, Chen Y, et al. (2005) The extracellular matrix guides the orientation of the cell division axis. *Nat Cell Biol* 7: 947–953. DOI:10.1038/ncb1307.
20. Vilmos P, Jankovics F, Szathmári M, Lukácsovich T, Henn L, et al. (2009) Live imaging reveals that the *Drosophila* actin-binding ERM protein, moesin, co-localizes with the mitotic spindle. *Eur J Cell Biol* 88: 609–619. DOI:10.1016/j.ejcb.2009.05.006.
21. Kwon M, Godinho SA, Chandhok NS, Ganem NJ, Azioune A, et al. (2008) Mechanisms to suppress multipolar divisions in cancer cells with extra centrosomes. *Genes Dev* 22: 2189–2203. DOI:10.1101/gad.1700908.
22. Park AYJ, Shen T-L, Chien S, Guan J-L (2009) Role of focal adhesion kinase Ser-732 phosphorylation in centrosome function during mitosis. *J Biol Chem* 284: 9418–9425. DOI:10.1074/jbc.M809040200.
23. Théry M, Jiménez-Dalmaroni A, Racine V, Bornens M, Jülicher F (2007) Experimental and theoretical study of mitotic spindle orientation. *Nature* 447: 493–496. DOI:10.1038/nature05786.
24. Gittes F, Mickey B, Nettleton J, Howard J (1993) Flexural rigidity of microtubules and actin filaments measured from thermal fluctuations in shape. *J Cell Biol* 120: 923–934.
25. Ochsner M, Dusseiller MR, Grandin HM, Luna-Morris S, Textor M, et al. (2007) Micro-well arrays for 3D shape control and high resolution analysis of single cells. *Lab Chip* 7: 1074–1077. DOI:10.1039/b704449f.

26. Stein GS, Borun TW (1972) The synthesis of acidic chromosomal proteins during the cell cycle of HeLa S-3 cells. I. The accelerated accumulation of acidic residual nuclear protein before the initiation of DNA replication. *J Cell Biol* 52: 292–307.

Chapter 3

Hydrodynamic Stretching of Single Cells for Large Population Mechanical Phenotyping

The previous chapter explored how environmental mechanical stresses - as found in tumor environments - can create a positive feedback loop to increase genetic instability through aberrant mitosis events. Epigenetic changes, such as increased chromosome count and increased transcription levels due to aneuploidy, can alter cell mechanics. This is a contributing motivation for this chapter and the development of a high-throughput label-free mechanical properties-based biomarker platform.

There is growing evidence that cell deformability (i.e. the ability to change shape under load) is a useful indicator of changes in the cytoskeleton and nuclear organization and may provide a label-free biomarker for determining cell states or properties such as metastatic potential¹⁻³, cell cycle stage⁴, degree of differentiation^{5,6}, and leukocyte activation⁷. Clinically, a measure of malignancy and metastatic potential in tissues or biological fluids could guide treatment decisions, or a measure of degree of differentiation could prevent transplantation of undifferentiated, tumorigenic stem cells in regenerative therapies. For drug discovery and personalized medicine, a simple measure of cytoskeletal integrity could allow screening for cytoskeletal-acting drugs or evaluation of cytoskeletal drug resistance in biopsied samples. Additionally, measures of leukocyte activation are strong predictors of disease prognosis and response to treatment in persons with HIV-1 infection⁸ or rejection of allografts⁹. Currently, major barriers to clinical use of flow cytometry-based assays for these applications are requirements for costly fluorescent-labeled antibodies and skilled technicians to prepare samples and interpret results. A simple label-free deformability measurement in which cells are

minimally handled thus has the potential to greatly reduce costs and allow routine cell screening and classification in clinical and research applications¹⁰.

A wide variety of platforms have been engineered to perform mechanical measurements on cells¹¹. Generally, these techniques can be divided into two categories based on the samples they act on: bulk and single-cell¹². Bulk platforms, such as microfiltration, tend to have high throughput, but they yield one endpoint measurement and do not take into account heterogeneity or size differences within the sample population of cells. Disease may develop from abnormalities in a single cell¹² or small subset, such that accurately detecting rare events or small populations is important, and bulk measurement may result in misleading averages¹³. Single-cell platforms that can assay this heterogeneity include micropipette aspiration⁵, atomic force microscopy (AFM)³, magnetic bead-based rheology, microfluidic optical stretching^{2,14}, and microfluidic cell transit analyzers^{12,15-17}. In particular, microfluidic single-cell mechanics assays have been promising, yielding more automated measurements through microscopically observed cell transit through microchannels or pores^{12,15-17}. In these approaches the transit time at a constant pressure is indicative of mechanical properties; however, cell size and adhesiveness also can contribute to the measurement, which is especially relevant when dealing with heterogeneous cell solutions. In general, current approaches, usually optimized for biophysics research, operate at rates from 1 cell/min (AFM and optical stretching) to ~1-5 cells/sec (microfluidic cell transit analyzers, electroporative flow cytometry¹⁸).

A unique combination of inertial focusing, hydrodynamic stretching, and automated image analysis enables us to carry out tunable single-cell mechanical measurements of cells with a throughput several orders of magnitude greater than current systems (~2,000 cells/s). Cells are carried and measured surrounded by fluid, and never contact, adhere to, or foul channel surfaces

which can lead to clogging. Moreover, the method results in high strains, which are easy to visualize, and high strain rates which deliver unique insights into cell mechanics. The large observed strains are due to stresses approximately an order of magnitude greater than current methods¹⁹.

Briefly, we employ inertial focusing, a sheath-less method of ordering cells in flow²⁰⁻²², to deliver suspended cells uniformly to an extensional flow^{23,24} region where they are deformed (Fig. 1a-d). Uniform delivery leads to increased uniformity in the hydrodynamic stresses and resulting deformation of individual cells. A microfluidic approach also allows tuning of the magnitude of hydrodynamic stresses which is important to be able to obtain sensitive measurements for cells with a range of deformabilities (see Supplemental Fig. 1). After entering the extensional flow region, an inverted microscope-mounted high-speed camera records several thousand deformations per second. Then, an automated image analysis algorithm finds and tracks cells to quantify initial diameter and deformability (the length of the long axis of a deformed cell divided by a perpendicular shorter axis) which are plotted in flow cytometry-like 2D scatter plots (Fig. 1e-f and Supplemental Fig. 2 online). This automation limits user bias and strengthens repeatability which are notable issues with manual mechanical measurements. Further, the ability to measure whole cell deformation of spherical cells in suspension limits variability due to the contact point of AFM tips or micropipettes on mechanically heterogeneous attached cells (e.g. significant differences in stiffness in the vicinity or far from actin stress fibers)²⁵. However, in cases where this heterogeneity during adhesion is of interest we cannot directly probe cells (a task which can be performed by AFM and micropipettes).

In this work, we thoroughly characterize the method and provide demonstrations of its robustness and utility with over 100,000 single-cell mechanical measurements: in clinical

screening of pleural fluids for malignant cells and characterization of stem cell differentiation state. Mechanistic and experimental details are provided in the Online Methods section.

Specifically, we discuss modes of deformation, standard operating protocols (cell densities, flow rates), and methods of controlling for mechanical drift (Supplemental Fig. 3) that occurs when adherent cells are brought into suspension.

Results and Discussion

Validation and calibration of measurement

Clearly, cells are complex viscoelastic objects; however, we investigated the deformation of several simple model systems to validate and calibrate our measurements. Surfactant-stabilized oil droplets of low surface tension and known viscosity were measured to confirm that deformability cytometry could distinguish between objects of different viscoelastic properties. Droplets from 500 to 10,000 cSt, deformed an amount trending with their internal viscosity (external viscosity was held constant; see methods, Supplemental Fig. 4), allowing for evaluation of an effective viscosity of a deformed cell. We describe the viscosities of these emulsions as ratios of their internal dynamic viscosity, μ_i , to that of water, μ_o . ($\lambda = \mu_i / \mu_o$)^{26,27}. Cell mechanical behavior is predominantly determined by viscous properties at high strain rates^{28,29}. Generally, cells deformed like emulsions with $\lambda < 9,650$. As further validation, we also see a large decrease in deformability upon chemically crosslinking proteins in HeLa cells (cervical carcinoma cells fixed with 4% formaldehyde; see Supplemental Fig. 4 online).

Next, we characterized the intrinsic noise level of deformability cytometry by measuring physical properties of rigid polystyrene microspheres (see Supplemental Fig. 4). The semi-interquartile range of the deformability measurement was an order of magnitude lower than that

of a cancer cell line, suggesting that variability in cellular deformation measures is not due to measurement error. A correctable systematic error in the deformability of these rigid particles was also observed which can be attributed to 1 μ s exposure time blur in the direction of particle motion.

Certainly, a barrier to translation of biophysical measurements is repeatability and variability between labs. We measured the deformability of the breast cancer epithelial MCF7 cell line on different days in different replicas of the device and found no statistical difference (nonparametric Wilcoxon ranked sum; $p=0.22$; Supplemental Fig. 3). It will still be important to confirm this minimal variability when the technique is applied in other labs.

Identification of inflammation and malignancy in pleural fluids

Confident in the accuracy of our deformability measurements we initiated studies to examine the mechanical properties of cells suspended within blood and pleural fluids, analysis of which provides insight into various diseases such as inflammation, bacterial infections, and tumor progression³. It has been hypothesized that the invasiveness of metastatic cells, which may accumulate in these fluids, is conferred by increased deformability¹, and there is a precedent for using mechanical measurements of small sample sizes of biopsied cells for clinical diagnostics³⁰ in which mechanical measurements correlated with current immunohistochemical methods³. Work by Cross et al. showed that metastatic cancer cells disseminated in pleural fluid were 70% softer than benign cells from the same sample (N=40 cells) while Remmerbach et al. found that oral squamous cell carcinoma cells obtained by mucosal biopsy were 3.5 times more compliant than cells from healthy patients using a sample of 71 cells. However, in these previous studies time-consuming protocols are first needed to select cells to measure. By using deformability

cytometry, sampling thousands instead of tens of cells is possible such that all cells in a complex population can be measured without pre-selection. Improved statistical accuracy is conferred, and identification of outlier populations is possible.

Pleural fluids – the fluid that accumulates in the space between the lungs and the chest cavity - is of diagnostic importance for metastatic disease. Cytological examination of pleural fluids for detection of malignancy is not always reliable, with an overall sensitivity rate ranging from 40% to 90%, with higher false-negative rates for mesotheliomas and lymphomas^{31,32}.

Furthermore, the preparation of cell smears and blocks (Figure 2d-g right) requires technician-intensive fixation, labeling, and sample preparation, followed by manual microscopic scanning of slides by the cytopathologist to visually identify cells with suspicious features.

Immunofluorescence flow cytometry is not routinely performed in the clinic. The reason is that the reagents and instruments for these systems must be routinely calibrated – (i) the fluorophore-conjugated antibody must have extensive quality control to make sure there are minimal batch to batch variations in fluorescence, (ii) the flow cytometer laser power and detector sensitivity must also be routinely calibrated with uniform intensity standard fluorescent beads. Notably, a deformability measurement is an intrinsic property of a cell and therefore does not depend on the quality of a label or power of a detector.

Pleural fluid contains a high density of blood cells which may obscure cells of interest. To gain insight into how this leukocyte population would appear in the pleural fluid, we first measured the deformability of resting peripheral blood mononuclear cells (PBMCs) and PBMCs activated with an anti-CD3 antibody (12F6) or phytohaemagglutinin (PHA) for two days. On average, stimulated PBMCs were much more deformable and slightly larger (12F6 activated PBMCs: median deformability=1.47, N=3,474; PHA activated PBMCs: median

deformability=1.45, N=4,765) than unstimulated PBMCs (median deformability=1.18, N=4,377; Figure 2a). Activated PBMCs deformed similarly to oil-in-water emulsions with $\lambda \leq 760$ while untreated control PBMCs deformed similar to emulsions with $\lambda = 970$. Microfilaments, microtubules, and the intermediate filament, vimentin, reorganize during activation. It is hypothesized that this reorganization—a loss of rigidity—enables transendothelial migration^{33,34}. On the other hand, granulocytes were expected to become less deformable upon stimulation. Here, in vitro activation of granulocytes with fMLP treatment shifted the median deformability value from 1.19 to 1.33 ($p < 0.001$, $N_{\text{resting}}=3,200$, $N_{\text{activated}}=3,374$) and increased the number of highly deformable cells above deformability = 1.4 (Figure 2b). While this does not agree with previous studies, previous measurement methods are prone to misinterpret changes in cell size and adhesiveness as increases in cell stiffness³⁵. Most importantly, we have reproducibly measured these differences and expected to be able to detect these changes for stimulated leukocytes in vivo.

Through characterization of cells from the pleural fluids of 47 patients we constructed deformability cytometry profiles of the primary cell populations associated with the common disease states detectable by cytological analysis and developed a 2-dimensional gating strategy to classify unknown samples (Figure 2c). These profiles are based on our initial scatter plots for PBMCs and stimulated PBMCs as well as correlation with the cytology diagnosis. We performed deformability cytometry on pleural effusions collected within the same day in parallel with traditional cytological methods; possible cytological diagnoses included: negative for malignancy, positive for malignancy, acute inflammation associated with an increased neutrophil population, and chronic inflammation—associated with a larger fraction of lymphocytes and histiocytes. In the diagnosed carcinoma cases, the tissue of origin was often known from patient

history. Prior to deformability cytometry, any red blood cells in the pleural fluids were hypotonically lysed leaving behind white blood cells, benign mesothelial cells, and cancer cells, if present. Leukocytes make up a majority of the cellular population in pleural fluids, but metastasized tumor cells from ovarian cancer, breast cancer, lung cancer, gastrointestinal track cancer, mesothelioma, and lymphoma can accumulate in the pleural fluid. Benign mesothelial cells, which are contaminants of the thoracentesis—the process of draining pleural fluids—are also present in the samples which we analyzed.

As expected, patients diagnosed negative for malignancy and without diagnoses of acute or chronic inflammation were measured to have small rigid cells, features corresponding to unactivated leukocytes (Figure 2d). As indicated in cell blocks and cell smears benign mesothelial cells are also present. These likely appear as large rigid cells in our assay (Figure 2d center). Patient samples with a larger fraction of lymphocytes and histiocytes (tissue macrophages and dendritic cells) due to prolonged immune activation are diagnosed as chronic inflammation. Deformability scatter plots obtained from a majority of these samples show a strong similarity to those for in vitro activation of PBMCs, in which we observe a slight increase in median initial diameter and a large increase in median deformability (Figure 2e). Pleural fluids from patients with a larger fraction of neutrophils are diagnosed as acute inflammation. In agreement with our in vitro measurements of stimulated neutrophils we observed many small cells and a greater quantity of highly deformable small cells than for measurements of resting leukocytes (Figure 2f).

The deformability cytometry profiles of patients diagnosed with malignancy are markedly different from all other outcomes (Figure 2g). In these cases, we observe many large cells ($>17\ \mu\text{m}$) which are also highly deformable (>1.4). Gating in this region for all carcinoma

and mesothelioma cases (N=11), yields a high percentage of cells in this region: $15.7 \pm 8.7\%$ ($\mu \pm \sigma$). Whereas similar gating of negative outcome cases (N=9) yields $0.8 \pm 0.3\%$ ($\mu \pm \sigma$) in this upper right quadrant. Thus, if we use less than 1% of cells measuring within the gate as a selection criteria for a true negative outcome, the deformability assays achieves an overall sensitivity of 91% and specificity of 65% in detecting malignancy when screening against all patient outcomes (N=47). Specificity can be improved to 86% without affecting sensitivity by algorithmically identifying chronic inflammation cases in which there are also large deformable cells that lie on the border of the gate (Supplemental Figure 5). In some patients with a diagnosed negative outcome, large, rigid putative mesothelial cells are also present which can confound diagnoses of malignancy based on cell size alone (Figure 2d center). Supplemental Table 1 contains patient diagnoses based on traditional cytological methods and deformability cytometry.

Given the predictive power of our label-free cytological method, we envision deformability cytometry could complement histological analysis of pleural fluids following a thoracentesis, or even disaggregated biopsies, with high-throughput ensuring thorough sampling of the tumor mass that is often not possible with manual inspection of pathology slides. As a negative cytology result is not conclusive, the higher sensitivity conferred by deformability cytometry has the potential to eliminate costly patient follow-up procedures and invasive biopsies.

Identification of stem cell state

Leukocyte activation and cancer malignancy are often associated with changes in cell differentiation state. The unique mechanical signatures for these cells directed us to examine the mechanical properties of embryonic stem cells (ESCs). It is currently difficult to confidently

discriminate embryonic stem cells³⁶ and induced pluripotent stem cells (IPSC)³⁷, which are being explored for use in cell-based regenerative medicine, from their differentiated progeny using solely biochemical markers. These markers, including SSEA4, OCT4, and NANOG³⁸, exhibit significant overlap and variable expression over orders of magnitude when measured with flow cytometry (see Supplemental Text for further discussion). We were able to classify stem cells and their differentiated progeny using our high-throughput deformability measurement. Previously, small sample sizes of mouse ESCs (mESCs) and human ESCs (hESCs) and their nuclei were found to be more deformable than their differentiated progeny using atomic force microscopy and micropipette aspiration, suggesting deformability may be a viable biomarker for pluripotency^{5,6}. Here, with orders of magnitude higher throughput and statistical significance, we show that differentiated cells generated from mESCs by two alternate methods of differentiation including adherent (median deformability=1.28; N=3,427) and embryoid body (EB) differentiation protocols (1.54; N=1,046) are less deformable than undifferentiated mESC (1.68; N=3,535) (see Fig. 3a,c). Furthermore, we confirmed this trend with hESCs (median deformability=1.82; N=2,523) and hESCs differentiated using an adherent differentiation protocol for 9 days (1.48; N=1,718) and 14 days (1.59; N=2,283; Fig. 3d,h). Interestingly, mESC and hESC were both more deformable than the lowest viscosity emulsions that we were able to measure ($\lambda < 480$). Differentiation of hESCs was confirmed by an absence of alkaline phosphatase (AP), reduced expression of SSEA4 and TRA1-60 observed by flow cytometry, and a reduction of OCT4 protein on days 9 and 14 of the protocol (Fig. 3e-g). Differentiation of mESCs was confirmed by a reduction of OCT4 protein after EB and adherent differentiation protocols (Fig. 3b). Our data suggest that the deformability biomarker is an earlier indicator of differentiation that precedes loss of OCT4 expression in hESCs given that a statistically

significant decrease in deformability for day 9 differentiated cells ($p < 0.001$) was observed prior to a reduction in OCT4 protein levels. The ability for a biophysical marker to change prior to molecular markers has been observed in neural³⁹ and mesenchymal stem cells⁴⁰ as well.

A significant capability of our single-cell measurement approach is the ability to observe the distribution of cell behaviors and identify sub-populations within two-dimensional scatter plots - similar to traditional flow cytometry plots. Interestingly, density scatter plots for stem cells reveal one large population centered at a deformability of 1.8, and size of 16 μm (88.9%), and a smaller population at 1.15, 11 μm (10.1%) that corresponds with the smaller fibroblast feeder cells used in culture (Fig. 3d, see Supplemental Figure 6 for a scatter plot for pure fibroblast feeders). After 14 days of differentiation we also notice a broad distribution of sizes and deformability (although generally less deformable) that corresponds to the multiple terminally differentiated lineages. Using this type of multiparametric data we also demonstrated high statistical accuracy of classification for the combination of biophysical biomarkers (i.e. size and deformability). We constructed a classification tree (Supplemental Fig. 7) to identify undifferentiated hESC and 9 day adherent differentiated hESC with the cost of misclassifying an undifferentiated hESC being 4 times greater than misclassifying differentiated cells (i.e. the tree was designed to avoid misclassifying undifferentiated cells as they will be especially dangerous if delivered in vivo). The tree achieved an area under the curve (AUC) of 0.91 with a sensitivity of 0.93 and specificity of 0.88. This is comparable to the classification accuracy of a decision tree derived from flow cytometry data (surface markers for pluripotency): an AUC of 0.84, a sensitivity of 0.82, and a specificity of 0.86.

Cytoskeletal and nuclear origins of deformability

It remains to be seen what molecular changes are responsible for differences in whole cell deformability upon differentiation; however, the nuclear architecture has been implicated and is easily probed with our large deformation amplitudes. Pajeroski et al. found nuclear lamins A and C (intermediate filaments absent from pluripotent cells) contributed to measured increases in nuclear stiffness that occurred as cells matured while the stiffer rheological character of the nucleus was dependent on tighter chromatin packing⁵. In the process of differentiation, cells gain regions of condensed heterochromatin with which nucleoproteins are more closely associated, while these proteins are dynamically associated with a loose chromatin structure in undifferentiated cells⁴¹.

Besides changes in chromatin density and nuclear architecture, cytosolic cytoskeletal components are expected to contribute to cell deformability measurements and response to mechanical stimuli⁴². Using our high-throughput measurement system we studied the effect of cytoskeletal perturbations on whole-cell deformability. We treated human cervical adenocarcinoma cells (HeLa) and NIH 3T3 fibroblasts with pharmacological inhibitors of two cytoskeletal components with roles in regulation of cell shape and motility, a compound shown to reorganize keratin intermediate filament networks, as well as an inhibitor of myosin contractility (blebbistatin) and characterized their resistance to deformation^{43,44}. As shown in Figure 4 and Supplemental Figure 8 treatment with these compounds did not have the profound effects on cell deformability observed in the processes of disease (Figure 2) and differentiation (Figure 3). Depolymerization of actin with latrunculin A, disruption of the microtubule network with nocodazole, and reorganization of keratin networks with sphingosylphosphorylcholine (SPC⁴⁵) resulted in small deviations in deformability from that of untreated cells (Figure 4).

Treatment with blebbistatin, which prevents myosin II from generating contractile stresses in the actin network, resulted in more apparent changes, including an increase in the distribution of deformabilities as well as the presence of a larger more deformable population (size > 20 μm and deformability > 2.2) for both HeLa and 3T3 cells.

Notably, the overall changes in median deformability for all of the cytoskeletal disruptors was small compared to deformability changes observed upon differentiation of stem cells or activation of leukocytes, suggesting that the relative nucleus size, nuclear cytoskeletal components and chromatin structure may be the dominant molecular changes that our large amplitude and strain rate deformations report on. Cell deformation is likely dominated by the viscous properties of cytoplasmic material and chromatin in the cell. This may be expected given that rigid actin networks are known to fluidize at high strains⁴⁶. Beyond the large strains resulting from our method, the large strain rate ($\sim 10^5/\text{s}$) likely affects the observed mechanical properties²⁸. Like for magnetic bead twisting cytometry and laser tracking microrheology²⁹ operating at high frequencies, the observed cell response may be similarly predominantly viscous, and therefore largely independent of cytoskeletal structure. As such, deformability cytometry may complement a low strain, low strain rate method like AFM, which is useful in probing this different regime.

Conclusions

Combined, our results highlight interesting correlations whereby lymphocyte activation and stem cell pluripotency are each associated with increased deformability. Both cell states have been characterized by the presence of loose, open chromatin structures. For a multitude of biophysical questions, the dramatic (>3 orders of magnitude) increase in throughput provided by

deformability cytometry will provide statistically robust answers, enabling new discoveries across fields. Further, for pleural fluid diagnostics an automated assay would: (i) augment traditional cytology and diagnostic routines without requiring additional sample preparation, (ii) limit operator bias, and (iii) provide a standardized and compact measurement (the deformability scatter plot) useful for quantitative communication of disease states between clinicians. The developed microfluidic instrument integrates label-free physical measurements of cells with the massive throughput and statistical significance of flow cytometry, providing a practical realization of a mechanical biomarker in clinical assays.

Materials and Methods

MCF7 cell culture

The MCF7 cell line (ATCC Number: HTB-22) was propagated in DMEM-F12 with 0.01 mg/mL bovine insulin and fetal bovine serum at a final concentration of 10% (v/v). For biomechanical measurements MCF7 cells were released from substrates with 0.25% porcine trypsin and resuspended in culture media at a density between 200,000 and 500,000 cells/mL.

Embryonic stem cell culture

Undifferentiated mESC lines were cultured in 5.0% CO₂ at 37°C on mitomycin C-inactivated CF1 mouse embryonic fibroblast cells (MEFs). Culture medium contained KnockOut Dulbecco's modified Eagle's medium (DMEM), 15% fetal calf serum, 1X non-essential amino acids (Invitrogen/GIBCO, 100X concentration), 1X Pen Strep Glutamine (Invitrogen/GIBCO, 100X concentration), 0.055mM 2-mercaptoethanol (Invitrogen/GIBCO,

1000X concentration, 55mM), and 5×10^5 units leukemia inhibitory factor (Millipore, 10^6 units/ml). Information regarding HSF-1 (46XY) can be obtained at <http://stemcells.nih.gov/stemcells>. Undifferentiated hESC colonies were maintained as previously described⁴⁷. For all experiments, hESCs were used between passages 35 and 60. All hESC experiments were conducted with prior approval from the UCLA Embryonic Stem Cell Research Oversight Committee.

Differentiation of embryonic stem cells

Mouse ESCs were differentiated through either embryoid bodies (EBs) within hanging drops or through adherent culture on gelatin. Differentiation medium contained KnockOut (DMEM), 15% fetal calf serum, 1X non-essential amino acids, 1X Pen Strep Glutamine, and 0.055mM 2-mercaptoethanol. EBs were collected at day 6 for analysis. For adherent culture, 15,000 cells were plated on gelatin-coated six-well plates in mESC differentiation medium. Media was changed at day 4, 5 and 6. At day 7, cells were collected for analysis. Differentiation of hESCs was performed as previously described except without RA treatment⁴⁸. At days 9 and 14, of differentiation, hESCs were collected for analysis.

NIH 3T3 and HeLa cell culture and pharmacological inhibition

NIH 3T3 and HeLa cell lines were maintained in DMEM-F12 with 1% (v/v) penicillin/streptomycin and 10% (v/v) fetal bovine serum. To explore the effects of cytoskeletal components on deformability, we inhibited microtubules with nocodazole, inhibited non-muscle myosin II with blebbistatin, and disrupted actin polymerization with Latrunculin A. Keratin

networks architecture was modified by sphingosylphosphorylcholine (SPC). Cells were incubated in 0.001-10 μ M Latrunculin A, 0.001-10 μ M nocodazole, 0.1-10 μ M SPC, or 5 μ M blebbistatin for 2 hours, prior to the deformability assay. For biomechanical measurements cells were released from culture flasks with 0.25% porcine trypsin and resuspended in culture media at a density between 200,000 and 500,000 cells/mL. Cultured cells were measured immediately ($t < 10$ minutes from harvest) with the deformability cytometer as mechanical properties were observed to change significantly over longer time periods (see ‘Device Operation’).

Western blots

Protein was harvested from undifferentiated and differentiated ESCs using M-PER cell lysis reagent (Thermo Scientific, Rockford, IL). Protein concentration was measured using BCA Protein assay (Thermo Scientific). 3.5 (mouse) and 10 (human) μ g of total protein were electrophoresed through 12% NuPAGE Novex Bis-Tris gels (Invitrogen) and transferred according to standard procedures. For immunoblotting, primary antibodies were goat anti-Oct4 (Santa Cruz Biotechnology) used at a 1:250 dilution and rabbit anti- β -actin (Abcam) used at a 1:5,000 dilution. Secondary donkey polyclonal to goat HRP-conjugate was used at a 1:5,000 dilution and secondary donkey polyclonal to rabbit HRP-conjugate was used at a 1:7,500 dilution. Blots were developed using Amersham ECL Western Blotting Analysis System (GE Healthcare).

Alkaline phosphatase assay

Detection of alkaline phosphatase was performed using Fast Red Salt (Sigma F2768) and Naphthol AS-MX phosphate (Sigma 85-5) dissolved in water.

Preparation and activation of PBMCs and granulocytes

Peripheral blood mononuclear cells (PBMCs) were obtained from normal healthy donors and processed at the UCLA Virology Core Facility. The PBMCs were separated via Ficoll-Paque density gradient (Sigma 1077 Histopaque) and resuspended in RPMI 1640 medium (Sigma) with penicillin-streptomycin and L-glutamine and 50 units/ml of recombinant human Interleukin-2 (NIH AIDS Reagent Repository). The PBMCs were then seeded in a 6 well plate at 10^6 cells per well with or without the addition of an anti-CD3 antibody (12F6) at 0.5 $\mu\text{g/ml}$ or phytohaemagglutinin (PHA; Sigma L9132) at 5 $\mu\text{g/ml}$ to stimulate the PBMCs for three days. For deformability cytometry, the suspended cells from each well were harvested and assayed at a density between 200,000 and 500,000 cells/mL. BD Vacutainer® CPT™ cell preparation tubes were used as prescribed. However, granulocytes were also extracted from below the cell barrier and red blood cells were hypotonically lysed with Red Blood Cell Lysis Buffer as prescribed (Roche Applied Science, Indianapolis, Indiana, USA) in preparation for our assay. Granulocytes were stimulated with 10 μM fMLP for 45 minutes.

Pleural Fluid preparation and analysis

Pleural fluids were obtained from Ronald Reagan UCLA Medical Center and Santa Monica UCLA Medical Center. Cell blocks and cell smears were prepared by traditional

cytological methods. In parallel, a fraction of each sample was concentrated and red blood cells and debris were removed by hypotonic lysis with Red Blood Cell Lysis Buffer as prescribed. The remaining cells were resuspended in culture media at a density between 200,000 and 500,000 cells/mL for the assay.

Microfluidic device fabrication and device dimensions

The devices were designed in AutoCAD (Autodesk, San Rafael, California, USA). Transparency photomasks for these designs were printed at 20,000 dots per inch (CAD/Art Services, Inc., Bandon, Oregon, USA). Molds for replica molding were prepared using these masks in the UCLA Nanoelectronics Research Facility. Negative photoresist, SU-8 50 (MicroChem, Newton, Massachusetts, USA) was spun on a 4 inch Silicon wafer at 4000 rotations per minute. The coated wafer was soft baked at 65°C for 5 minutes then 95°C for 15 minutes. The wafer was then exposed under near UV at 8.0 mW/cm² for 30 seconds. A post exposure bake of the wafer was carried out at 65°C for 2 minutes then at 95°C for 3.5 minutes. The unexposed photoresist was developed in SU-8 Developer (MicroChem) until an isopropyl alcohol rinse produced no white film. The height of the resulting features was characterized by a surface profiler. The width of microchannels immediately before and after the extensional flow region was 67 μm. The height of the features in the device was 28 μm.

The mold was taped to the lower plate of a petri dish with features facing up and an approximately 6 mm layer of Sylgard 184 Silicone Elastomer (Dow Corning, Midland, Michigan, USA), polydimethylsiloxane (PDMS), mixed 10 parts base to 1 part curing agent, was poured on top. The cast mold was placed in a vacuum chamber and the chamber was evacuated

for 30 minutes to remove air from the curing polymer. It was then moved to an oven set to 65°C for 3 hours. The devices were cut from the mold and inlet and outlets were punched into the cured polymer. They were then placed in a plasma cleaner along with slide glasses to be activated. After a 30 second exposure to air plasma the activated surfaces of PDMS and glass were placed in contact to form permanent covalent bonds between the two materials.

Production of droplet models

Saturated, surfactant-stabilized viscous oil-in-water emulsions were created using PDMS oils ($\rho = 960 \text{ kg/m}^3$) of known viscosity by rigorously vortexing PDMS oil at 3% (w/w) with Tween 80 at 3% (w/w) in water. Size was not controlled but droplets were typically sheared to approximately the size of cells by microscale, size-exclusion filters on the microfluidic device. The kinematic viscosity of the PDMS oils ranged from 500 to 10,000 cSt. The Capillary Number ($Ca = \mu U / \sigma$ where μ is the dynamic viscosity of the fluid, U is the droplet velocity, and σ is the surface tension) is used to represent the ratio of viscous stress to interfacial tension²⁷. The interfacial tension of a saturated, surfactant-stabilized emulsion⁴⁹ is $<5 \text{ mJ/m}^2$. Here μ_o and Capillary number are kept constant for all experiments²⁷, but we vary $\lambda = \mu_i / \mu_o$, the ratio of inner to outer viscosity to determine the effect on deformability.

Device operation

Cell suspensions were prepared as described above. The optimal cell density for the devices is between 200,000 and 500,000 cells/mL. In this range there is minimal interaction between cells. Cells were loaded into 5 mL plastic syringes. A 25 gauge luer stub (Instech

Laboratories, Inc., Plymouth Meeting, Pennsylvania, USA) was connected to the syringe and a short length of PEEK tubing (Upchurch Scientific, Oak Harbor, Washington, USA) with an inner diameter of 0.02 inches and an outer diameter of 0.0313 inches was connected to the luer stub. The free end of the tubing was fitted into the open inlet. Equal tubing lengths were inserted into the outlets with free ends directed into a waste receptacle. The syringe was loaded onto a PHD 2000 syringe pump (Harvard Apparatus, Holliston, Massachusetts, USA) and set to inject at a flow rate optimized for the device. A volumetric flow rate of 1,075 $\mu\text{L}/\text{min}$ was selected for the MCF7 and HeLa cell lines and 800 $\mu\text{L}/\text{min}$ for hESCs and mESCs (Figure 3) unless otherwise stated. 900 $\mu\text{L}/\text{min}$ was optimal for prepared blood and pleural fluid samples as well as NIH 3T3 cells. After initiating the injection, imaging was delayed a further 20 seconds to account for fluidic capacitance. Cells migrated across fluid streamlines to the center of the channel due to inertial lift forces. At the junction, an extensional flow was generated. When a cell reached the center of the extensional flow it could be stretched.

After being released from substrates with trypsin, as described above, cell morphology shifted with time. With increasing time, for example topographic features became smoothed most likely as cytoskeletal structures from the adherent state reorganized. These changes were accompanied by a measured shift in deformability. For example HeLa cell deformability increased over a period of several hours. Over shorter time periods of minutes only small changes in deformability were observed (Supplemental Figure 3). We accounted for the time dependence by maintaining a uniform measurement time after bringing cells in suspension, such that measurements of the same cell line (e.g. MCF7) harvested on different days were not statistically different (Supplemental Figure 3).

Microscopy

Cells in flow were magnified with a 10x objective (Nikon Japan 10x/0.30) on a Nikon Eclipse Ti inverted microscope. A digital high-speed video camera, Phantom v7.3 (Vision Research, Inc., Wayne, New Jersey, USA), was connected to the microscope via a c-mount for image capture. Camera settings were controlled with Phantom Camera Control (Vision Research, Inc.). The frame rate of the camera is limited by the chosen pixel resolution. 256x32 pixels was used. The resulting frame rate was 142,857 per second. The minimum allowable exposure time, 1 μ s, was used for both devices. The device was aligned at the center of the field of view. The aperture was half-closed to focus light and reduce scatter. Light intensity was adjusted to maximize the contrast between the cell walls and the exterior fluid.

Data processing

A custom built script in Matlab v2009a (MathWorks, Natick, Massachusetts, USA), was used to automate image analysis, data collection, and post-processing analysis (Supplemental Figure 2). When required, images were processed with Cine Viewer (Vision Research, Wayne, New Jersey, USA) and ImageJ (NIH) to increase contrast and assist the automated image analysis. Image analysis is similar to previously published techniques². Briefly, the image of a cell is mapped from polar to Cartesian coordinates and cell walls are determined by a custom algorithm. This analysis provides a dataset of cell diameters at intervals of 2 degrees. Analysis of each cell begins 4 frames prior to the extensional flow junction. Upon entering the extensional flow junction, the lower cell velocity allows for 360° measurements of the cell diameter where deformability and circularity parameters are determined. In post-processing the

deformability, circularity, and size biomarkers are collected. The cell diameter measurement is determined as the minimum cell diameter at $90^\circ \pm 30^\circ$ measured prior to the flow junction (the walls at $0^\circ \pm 30^\circ$ cannot be visualized due to motion blur at the higher velocity experienced in this part of the channel). The deformability parameter is determined by the ratio of the maximum diameter in the vertical direction at $90^\circ \pm 30^\circ$ to the minimum diameter in the horizontal direction at $0^\circ \pm 30^\circ$. Finally, the circularity parameter $= (4\pi A/P^2)$ is calculated where A is the area of the observed cell, and P is the perimeter of the cell (Figure 1). These parameters are extracted for all frames where the whole cell is visible in the field-of-view, but we chose the maximum value as the representative value for plots and statistics. Our code also collected a variety of statistics concerning cell speed as well as the number of frames cells resided in the extensional flow. We used this data for quality control of device operation and rejected data in which the speed or time within the stretching flow were outside of our accepted normal range. Measurements of cells that had initial diameters greater than or equal to $28 \mu\text{m}$ are discarded as these cells are bigger than the smallest channel dimension and are deforming to fit through the channel. Measurements of cells that had initial diameters that measured less than or equal to $5 \mu\text{m}$ are also discarded as our confidence in these measurements is diminished by the limited number of pixels per cell at this size. Lastly, measurements of cells are omitted when their initial diameters are greater than the third quartile plus 1.5 times the interquartile range or less than the first quartile minus 1.5 times the interquartile range, except for results in Figure 3. Scatter plots were constructed using the `dscatter` function available from the MATLAB File Exchange⁵⁰.

Statistical analysis

All sample comparisons and determinations of statistical significance were performed using the Wilcoxon rank sum test in Matlab (equivalent to the Mann-Whitney U-test). The deformability measure has a lower bound of one, and the circularity measure has an upper bound of one, thus measured populations are asymmetric, non-normally distributed, and using the Wilcoxon rank sum test is appropriate. We also used R to train classification trees to recognize the differences between populations of cells based on various metrics: size, deformability, and circularity or intensity of fluorescently labeled molecular markers measured by flow cytometry^{51,52}. Classification was performed after an initial gating: flow cytometry data was gated by cell optical properties and relevant concentrations of molecular markers of cell death or pluripotency; deformability cytometry data was gated by the probability that a cell was part of the pure population (Supplemental Fig. 7). We then evaluated these trees with the data and created sensitivity/specificity, receiver operating characteristic (ROC) curves, extracting the area under the curve. All trees were constructed weighting the cost of false negatives four times greater than false positives.

Cytoskeletal Staining

All samples were fixed with 4% formaldehyde for 7 minutes, followed by a permeabilization with 0.25% Triton X-100 (Sigma), and 1% bovine serum albumin (Sigma) for 10 minutes. The first staining solution contained rat-anti- α -tubulin primary (Novus Biologicals, CO, USA) with 3 mM magnesium chloride (Sigma), and 10mM EGTA for 3 hours at room temperature. The second staining solution contained goat-anti-rat Alexa Fluor 568 secondary

(Molecular Probes), 800 nM DAPI, and 1.6U FITC-phalloidin in PBS for 3 hours at room temperature.

Acknowledgements

We are grateful to the UCLA Statistics Consulting Center and Sophia Gkountela for helpful discussions. We are also grateful for computing services provided by the UCLA Academic Technology Services High Performance Computing group and the technical assistance of Prakashan Korambath and thank Hwee Ng, Mary Levin, Sean O'Byren, Christopher Johnson, Michael Cutidioc, and Amanda Cokhlin for preparing samples and technical assistance. Support for this project involved funds from the Eli and Edythe Broad Center of Regenerative Medicine and Stem Cell Research (ATC), the David and Lucile Packard Foundation Fellowship (DD) and a DARPA Young Faculty Award (DD).

Figures

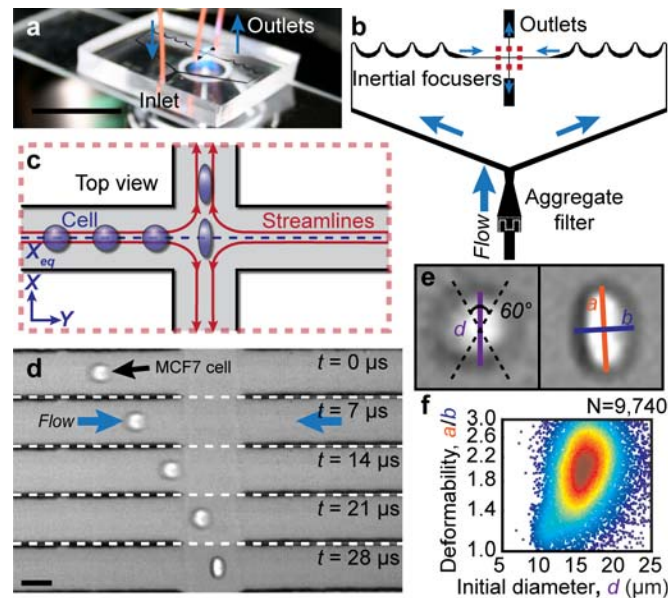


Figure 1. Principles of deformability cytometry. (A) A photograph of the microscope-mounted and fluid-coupled microfluidic deformability cytometry device. Only a single inlet is required. Scale bar is 25 mm. (B) A schematic of the microfluidic device (channel height = 28 μm) that focuses cells to the channel centerline before delivering them to the stretching extensional flow is shown. Cells can enter the extensional flow from both directions. (C) A schematic of the deformation of a cell delivered to the center of an extensional flow by being previously aligned at an inertial focusing position, X_{eq} is shown. (D) High speed microscopic images showing a focused cell entering the extensional flow region. Delivery and stretching occurs in less than 30 μs . Scale bar is 40 μm . (E) Definitions of the shape parameters extracted from images are shown. (F) Density scatter plot of 9,740 size and deformability measurements of single human embryonic stem cells.

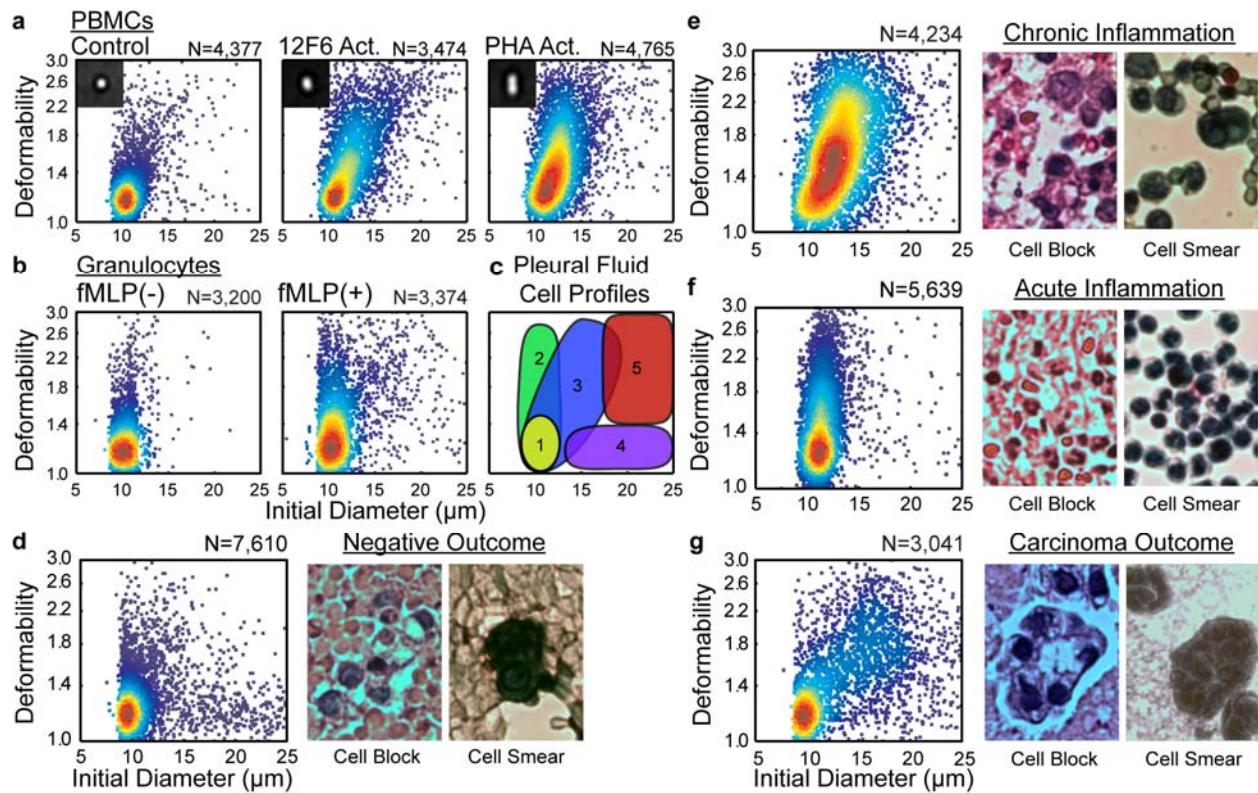


Figure 2. Mechanical measurements help distinguish populations of cells within blood and pleural fluids. (A) Density scatter plots of the size and deformability of untreated PBMCs and PBMCs stimulated with 12F6 or PHA. (B) Density scatter plots of the size and deformability of untreated granulocytes and granulocytes stimulated with fMLP. (C) Locations of cell populations found in pleural fluids on a size-deformability map: (1) Non-Activated Leukocytes, (2) Non-Activated Leukocytes, (3) Activated Mononuclear Cells, (4) Mesothelial Cells, (5) Suspicious Cells. (D) Density scatter plot of the size and deformability of cells within pleural fluid of a patient diagnosed negative for carcinoma (left) and typical cell blocks and smears for this diagnosis. (E) Density scatter plot of the size and deformability of cells within pleural fluid of a patient diagnosed negative for carcinoma but with chronic inflammation (left) and typical cell blocks and smears for this diagnosis. (F) Density scatter plot of the size and deformability of cells within pleural fluid of a patient diagnosed negative for carcinoma but with acute

inflammation (left) and typical cell blocks and smears for this diagnosis. (G) Density scatter plot of the size and deformability of cells within pleural fluid of a patient diagnosed positive for carcinoma (left) and typical cell blocks and smears for this diagnosis.

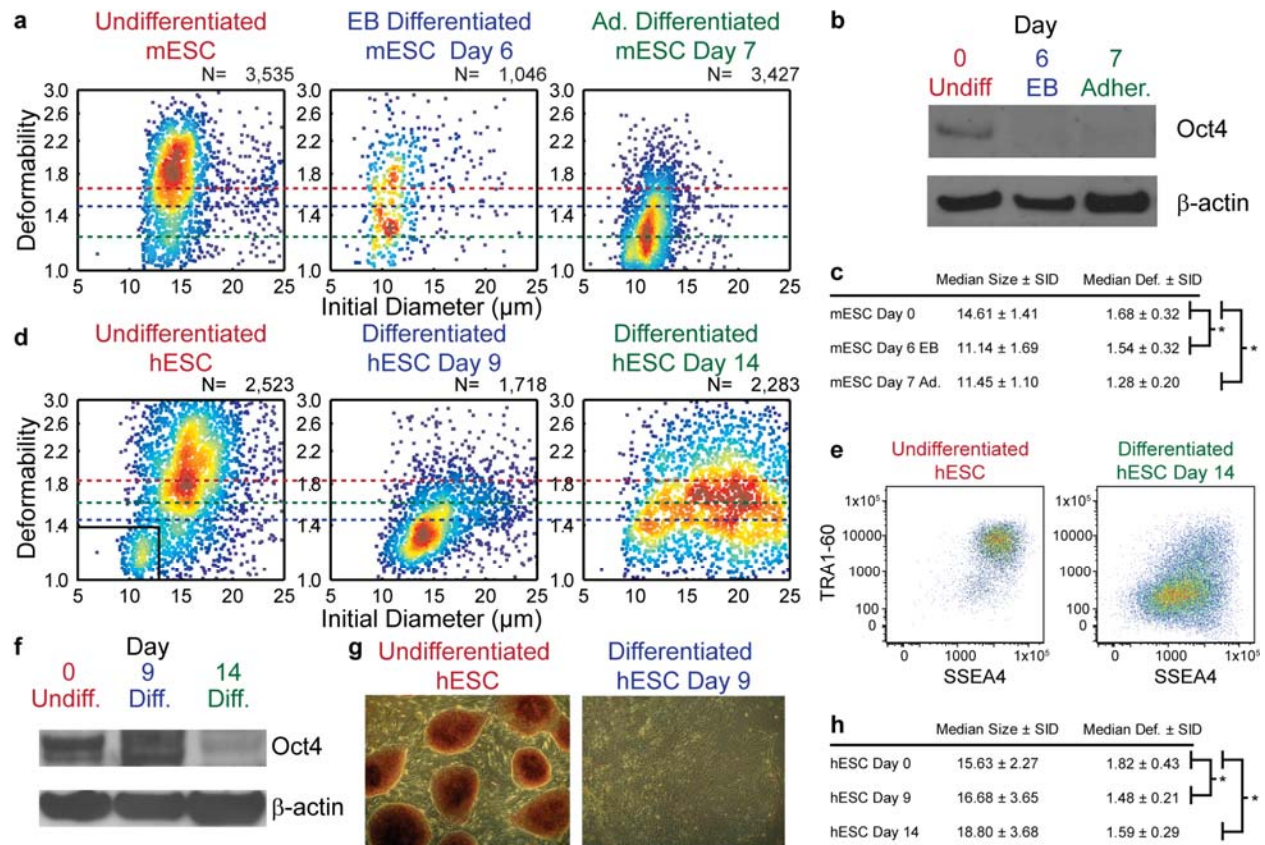


Figure 3. Increased deformability is correlated with increased pluripotency. (A) Density scatter plots of the size and deformability of undifferentiated mESCs, and mESCs differentiated by embryoid body (EB) and adherent methods. (B) Cell extracts from undifferentiated day 0 and differentiated day 6 (EB) and day 7 (adherent) mESCs were analyzed for Oct4 protein expression. Decreased Oct4 protein in differentiated mESCs was confirmed by Western blot analysis with anti-actin antibodies as a loading control. (C) Median and Semi Interquartile Deviation (SID) statistics of mESC measurements in part a; * Wilcoxon ranked sum, $p < 0.001$. (D) Density scatter plots of the size and deformability of undifferentiated hESCs, and hESCs differentiated adherently for 9 days and 14 days. (E) Differentiation of hESCs is accompanied by reduced expression of SSEA4 and TRA1-60, although significant overlap is observed between populations. (F) Decreased Oct4 protein in differentiated hESCs was confirmed by Western blot

analysis with anti-actin antibodies as a loading control. (G) Differentiation of hESCs was also confirmed by an absence of staining by alkaline phosphatase (AP). (H) Median and Semi Interquartile Deviation (SID) statistics of hESC measurements in part a; * Wilcoxon ranked sum, $p < 0.001$.

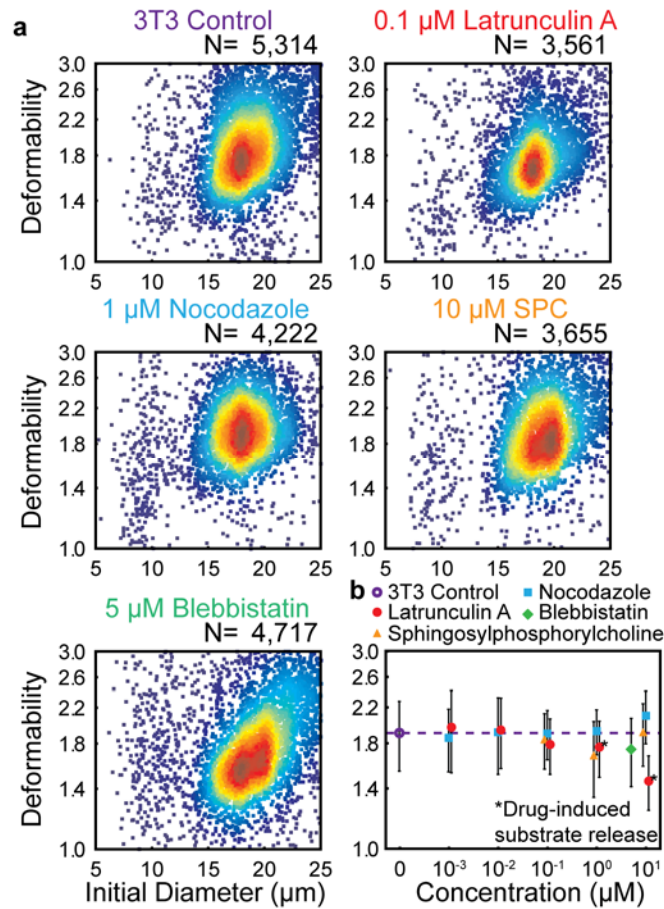
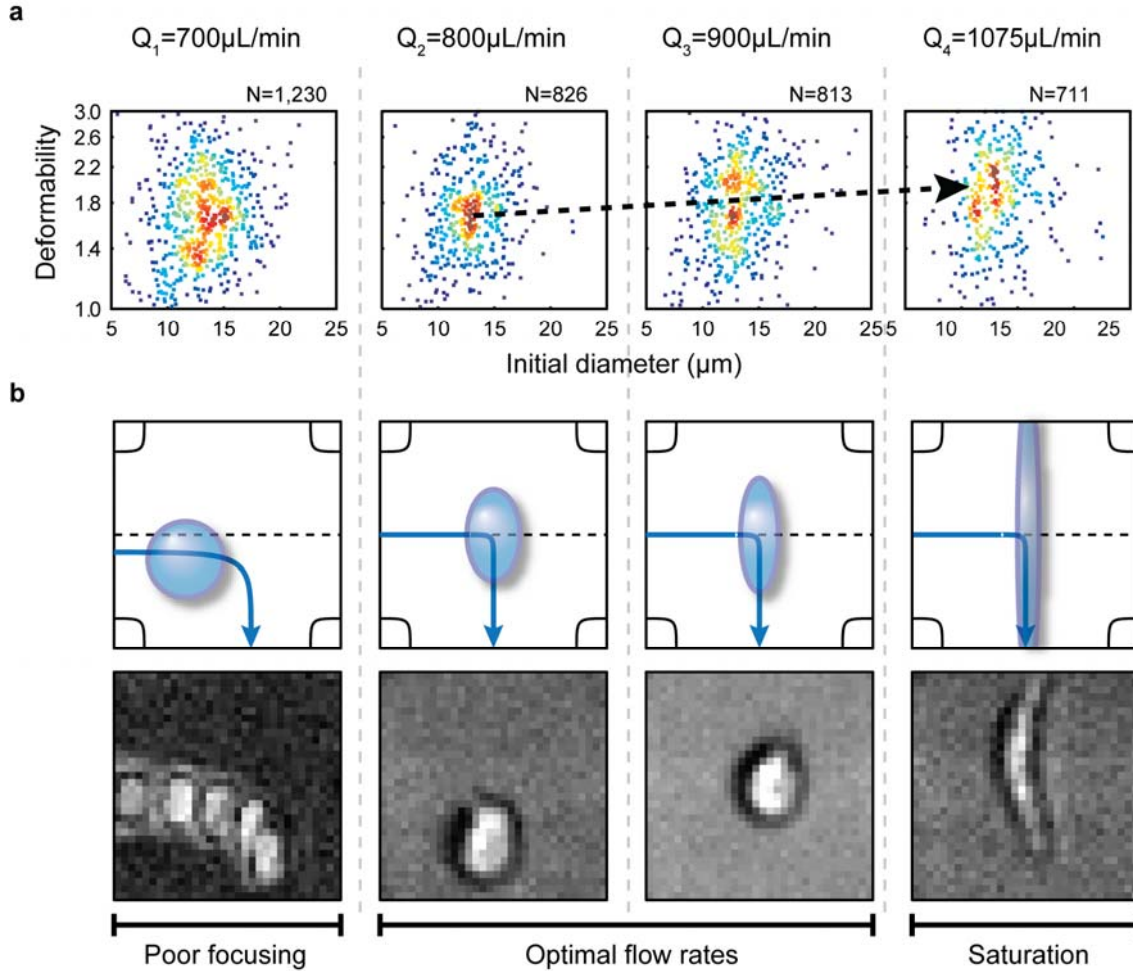
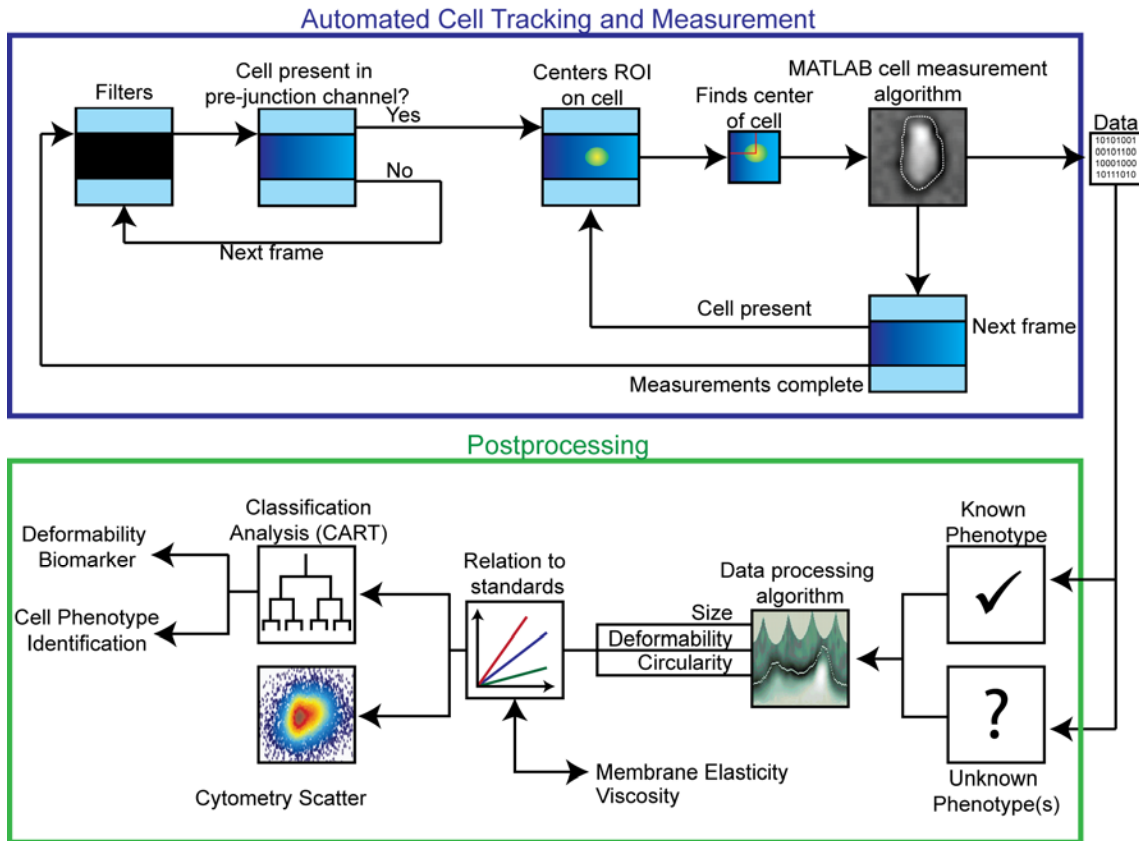


Figure 4. Effects of individual cytoskeletal components on whole cell deformability. (A) Density scatter plots of the initial diameter and deformability of untreated NIH 3T3 cells (control), 3T3 cells treated with latrunculin A, nocodazole, sphingosylphosphorylcholine, and blebbistatin for 2 hours. (B) Median and Semi Interquartile Deviation (SID) statistics of untreated 3T3 cells and 3T3 cells treated with different concentrations of one of four compounds for 2 hours (error bars are SID). “Drug-induced substrate release” indicates that cells detached from the substrate into suspension before the 2 hour treatment period elapsed.

Supporting Figures

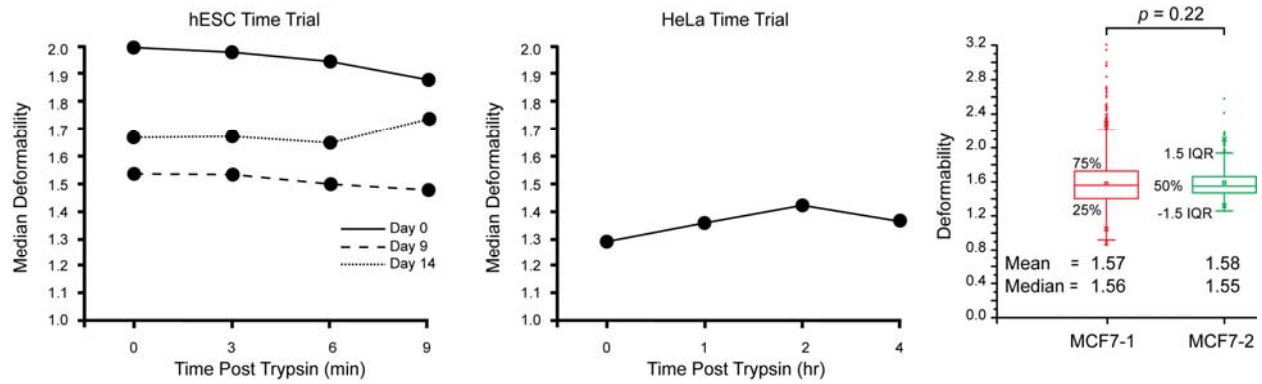


Supplemental Figure 1. Tuning of deformability measurements with flow rate. (A) The deformability of undifferentiated and differentiated hESC_s increases with flow rate, but analysis at too low or high flow rates result in inconsistent measurements (i.e. higher SIDs). (B) The cells exhibit non-uniform trajectories at low flow rates resulting in non-uniform mechanical stretching (left – notice the larger scatter over the deformability axis). At high flow rates the cells can be stretched beyond the imaging window resulting in saturation of the measurement (right). In an optimal range of flow rates the cells reach the center of the extensional flow where they deform a non-saturating amount.

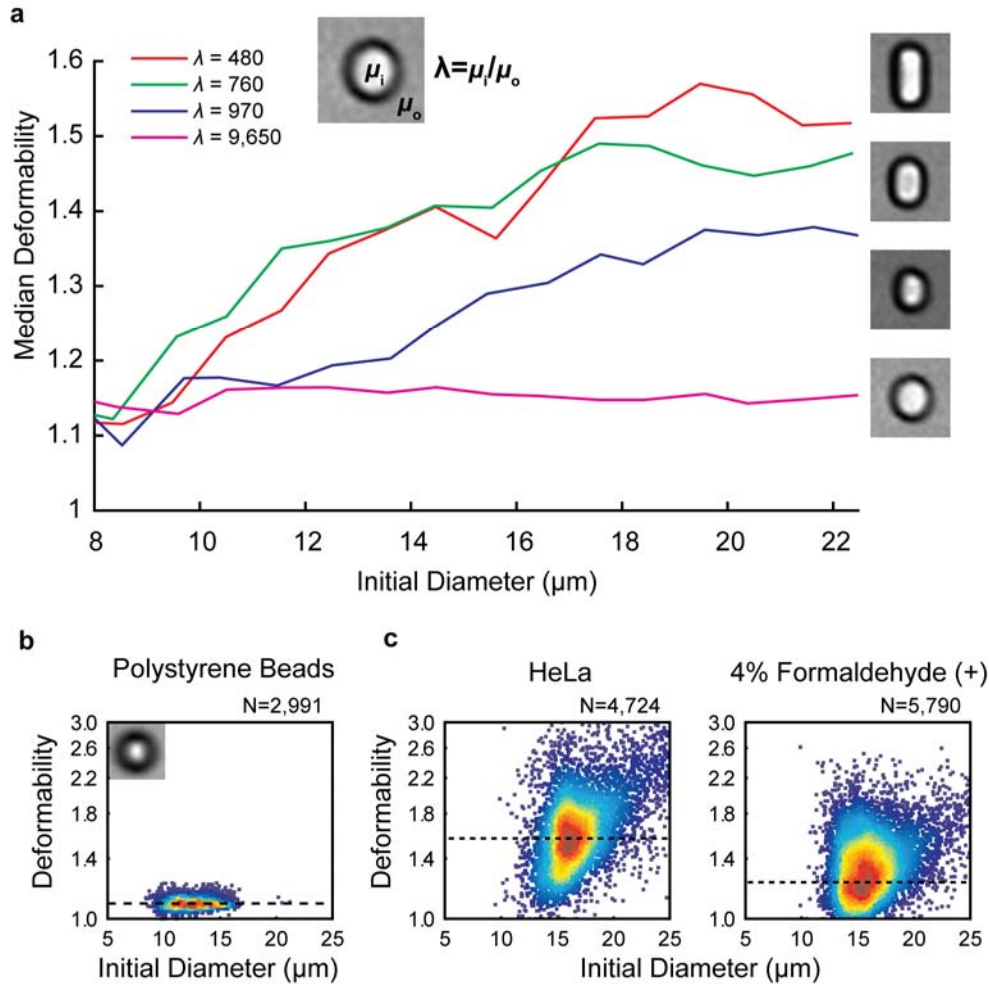


Supplemental Figure 2. Schematic of the automated image processing conducted to obtain and analyze cell deformability biomarkers. A custom MATLAB image analysis script performs image processing and data collection on each 1.8 second experiment totaling 260,000 frames, with expected individual measures for 1,000 to 5,000 cells. Preprocessing image filters are used to enhance cell identification by adjusting contrast, gamma, brightness, and using Fourier space filtering techniques. To collect data, a fixed field-of-view is positioned in the pre-junction area. When a cell enters this field-of-view, a centering algorithm identifies the cell center based on the cell position, shape, and local intensities. Once the cell center has been identified, the field-of-view is cropped and resized 10X to increase the accuracy of measurements to sub-pixel resolution. The image is then mapped from a polar to Cartesian coordinate system. The cell walls are found by examining changes in the intensity derivatives, and diameters are extracted

every 4°. The tracking algorithm then proceeds to the next frame to continue measurements until the cell leaves the deformation inducing extensional-flow region. After data collection the analysis of the parameters: initial diameter, deformability, and circularity is performed. By taking the initial diameter measurement from the vertical axis, noise due to blur attributed to high velocities in the horizontal direction is prevented. As the cell enters the extensional-flow region and changes trajectory the deformability and circularity parameters are measured. The dataset is then plotted as a 2D scatter for visual interpretation and/or tested in classification and regression tree analysis to determine cell type or establish cell type-specific deformability biomarker characteristics for future classification.

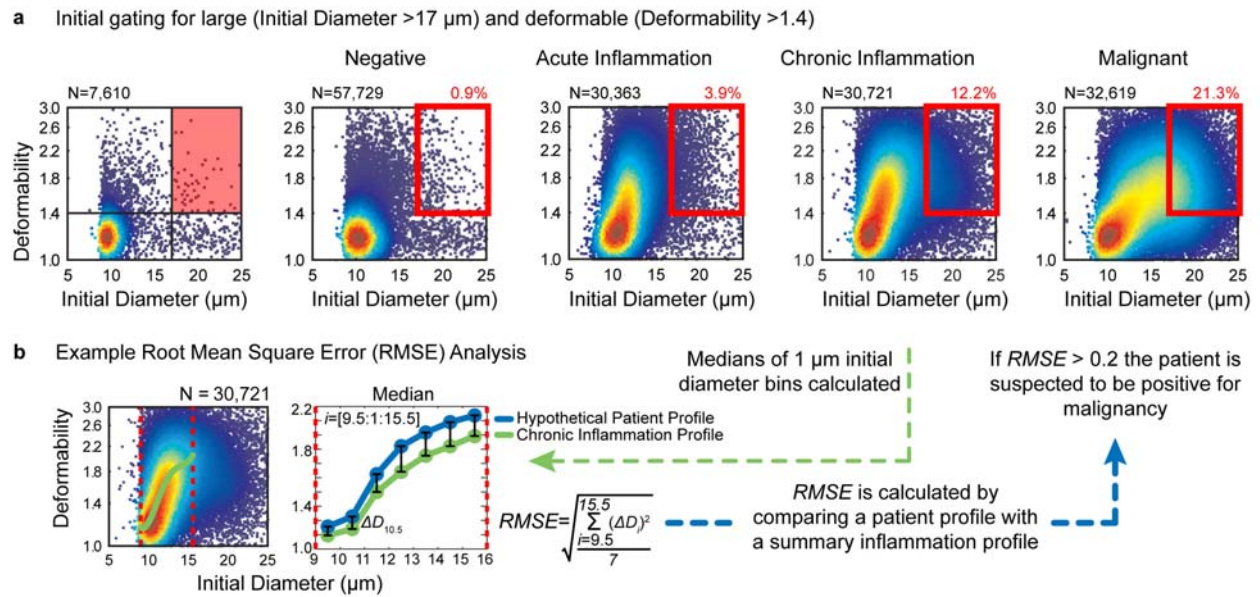


Supplemental Figure 3. Time dependence of the deformability measurement for adherent cell lines. Over short time scales (minutes), hESCs generally have little change in deformability but tend to be slightly less deformable (left). Over longer time scales (hours), HeLa cells become more deformable over time (center). MCF7 cells from different cultures were harvested and measured resulting in no statistical difference in median deformability when measured at a similar time after being brought into solution (right; $p=0.22$).

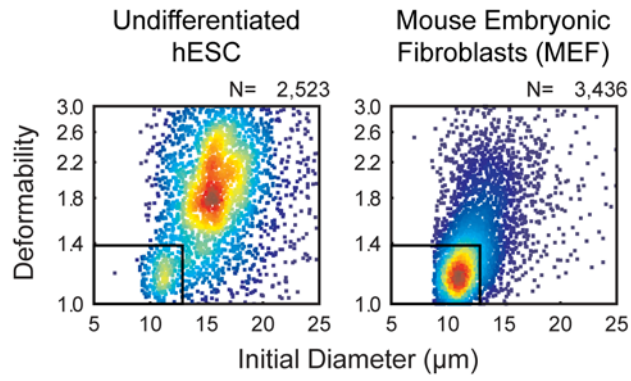


Supplemental Figure 4. Deformation measurements for model systems. (A) The deformability of surfactant-stabilized, oil-in-water emulsions depends on the viscosity of the silicone oil component and the initial diameter of emulsions before deformation (i.e. less viscous droplets deform more). Two parameters, Capillary number, the ratio of viscous vs. interfacial stresses, and the viscosity ratio, λ , can affect deformability. Here μ_o and Capillary number are kept constant for all experiments²⁷, but we vary $\lambda = \mu_i / \mu_o$, the ratio of inner to outer viscosity to determine the effect on deformability. Below $\lambda = 0.8$ the device fails to distinguish between viscosities. Larger droplets are also more deformable. (B) Deformability of polystyrene microspheres. The median deformability is 1.09. This systematic shift above 1 can be attributed

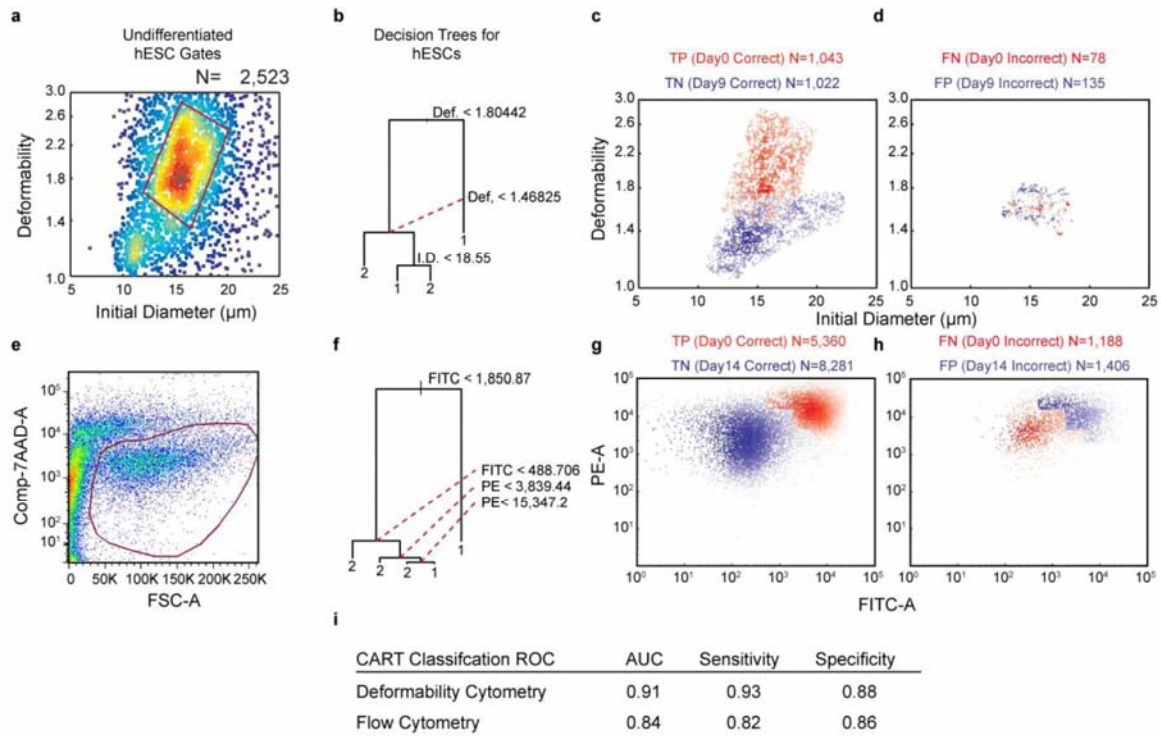
to a 1 μ s exposure blur in the direction of particle motion and does not affect our relative measurements with cells. (C) Chemical cross-linking of proteins increased the stiffness of HeLa cells. Note, the flow rate here is lower (900 μ L/min) than used to deform HeLa treated with cytoskeleton-acting drugs.



Supplemental Figure 5. Pleural fluid diagnostic classification protocol. (A) An initial gating by diameter and deformability is performed. The composite scatter profiles are depicted and gated cell percentages displayed. (B) When greater than 1% of a patient’s cells lie within the initial gate the patient’s profile is compared to a standard (composite) inflammation profile within the initial diameter range where deformability is especially dynamic. A root-mean-square error (RMSE) is calculated. If the RMSE is greater than 0.2, the profile is regarded as substantially different from the inflammation cases which we have observed and is classified as malignant.

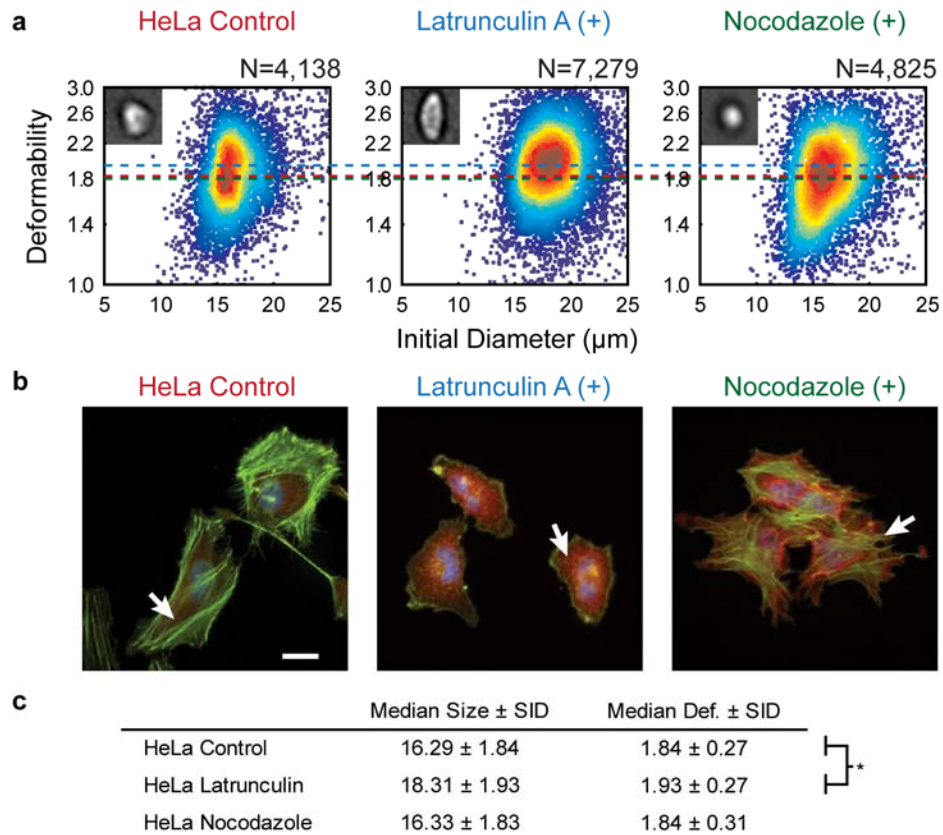


Supplemental Figure 6. Composition of hESC cultures. Mouse embryonic fibroblasts (MEFs) make up a small less deformable subpopulation in hESC cultures.

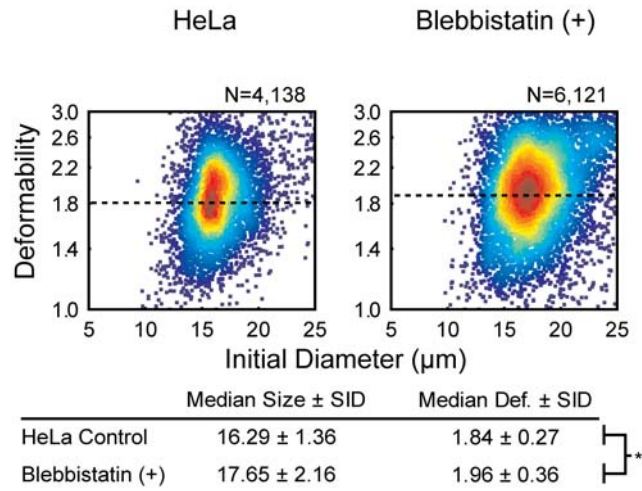


Supplemental Figure 7. Decision trees for classifying single hESC cells by their degree of differentiation (day 0 versus day 9 (deformability cytometry) or day 14 (flow cytometry)). (A) Initial probabilistic gating of deformability cytometry data to define populations. (B) Algorithmically generated decision tree to classify unknown cells by their deformability, size and circularity, pruned to limit false negatives (especially dangerous in the application of stem cell quality control). (C) Density scatter plot of true positives (TP) and true negatives (TN) classified by the deformability cytometry-derived decision tree. (D) Density scatter plot of false positives (FP) and false negatives (FN) classified by the deformability cytometry-derived decision tree. (E) Initial gating of flow cytometry data by optical properties (FSC-A) and viability (Comp-7AAD-A). (F) Algorithmically generated decision tree to classify unknown cells by the concentration of surface pluripotency markers, pruned to limit false negatives. (G) Density scatter plot of true positives (TP) and true negatives (TN) classified by the flow cytometry-derived decision tree. (H) Density scatter plot of false positives (FP) and false

negatives (FN) classified by the flow cytometry-derived decision tree. (i) Classification accuracy statistics.



Supplemental Figure 8. Effects of individual cytoskeletal components on whole cell deformability. (A) Density scatter plots of the size and deformability of untreated HeLa cells (control), HeLa cells treated with latrunculin A, and HeLa cells treated with nocodazole. (B) Fluorescently stained DNA (DAPI), tubulin (TRITC) and F-actin (FITC) in adhered, untreated HeLa cells (control), HeLa cells treated with latrunculin A, and HeLa cells treated with nocodazole. The depolymerization of actin stress fibers (left arrow) resulting in the loss of filaments (indicated by arrow at the center) results in a slightly increased median deformability, while actin reorganization (indicated by arrow at right) in cells with depolymerized microtubules did not statistically alter median deformability, but leads to a smaller population with lower deformability. Scale bar is 50 μm . (C) Median and Semi Interquartile Deviation (SID) statistics of untreated and treated HeLa measurements in part a; * Wilcoxon ranked sum, $p < 0.001$.



Supplemental Figure 9. Inactivation of myosin II with blebbistatin in HeLa cells. Density scatter plots of the size and deformability of untreated HeLa cells (control) and HeLa cells treated with 5 μM of blebbistatin. * Wilcoxon ranked sum, $p < 0.001$.

<i>Patient #</i>	<i>Cytology Results</i>		<i>Deformability cytometry</i>
	<i>Inflammation</i>	<i>Malignancy Origin</i>	<i>Predicted Diagnosis</i>
1	<i>Acute</i>	<i>N</i>	<i>N</i>
2	<i>Acute</i>	<i>N</i>	<i>N</i>
3	<i>Acute</i>	<i>N</i>	<i>N</i>
4	<i>Acute</i>	<i>N</i>	<i>N</i>
5	<i>Acute</i>	<i>N</i>	<i>N</i>
6	<i>Acute</i>	<i>N</i>	<i>N</i>
7	<i>Acute</i>	<i>N</i>	<i>N</i>
8	<i>Chronic</i>	<i>N</i>	<i>N</i>
9	<i>Chronic</i>	<i>N</i>	<i>N</i>
10	<i>Chronic</i>	<i>N</i>	<i>N</i>
11	<i>Chronic</i>	<i>N</i>	<i>N</i>
12	<i>Chronic</i>	<i>N</i>	<i>N</i>
13	<i>Chronic</i>	<i>N</i>	<i>N</i>
14	<i>Chronic</i>	<i>N</i>	<i>N</i>
15	<i>Chronic</i>	<i>N</i>	<i>N</i>
16	<i>Chronic</i>	<i>N</i>	<i>N</i>
17	<i>Chronic</i>	<i>N</i>	<i>M*</i>
18	<i>Chronic</i>	<i>N</i>	<i>M*</i>
19	<i>Mixed</i>	<i>N</i>	<i>N</i>
20	-	<i>N</i>	<i>N</i>
21	-	<i>N</i>	<i>N</i>
22	-	<i>N</i>	<i>N</i>
23	-	<i>N</i>	<i>N</i>
24	-	<i>N</i>	<i>N</i>
25	-	<i>N</i>	<i>N</i>
26	-	<i>N</i>	<i>N</i>
27	-	<i>N</i>	<i>N</i>
28	-	<i>N</i>	<i>N</i>
29	-	<i>N</i>	<i>N</i>
30	-	<i>N</i>	<i>N</i>
31	-	<i>N</i>	<i>N</i>
32	-	<i>N</i>	<i>N</i>
33	-	<i>N</i>	<i>N</i>
34	-	<i>N</i>	<i>M*</i>
35	-	<i>N</i>	<i>M*</i>
36	-	<i>N</i>	<i>M*</i>
37	<i>Chronic</i>	<i>M-Gastrointestinal</i>	<i>M</i>

38	-	<i>M-Breast</i>	<i>M</i>
39	-	<i>M-Ovary</i>	<i>M</i>
40	-	<i>M-Ovary, Lung</i>	<i>N*</i>
41	-	<i>M-Lung</i>	<i>M</i>
42	-	<i>M-Lung, Gastrointestinal</i>	<i>M</i>
43	-	<i>M-Lung</i>	<i>M</i>
44	-	<i>M-Ovary</i>	<i>M</i>
45	-	<i>M-Lung</i>	<i>M</i>
46	-	<i>M-Pancreatic</i>	<i>M</i>
47	-	<i>M-Mesothelioma</i>	<i>M</i>

Supplemental Table 1. Summary of clinical outcomes and deformability cytometry predicted outcomes for pleural effusion samples (N=47). Analysis by the cytology lab yields inflammation state (acute, chronic, and mixed) and the presence of malignancy (N-Negative, M-Malignancy)—the originating source listed. Based on initial diameter and size gating and RMSE analysis pleural fluids are predicted to be negative or positive for malignancy. A 91% sensitivity and 86% specificity was achieved. The * indicator marks incorrectly diagnosed samples.

Bibliography

1. Suresh, S., Spatz, J., Mills, J. P., Micoulet, A., Dao, M., Lim, C. T., Beil, M. & Seufferlein, T. (2005). Connections between single-cell biomechanics and human disease states: gastrointestinal cancer and malaria. *Acta Biomater* 1:15–30. DOI:10.1016/j.actbio.2004.09.001
2. Guck, J. *et al.* (2005). Optical Deformability as an Inherent Cell Marker for Testing Malignant Transformation and Metastatic Competence. *Biophysical Journal* 88:3689–3698. DOI:10.1529/biophysj.104.045476
3. Cross, S. E., Jin, Y.-S., Rao, J. & Gimzewski, J. K. (2007). Nanomechanical analysis of cells from cancer patients. *Nat Nano* 2:780–783. DOI:10.1038/nnano.2007.388
4. They, M. & Bornens, M. (2008). Get round and stiff for mitosis. *HFSP J.* 2:65–71. DOI:10.2976/1.2895661
5. Pajerowski, J. D., Dahl, K. N., Zhong, F. L., Sammak, P. J. & Discher, D. E. (2007). Physical plasticity of the nucleus in stem cell differentiation. *Proceedings of the National Academy of Sciences* 104:15619–15624. DOI:10.1073/pnas.0702576104
6. Chowdhury, F., Na, S., Li, D., Poh, Y.-C., Tanaka, T. S., Wang, F. & Wang, N. (2010). Material properties of the cell dictate stress-induced spreading and differentiation in embryonic stem cells. *Nat Mater* 9:82–88. DOI:10.1038/nmat2563
7. Khismatullin, D. B. (2009). Chapter 3 The Cytoskeleton and Deformability of White Blood Cells. *Current Topics in Membranes* Volume 64:47–111
8. Liu, Z., Cumberland, W. G., Hultin, L. E., Kaplan, A. H., Detels, R. & Giorgi, J. V. (1998). CD8+ T-lymphocyte activation in HIV-1 disease reflects an aspect of pathogenesis distinct from viral burden and immunodeficiency. *J. Acquir. Immune Defic. Syndr. Hum. Retrovirol* 18:332–340
9. Gregson, A. L. *et al.* (2008). Bronchoalveolar immunologic profile of acute human lung transplant allograft rejection. *Transplantation* 85:1056–1059. DOI:10.1097/TP.0b013e318169bd85
10. Di Carlo, D. (2012). A Mechanical Biomarker of Cell State in Medicine. *Journal of Laboratory Automation* 17:32–42. DOI:10.1177/2211068211431630

11. Kim, D.-H., Wong, P. K., Park, J., Levchenko, A. & Sun, Y. (2009). Microengineered Platforms for Cell Mechanobiology. *Annu. Rev. Biomed. Eng.* 11:203–233. DOI:10.1146/annurev-bioeng-061008-124915
12. Rosenbluth, M. J., Lam, W. A. & Fletcher, D. A. (2008). Analyzing cell mechanics in hematologic diseases with microfluidic biophysical flow cytometry. *Lab Chip* 8:1062. DOI:10.1039/b802931h
13. Di Carlo, D. & Lee, L. P. (2006). Dynamic Single-Cell Analysis for Quantitative Biology. *Analytical Chemistry* 78:7918–7925. DOI:10.1021/ac069490p
14. Sraj, I., Eggleton, C. D., Jimenez, R., Hoover, E., Squier, J., Chichester, J. & Marr, D. W. M. (2010). Cell deformation cytometry using diode-bar optical stretchers. *J Biomed Opt* 15:. DOI:10.1117/1.3470124
15. Chen, J. *et al.* (2011). Classification of cell types using a microfluidic device for mechanical and electrical measurement on single cells. *Lab Chip* 11:3174–3181. DOI:10.1039/C1LC20473D
16. Bow, H., Pivkin, I. V., Diez-Silva, M., Goldfless, S. J., Dao, M., Niles, J. C., Suresh, S. & Han, J. (2011). A microfabricated deformability-based flow cytometer with application to malaria. *Lab Chip* 11:1065–1073. DOI:10.1039/c0lc00472c
17. Abkarian, M., Faivre, M. & Stone, H. A. (2006). High-speed microfluidic differential manometer for cellular-scale hydrodynamics. *PNAS* 103:538–542. DOI:10.1073/pnas.0507171102
18. Bao, N., Zhan, Y. & Lu, C. (2008). Microfluidic Electroporative Flow Cytometry for Studying Single-Cell Biomechanics. *Analytical Chemistry* 80:7714–7719. DOI:10.1021/ac801060t
19. Rowat, A. C., Lammerding, J., Herrmann, H. & Aebi, U. (2008). Towards an integrated understanding of the structure and mechanics of the cell nucleus. *BioEssays* 30:226–236. DOI:10.1002/bies.20720
20. Gossett, D. R. & Di Carlo, D. (2009). Particle focusing mechanisms in curving confined flows. *Anal. Chem* 81:8459–8465. DOI:10.1021/ac901306y

21. Di Carlo, D., Irimia, D., Tompkins, R. G. & Toner, M. (2007). Continuous inertial focusing, ordering, and separation of particles in microchannels. *Proc. Natl. Acad. Sci. U.S.A* 104:18892–18897. DOI:10.1073/pnas.0704958104
22. Di Carlo, D. (2009). Inertial microfluidics. *Lab Chip* 9:3038–3046
23. Perkins, T. T., Smith, D. E. & Chu, S. (1997). Single Polymer Dynamics in an Elongational Flow. *Science* 276:2016–2021. DOI:10.1126/science.276.5321.2016
24. Dylla-Spears, R., Townsend, J. E., Jen-Jacobson, L., Sohn, L. L. & Muller, S. J. (2010). Single-molecule sequence detection via microfluidic planar extensional flow at a stagnation point. *Lab Chip* doi:10.1039/b926847b. DOI:10.1039/b926847b
25. Wottawah, F., Schinkinger, S., Lincoln, B., Ananthakrishnan, R., Romeyke, M., Guck, J. & K♦s, J. (2005). Optical Rheology of Biological Cells. *Phys. Rev. Lett.* 94:098103. DOI:10.1103/PhysRevLett.94.098103
26. Stone, H. A. & Leal, L. G. (1989). A note concerning drop deformation and breakup in biaxial extensional flows at low reynolds numbers. *Journal of Colloid and Interface Science* 133:340–347. DOI:10.1016/S0021-9797(89)80042-6
27. Mortazavi, S. & Tryggvason, G. (2000). A Numerical Study of the Motion of Drops in Poiseuille Flow. Part 1. Lateral Migration of One Drop. *Journal of Fluid Mechanics* 411:325–350. DOI:10.1017/S0022112099008204
28. Hoffman, B. D. & Crocker, J. C. (2009). Cell Mechanics: Dissecting the Physical Responses of Cells to Force. *Annu. Rev. Biomed. Eng.* 11:259–288. DOI:10.1146/annurev.bioeng.10.061807.160511
29. Massiera, G., Citters, K. M. V., Biancaniello, P. L. & Crocker, J. C. (2007). Mechanics of Single Cells: Rheology, Time Dependence, and Fluctuations. *Biophysical Journal* 93:3703–3713. DOI:10.1529/biophysj.107.111641
30. Remmerbach, T. W., Wottawah, F., Dietrich, J., Lincoln, B., Wittekind, C. & Guck, J. (2009). Oral Cancer Diagnosis by Mechanical Phenotyping. *Cancer Res* 69:1728–1732. DOI:10.1158/0008-5472.CAN-08-4073
31. Sahn, S. A. (2008). The value of pleural fluid analysis. *Am. J. Med. Sci* 335:7–15. DOI:10.1097/MAJ.0b013e31815d25e6

32. PORCEL, J. M. (2011). Pearls and myths in pleural fluid analysis. *Respirology* 16:44–52. DOI:10.1111/j.1440-1843.2010.01794.x
33. Brown, M. J., Hallam, J. A., Colucci-Guyon, E. & Shaw, S. (2001). Rigidity of Circulating Lymphocytes Is Primarily Conferred by Vimentin Intermediate Filaments. *The Journal of Immunology* 166:6640–6646
34. Vicente-Manzanares, M. & Sanchez-Madrid, F. (2004). Role of the cytoskeleton during leukocyte responses. *Nat Rev Immunol* 4:110–122. DOI:10.1038/nri1268
35. Worthen, G., Schwab, B., Elson, E. & Downey, G. (1989). Mechanics of stimulated neutrophils: cell stiffening induces retention in capillaries. *Science* 245:183–186. DOI:10.1126/science.2749255
36. Thomson, J. A., Itskovitz-Eldor, J., Shapiro, S. S., Waknitz, M. A., Swiergiel, J. J., Marshall, V. S. & Jones, J. M. (1998). Embryonic Stem Cell Lines Derived from Human Blastocysts. *Science* 282:1145–1147. DOI:10.1126/science.282.5391.1145
37. Maherali, N. *et al.* (2007). Directly Reprogrammed Fibroblasts Show Global Epigenetic Remodeling and Widespread Tissue Contribution. *Cell Stem Cell* 1:55–70. DOI:10.1016/j.stem.2007.05.014
38. Adewumi, O. *et al.* (2007). Characterization of human embryonic stem cell lines by the International Stem Cell Initiative. *Nat. Biotechnol* 25:803–816. DOI:10.1038/nbt1318
39. Keung, A. J., de Juan-Pardo, E. M., Schaffer, D. V. & Kumar, S. (2011). Rho GTPases mediate the mechanosensitive lineage commitment of neural stem cells. *Stem Cells* 29:1886–1897. DOI:10.1002/stem.746
40. Fu, J., Wang, Y.-K., Yang, M. T., Desai, R. A., Yu, X., Liu, Z. & Chen, C. S. (2010). Mechanical regulation of cell function with geometrically modulated elastomeric substrates. *Nat Meth* 7:733–736. DOI:10.1038/nmeth.1487
41. Meshorer, E. & Misteli, T. (2006). Chromatin in pluripotent embryonic stem cells and differentiation. *Nat Rev Mol Cell Biol* 7:540–546. DOI:10.1038/nrm1938
42. Suresh, S. (2007). Biomechanics and biophysics of cancer cells. *Acta Biomater* 3:413–438. DOI:10.1016/j.actbio.2007.04.002

43. Sen, S. & Kumar, S. (2009). Cell–Matrix De-Adhesion Dynamics Reflect Contractile Mechanics. *Cel. Mol. Bioeng.* 2:218–230. DOI:10.1007/s12195-009-0057-7
44. They, M., Racine, V., Pepin, A., Piel, M., Chen, Y., Sibarita, J.-B. & Bornens, M. (2005). The extracellular matrix guides the orientation of the cell division axis. *Nat Cell Biol* 7:947–953. DOI:10.1038/ncb1307
45. Beil, M. *et al.* (2003). Sphingosylphosphorylcholine regulates keratin network architecture and visco-elastic properties of human cancer cells. *Nat Cell Biol* 5:803–811. DOI:10.1038/ncb1037
46. Janmey, P. A., Ursula, E., Traub, P. & Schliwa, M. (1991). Viscoelastic properties of vimentin compared with other filamentous biopolymer networks. *J Cell Biol* 113:155–160
47. Clark, A. T., Bodnar, M. S., Fox, M., Rodriguez, R. T., Abeyta, M. J., Firpo, M. T. & Pera, R. A. R. (2004). Spontaneous differentiation of germ cells from human embryonic stem cells in vitro. *Human Molecular Genetics* 13:727–739. DOI:10.1093/hmg/ddh088
48. Ambartsumyan, G., Gill, R. K., Perez, S. D., Conway, D., Vincent, J., Dalal, Y. & Clark, A. T. (2010). Centromere protein A dynamics in human pluripotent stem cell self-renewal, differentiation and DNA damage. *Human Molecular Genetics* doi:10.1093/hmg/ddq312. DOI:10.1093/hmg/ddq312
49. Gennes, P.-G. de, Brochard-Wyart, F. & Quéré, D. (Springer: 2004). *Capillarity and wetting phenomena: drops, bubbles, pearls, waves.*
50. Henson, R. (2005). *Flow Cytometry Data Reader and Visualization-MATLAB Script.* at <<http://www.mathworks.com/matlabcentral/fileexchange/8430-flow-cytometry-data-reader-and-visualization>>
51. R Development Core Team (R Foundation for Statistical Computing: Vienna, Austria, 2011). *R: A Language and Environment for Statistical Computing.* at <<http://www.R-project.org>>
52. Ripley, B. (2010). *CRAN - Package tree.* at <<http://cran.r-project.org/web/packages/tree/index.html>>

Chapter 4

Strategies for Implementing Hardware Assisted High-Throughput Image Analysis

The mechano phenotyping platform developed in the previous chapter enabled high-throughput mechanical measurements of cells via high-speed imaging. One of the major challenges of the system lie in the data processing burden due to the rate of data capture (>140,000 fps). In order to develop a robust platform applicable for general research and in clinical settings, new process efficient image analysis algorithms are needed. The analysis and development of these algorithms are explored here.

Imaging is ubiquitous in industrial processing, medicine, environmental science, and cell biology. Given the diverse modes of imaging that exist, an image can contain a wealth of information about an object. Process quality control in semiconductor manufacturing and particle synthesis uses a number of spatial metrics from images from scanning electron microscopy (SEM), transmission electron microscopy (TEM), atomic force microscopy (AFM), and optical microscopy^{1,2}. Imaging tools including positron emission tomography (PET), X-ray, magnetic resonance imaging (MRI) and computed tomography (CT) are widely used in medicine for diagnostic and prognostic purposes. Ocean and waterway monitoring, a critical charge of environmental science, can be performed with high-speed camera-coupled flow cytometry whereby the diversity and density of microscopic organisms, key indicators of ecosystem health, can be identified^{3,4}. In cell biology, for example, cell size, morphology, and location can be extracted from bright-field or phase-contrast images. And, the presence or location of biomolecules within cells can be obtained from fluorescence images of chemically labeled cells—which has recently been implemented with automated fluid handling and imagers for high

content analysis⁵. As technology improves, imaging rates and resolution increase and the cost of acquiring image sets decreases but this can burden the end user or associated analysis or sorting systems with large image backlogs. Ultimately, both extreme high-speed bright-field imaging and high-content analysis systems based on fluorescence imaging now have the propensity to generate truly massive image-based datasets and will require a method to accommodate the time-requirements of the user or system (e.g. real-time results will be required for cell sorting in medicine and cell biology). Only if automated image analysis can extract useful information and operate at meaningful rates will emerging image-based technologies find utility.

There are numerous applications where images have several advantages over other types of signal outputs and are often the preferred method of analysis. Qualitatively, images are most effective in conveying certain types of messages. They may also confer some measureable advantages. For example, flow cytometry measures scattered light to assess cell size and granularity, but these values are only relative⁶. Analysis of microscopic images, on the other hand, yields an exact value of size. Image analysis can also be used to distinguish between cells, debris, and clusters of cells where flow cytometry would yield erroneous results. Spectroscopic readings of biochemically labeled cells in microtiter plates lack the sensitivity to detect rare cell populations⁷ and can vary greatly with cell seeding density. In contrast, high-throughput automated microscopy coupled with automated image analysis can be used to identify and measure properties of single-cells with multiple spectra, high spatial and temporal resolution for measuring dynamic processes, and with high bit depth. This is a powerful tool for studying complex biological pathways or measuring heterogeneous response to stimuli. Further, new tools are being introduced to take images of cells in flow. High-speed CMOS cameras, with high frame rates, fast shutter speeds, and high sensitivities, have recently enabled novel studies of

highly dynamic events such as bubble rupture and microscale phenomena in particle-laden flow⁸⁻
¹¹. Other recent advances in computing, optics, and electronics have enabled imaging flow cytometry. This technology has shared roots in flow cytometry and microscopy, and can be applied to problems which would traditionally require multiple pieces of equipment and users trained in both. The ImageStream® system (Amnis Corporation, Seattle, WA) acquires multispectral/multimodal images at a rate of 1000 cells per second with sufficient resolution to extract features such as fluorescence intensity, morphology, and signal localization¹². It will be a useful tool for complex problems such as detecting tumor cells in body fluids and studying hematopoietic cells^{12,13}.

Cell morphology has been studied extensively and is a clinically useful biomarker for several diseases. In this paper, a high-throughput imaging cytometry system examines morphological features of cells. The dramatic morphological change that occurs following stimulation of granulocytes is one example where imaging cytometry will be useful (Fig. 1). The Amnis ImageStream system has been used to characterize morphological changes associated with the maturation processes of erythroid cells; traditional biomolecular labels were correlated with morphological changes in size, shape, texture, and nucleus to cytoplasm ratios¹³. Additionally, multispectral imaging flow cytometry has been used for the identification of morphological changes such as ruffle formations on HIV-1 infection T-cells¹⁴. In the clinic, cell blocks and smears are scrutinized for cells with shape and size characteristics that are indicative of infections and cancer. These examples illustrate the importance of image analysis of morphology. However, the current stage of morphological analysis relegates it to the role of cell classification, while biochemical biomarkers are used for critical applications in cell sorting. The ability to sort cells (requiring real-time measurement and analysis) would greatly enhance the

utility of morphology, and this ability will only be obtained by improvements to image analysis algorithms and processes.

However, these new technologies introduce challenges, especially in image processing and informatics¹⁵. Images can be very complex signals, with blurring occurring if an object's motion is faster than the shutter speed of the camera, and nonuniform illumination in wide field-of-view images. Filtering, measuring, tracking, and fitting data from, for example, 3D confocal images¹⁶ to complex multivariable models requires lengthy computation. Further, imaging flow cytometry and high speed microscopy can produce thousands of images per second. The qualities of these images (multispectral, high spatial and temporal resolution, and high bit depth) make the files tremendously large¹⁵ adding to computational requirements. In general, these technologies require offline image analysis. Gradually, increased computing power will increase image analysis speed and methods such as cloud computing image analysis¹⁷ will help share computing power with users on demand. But, for these technologies to be immediately accessible a new strategy which enhances the efficiency of image analysis algorithms is required.

Here we present a high-throughput image analysis strategy for a bright-field flow cytometry application with an image acquisition rate of over 140,000 frames per second. Analysis of bright-field images is in some respects more difficult than fluorescence images because of the more complex variation in intensities that are observed, such that our described strategies should also be compatible with fluorescence-based or other image sets. We first examine bottlenecks in the original detection and analysis algorithm, then design an alternative, less computationally demanding filtering algorithm, put in place a new detection strategy, and implement the algorithm on a graphical processing unit (GPU). Realization of real-time or near real-time analysis will enable systems like this one to be clinically relevant. The strategy which

we describe here should be considered for future implementations of high-speed image analysis in hardware.

Algorithm Description

Image enhancement and cell detection method

The automated analysis script was built in MATLAB v2009a (MathWorks, Natick, Massachusetts). The algorithm examines high-speed brightfield microscopic images (208 x 32 pixels x 142,857 frames/second) of cells in a high-throughput flow-through system. The algorithm (1) performs image adjustments, (2) detects the presence of an object, (3) tracks its motion, and (4) performs a measurement of morphology. The analysis is implemented frame-by-frame at a FOV of 23 x 20 pixels at an upstream location. The cell image signature is enhanced by bottom-hat filtering, which highlights intensity differences in a local area to allow for diameter measurement extractions. When a cell is detected in the first FOV the morphological analysis algorithm extracts morphological features. The same cell is then tracked downstream to examine changes in morphology. Analysis continues by moving the FOV downstream stepwise until the cell is within the FOV. Analysis continues until the cell is tracked out of the field. The FOV resets to the upstream location to detect the next cell.

Morphological analysis routine

Upon detection of a cell in the FOV, the image is interpolated and resized by 10x (230 x 200 pixels) to enhance the accuracy of centroid analysis and the extraction of morphological features of interest: area, diameter, and topography. The centroid method examines the bottom-hat filtered image using a 70 pixel disk (the expected average cell size) to locate the centroid

followed by a polar to Cartesian transformation. The cell walls are highlighted by locating the local maximums in pixel intensity (Fig. 2). Final data outputs are radius measurements at intervals of 4° per cell at each frame.

Hardware Acceleration

Recent work in hardware-assisted image analysis acceleration platforms have been implemented for various high-throughput applications¹⁸. In this section, first, we discuss acceleration platform modalities suited for high-throughput image analysis and their advantages and disadvantages. However, to fully utilize these hardware platforms for image analysis of cells or particles, the underlying algorithms for (1) image enhancement, (2) detection, (2) tracking, and (3) morphological analysis must be optimized for the specific platform. A systematic review of algorithm bottlenecks in the MATLAB-based CPU-run algorithms is first performed and algorithm components with the most intensive computing requirements are redesigned to optimize performance for GPU implementation. Finally, we compare the performance enhancements obtained with the GPU over the CPU algorithm.

Hardware-assisted image analysis acceleration platforms

Graphical processing units (GPUs) provide a high performance, low cost platform for hardware-assisted image analysis. GPUs employ a task parallel architecture that is primarily targeted towards accelerating graphics applications. However, they are being used more widely across other domains including databases¹⁹, weather forecasting²⁰ and cryptography²¹. They are also broadly utilized in digital image processing and the medical imaging field²²⁻²⁴. GPUs utilize a pipeline designed for efficient independent processing of data, and multiple pipelines are used

to exploit task level parallelism. GPUs outperform the CPUs by one to two orders of magnitude. They tend to perform well on highly parallel applications with limited number of memory accesses. Furthermore, they are ill-suited for applications with substantial amount of control flow, e.g., branching and looping. GPUs are programmed using custom languages and APIs; for example, the compute unified device architecture (CUDA) is an extension of the C programming language developed by NVIDIA for programming their GPUs. This and other GPU programming languages work using a stream model of computation where the application is divided into a set of parallel threads which explicitly defines parallelism and communication. Field-programmable gate arrays (FPGAs) are another option for hardware acceleration which is also used in a wide variety of applications. FPGAs use fine-grained programmable logic elements that implement basic Boolean logic functions (e.g., AND, OR, XOR). This creates the opportunity for substantial customization leading to significant performance increases over both CPUs and GPUs. As a concrete example, an FPGA implementation of the Viola-Jones object detection algorithm is about four times faster and uses an order of magnitude less power than the same algorithm running on a GPU²⁵. The high degree of customization afforded by FPGAs is both a blessing and a curse. It provides great flexibility in terms of the design of an application, yet it substantially increases the programming complexity. FPGA design tools require a significant amount of hardware design expertise. These design environments are a far cry from those used to program microcontrollers, microprocessors, digital signal processors and even GPUs. Therefore, the fundamental tradeoff when using an FPGA boils down to the need for high performance versus the ease of development.

In summary, FPGAs are typically the best option to create a high performance hardware accelerator. However, GPUs tend to be easier to program and more readily allow for

experimentation in parallelized algorithm design. Our initial analysis presented in the remainder of this article was done on GPUs due to reduced development complexity. The transition to FPGA implementation will build upon the work here emphasizing the design of novel efficient parallelization routines.

Bottleneck Analysis

To identify components of the algorithm that were most computationally intensive we used MATLAB v2009a and its profiler to obtain the run-times of three parts of the algorithm: image filter for image enhancement, morphological analysis, and other minor operations (detection and tracking). The run-time associated for each parts breaks down to 33.02%, 59.55%, and 7.42%, respectively. These results show that the image filter and morphological analysis constitute the majority of computing demands. Therefore, we focused on accelerating these two parts of the algorithms on the GPU platform.

These two computationally-intensive algorithms are naturally suitable for GPU parallelization since they call on high repetition of the same operations. For both image filter and morphological analysis, the algorithm can be divided into many identical operations (e.g., (1) local search operations that find minimum values; (2) repetition of simple transformation algebraic expressions). In a serial CPU program, these operations execute sequentially on the pixels. Since these operations execute the same computation on similar data types and without data dependency (e.g., one operation does not affect the others in a sequence), the image filter and morphological analysis algorithms can be implemented with GPUs very well and significant speedups can be expected.

Algorithm Modification

The architecture of GPUs and CPUs are significantly different in terms of thread scheduling²⁶ and on-chip memory²⁷. If the CUDA program has inefficient thread scheduling or memory access, GPU platforms will be no better than CPUs. This fact makes it necessary to modify algorithms for efficiency and minimal memory access before implementing it with GPUs.

In the image filter algorithm, the computing usage is dominated by image adjustment techniques. The main filtering algorithm is the bottom-hat filter which employs dilation and erosion operations. These two operations use a mask to search either for maximum or minimum values, respectively, in a local area of the image. The pixel corresponding to the center of the mask is replaced by the maximum or minimum value that is found in the local area²⁸. In the algorithm, the mask used is a disk area with an area of 16,357 pixels. This large size is required to ensure higher fidelity in the centroid analysis process. In the dilation and erosion operations, updating every pixel requires a maximum or minimum value search among all 16,357 elements at each pixel of the FOV. Resulting in over 46,000 calls per image (FOV: 230 x 200 pixels).

In the conventional dilation and erosion operations each mask area shares an overlapping region with the next mask. In order to minimize re-searching of these sections, we developed the “grid method” which organizes the image on to a grid system then re-uses the minimum or maximum search result of this common area by recording minima and maxima of each grid (Fig. 3). The pixels on the eroded or dilated image are then replaced by the corresponding value among the local minima or maxima in each grid. Further adjustments are possible by tuning the grid size to manage computing load for balancing resolution and efficiency. For a grid size of 40X40, the

minimum or maximum search operation for each image will be 16 elements instead of 16,357 elements.

In the morphological analysis algorithm the morphological features of the cell (e.g. diameters) are extracted to characterize the shape of the cell. The main operation of this algorithm is a centroid analysis of the cell to establish the origin for a polar to Cartesian coordinate transformation. The mapped image is then examined by a threshold analysis to outline cell walls and output the diameter at intervals of θ . In this original state, the algorithm is not suitable for GPU implementation for two reasons: (1) the centroid defined at each iteration is not located at the coordinate origin, thus creating scheduling inefficiencies for each GPU thread; and (2) the polar and Cartesian coordinate systems have different memory storage patterns which increase the memory access latency thus limiting run-time speedups (Fig. 4A).

To address these parallelization limitations, we made adjustments to both the centroid algorithm and data storage and access strategies. First, upon finding the centroid, the image is adjusted such that the centroid coordinate is also the origin of the polar coordinate (Fig. 5). Since the transformation from $(r, \theta) \rightarrow (x, y)$ are the same for all frames, the computation load for each GPU thread is predictable making it possible to assign threads efficiently in the GPU programming model. We next changed the memory storage and access strategy (Fig. 4B).

Instead of searching along all possible (r, θ) values, the new method accesses a $(r, \theta) \rightarrow (x, y)$ look-up-table (LUT) memory to find a corresponding pixel in the polar coordinate instead of algebraically converting the entire image into a Cartesian coordinate system. This strategy will result in quicker access times for mapping $(r, \theta) \rightarrow (x, y)$.

GPU Programming Model

The GPU program for the grid method bottom-hat filter consists of two modules: (1) erosion and (2) dilation. These two modules are very similar to each other erosion being a search for minimum values and dilation being a search for maximum values. Otherwise the GPU programming models are the same for both modules. Here we describe the GPU programming model for erosion.

The grid erosion algorithm consists of two phases: (1) finding a local minimum for each grid and (2) replacing the pixel on the erosion image with the minimum value among the local minimums of all grids inside or intersecting with the disk mask. The GPU grid erosion program model can parallelize these two phases using two kernels (Fig. 6). In the first kernel, we assigned a thread to each grid. The thread executes the local minimum value searching for the correspondent grid. In the second kernel, we assigned a thread to each pixel that is to be updated. The thread searches for the minimum value among the local minimums found in the first phase.

The morphological analysis GPU programming model utilizes a parallel threading scheme. Each thread is scheduled to operate at a defined θ , for the $(r,\theta) \rightarrow (x,y)$ transformation. Further parallelization can be achieved by a reduction GPU thread arrangement. However this method requires a uniform image size between sequential frames. The reduction method is not implementable for this version of the program, but in future revisions this process will aid in decreasing run-times. At this state we have kept the minimum gray-scale pixel searching as a serial process within each GPU thread (Fig. 4B).

Results

Image filter algorithm optimization using the grid erosion bottom-hat method results in distortion at the peripheries of the image (Fig. 7A). The interior of the image displays minimal differences against the conventional bottom-hat method (Fig. 7B). Error analysis of the grid erosion method highlights the top-left corner in the final bottom-hat image with higher error when comparing between the grid method and conventional method. This artifact is due in part to the grid erosion disk mask starting the grid analysis method at the upper left corner. These errors are compounded with the dilation operation to produce the high local error in final filter output. The final total error of the top left region is approximately 30% difference compared to the conventional method. Additionally, by using the grid method, high local intensity variations are completely smoothed out. These errors are not expected to interfere significantly with final morphological output as morphological analysis routine utilizes maxima threshold rules to extract diameter measurements. However, one can decrease the filtering error by adjusting to a smaller grid size.

Lastly, we compared the optimized image filter and morphological algorithm for GPU processing to the native CPU code. The testing was done on a 64-bit Intel Core i7 1.60GHz machine with 6GB RAM and Nvidia GT230M GPU. Our first benchmark compared the conventional bottom-hat filter against the grid method. The grid method bottom-hat filter algorithm resulted in a 2.15X speedup against the baseline algorithm (Fig. 8). When this is implemented on GPU hardware, we see a total decrease of 8.54x speedup.

The morphological analysis algorithm when modified with the transformation LUT also decreased the run-time dramatically. When compared to the original method without coordinate correction and the use of the transformation LUT, there is a 2.88x decrease in run-time on a

CPU, and when implemented on GPU there is a 55.64x decrease in run-time. As discussed in the previous section, we can expect further decreases in run-time as we adjust the degree of batch image processes. Determining the optimal batch rate is an on-going investigation.

Conclusion

In our approach to hardware-assisted high-throughput image analysis, we have shown that through improvements to algorithm design, execution of data management shortcuts, and optimization of image filters for implementation in parallelization schemes, the computational requirements for image analysis routines can be diminished dramatically. To date, the combination of improvements to the cell morphology analysis algorithm and the initial implementation of the GPU have resulted in a combined 20.30x run-time improvement. However, to achieve real-time analysis capabilities work remains to further improve the algorithms and eventually transition from a GPU to an FPGA, which often imparts an additional speedup which will ultimately be necessary to elicit wider adoption of biomedical technologies which require computationally demanding image analysis.

Figures

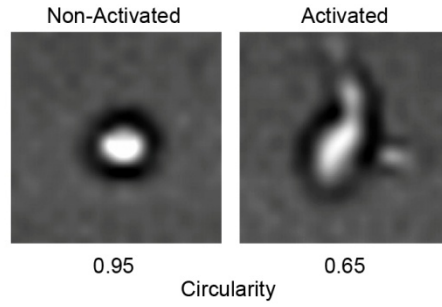


Figure 1. An example of cellular morphology differences due to cell states. High-speed microscopic images of a granulocyte (left) and a granulocyte activated by a chemical treatment (right) with associated measure of circularity as a characterization of the morphological differences of each cell.

Automated Cell Tracking and Analysis

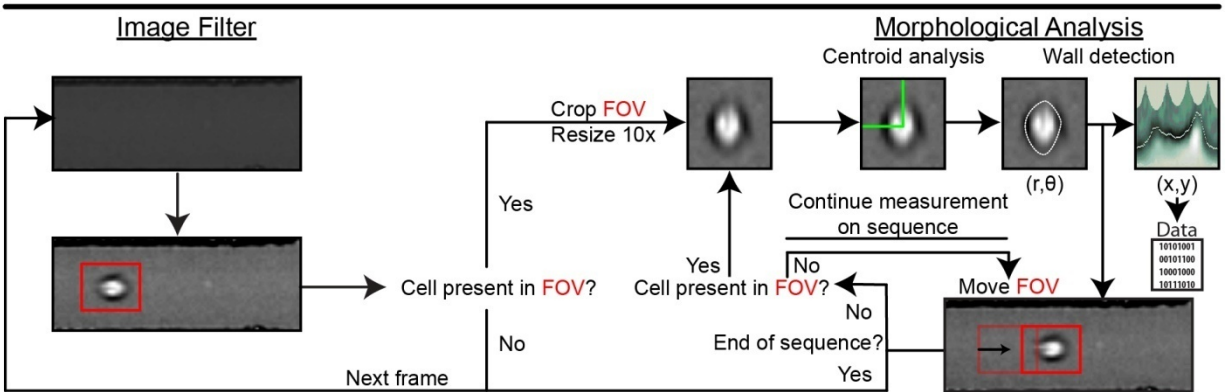


Figure 2. Automated cell tracking and analysis algorithm framework. The raw video frame is first contrast enhanced by the image filter algorithm, and the cell detection algorithm examines the field-of-view (FOV) (in red) for presence of a cell. When a cell is located in the FOV, the frame is cropped and resized by 10x. The morphological analysis algorithm starts by performing centroid analysis to determine origin of the polar to Cartesian coordinate transformation. The diameters are then extracted from the mapped image. The analysis is then iterated on the remaining cell image series until the FOV tracks out of frame.

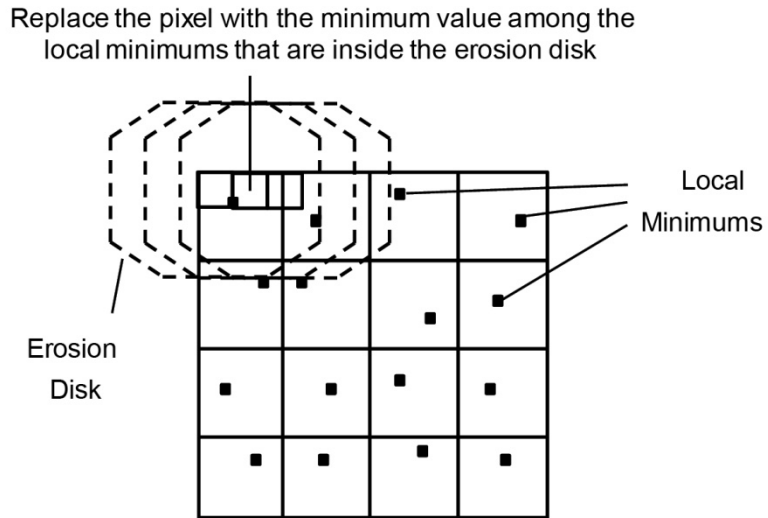


Figure 3. The grid method filter algorithm. The image is divided into several grids and each grid is analyzed for the local minimums or maximums (dots). For each pixel of the erosion or dilated image, the pixel value is determined by searching the grid for local minimums and maximums, respectively, within the disk mask.

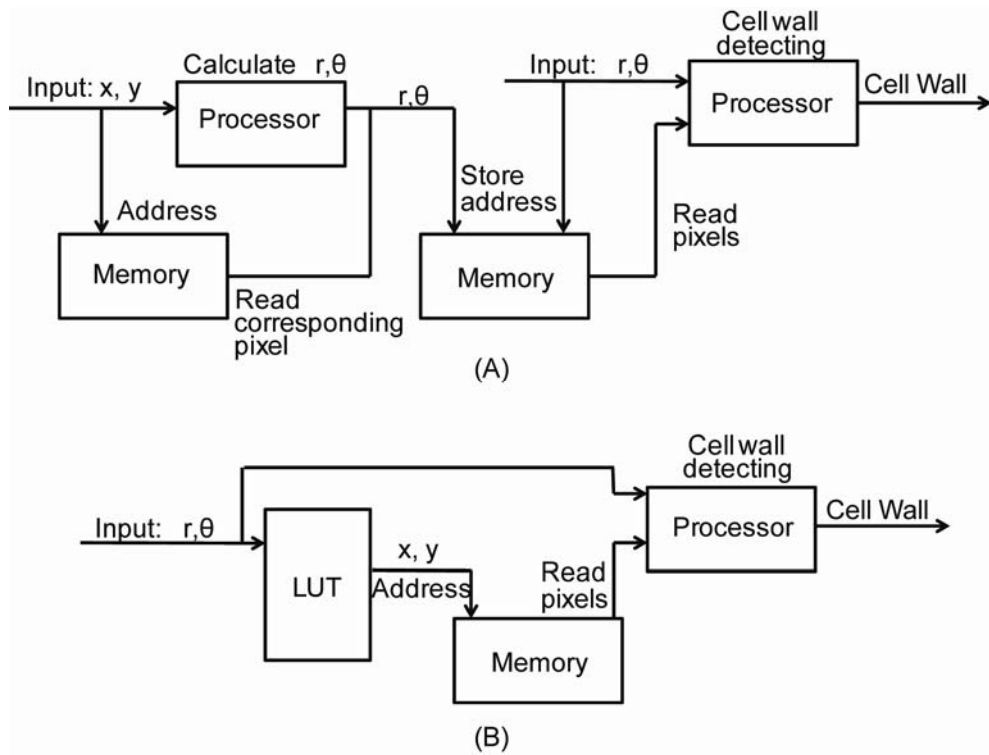


Figure 4. (A) Original morphological analysis algorithm. (B) Modified morphological analysis algorithm where a LUT lowers computation demands for the $(r, \theta) \rightarrow (x, y)$ transformation. Additionally, memory access is reduced as the polar coordinate image is not used.

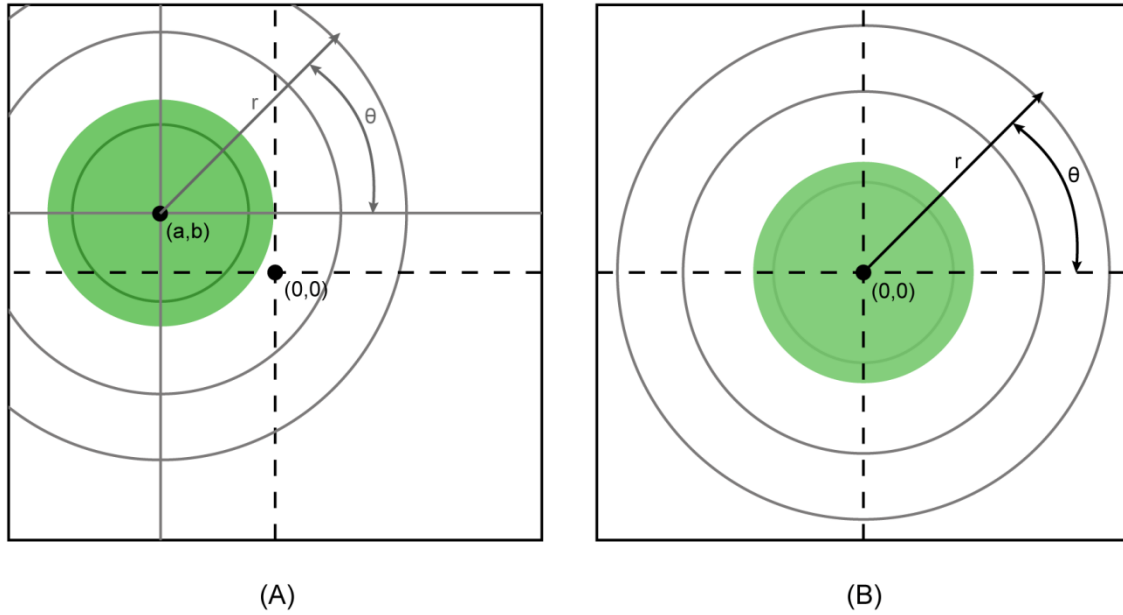


Figure 5. Re-centering FOV prior to coordinate transformation. (A) In the original algorithm, the cell center is not at the coordinate origin, thus requiring computing time to map each unique coordinate for the polar to Cartesian transformation from the (a,b) origin. (B) When a re-cropping event for a new FOV based on the centroid location, this enables the use of the $(r, \theta) \rightarrow (x, y)$ transformation look-up-tables per mapping event.

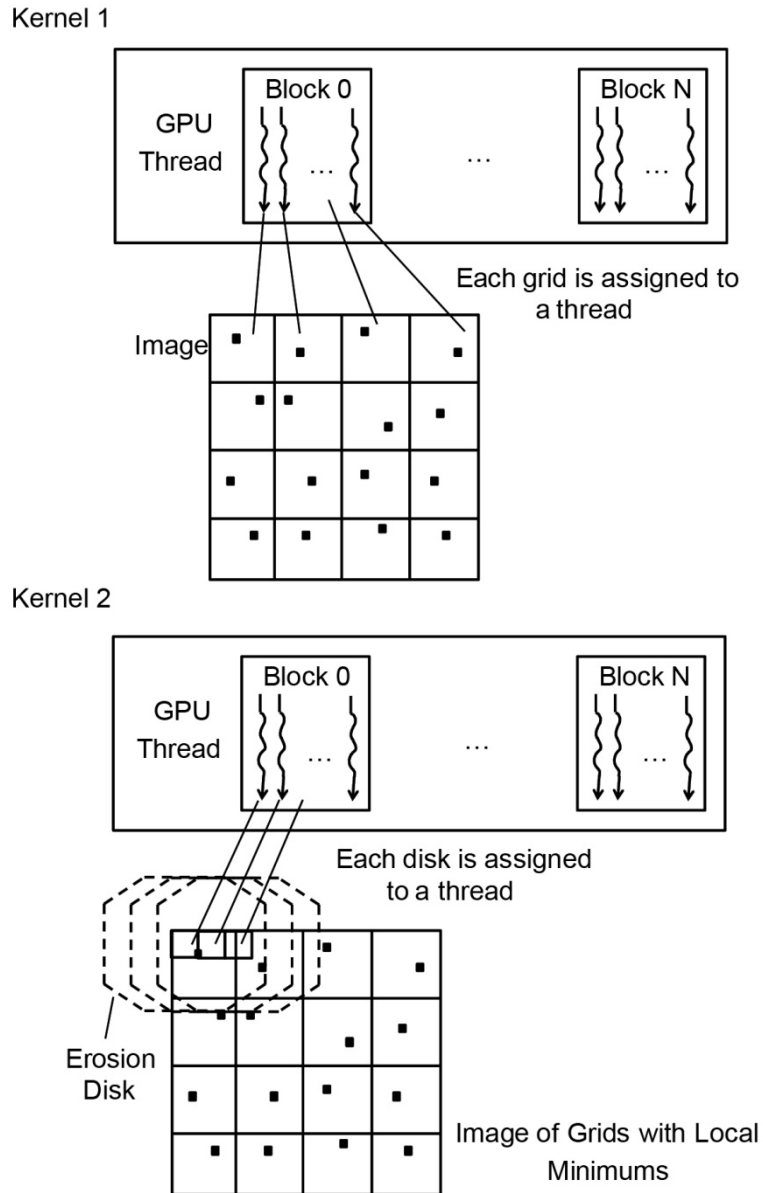
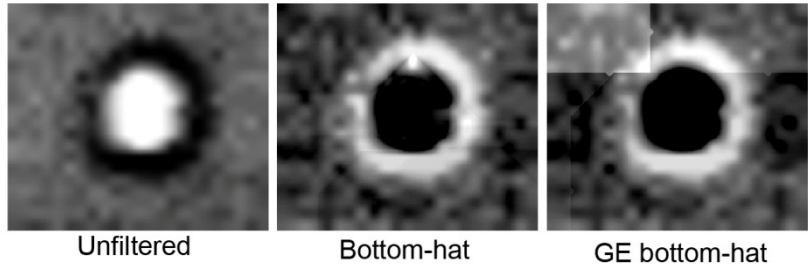


Figure 6. GPU programming model for grid erosion algorithm. In kernel 1, the local minimum (dots) search operations are executed in parallel by assigning each grid to a thread. In kernel 2, the eroded pixel value is found in parallel by assigning each disk to a thread.

A) Gray Scale Images Before and After Bottom-Hat Filter



B) Grid Erosion Bottom Hat Filter Error Analysis

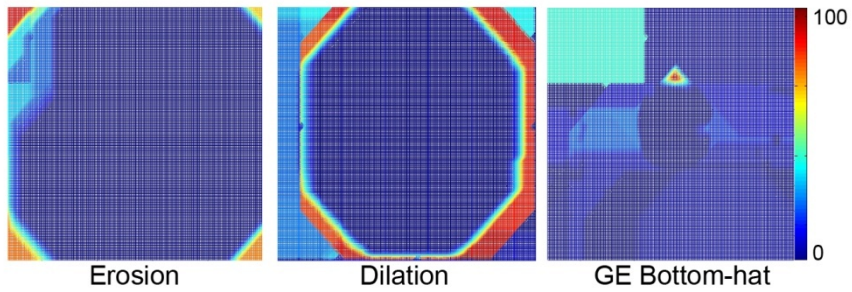


Figure 7. Results of bottom-hat filter using the grid erosion method. (A) Visual comparison of the gray scale images of original bottom-hat filtered image (middle) versus the grid erosion method bottom-hat filtered image (right). (B) Error analysis of the grid erosion bottom-hat filter method against the naïve bottom-hat filter method illustrating that the highest errors are along the edges of the image, while interior pixels values are conserved.

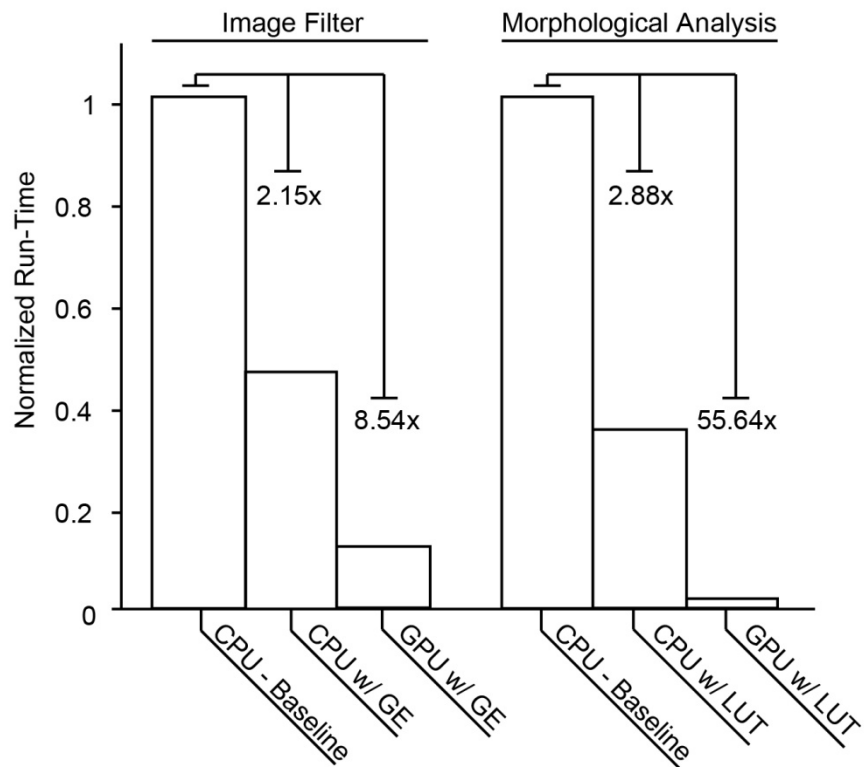


Figure 8. Run-time improvements against baseline algorithm. The grid erosion (GE) routine for the bottom-hat filter method achieves a 2.15x run-time improvement on a CPU, and an 8.54x run-time improvement when implemented on a GPU. The coordinate transformation look-up-table (LUT) routine achieves a 2.88x run-time improvement on a CPU, and a 55.64x run-time improvement when implemented on a GPU.

Bibliography

1. Witt, W., Kohler, U. & List, J. (2004). Direct imaging of very fast particles opens the application of the powerful (dry) dispersino for size and shape characterization. *Sympatech GmbH*
2. Provder, T. (1997). Challenges in particle size distribution measurement past, present and for the 21st century. *Progress in Organic Coatings* 32:143–153. DOI:10.1016/S0300-9440(97)00043-X
3. Culverhouse, P. F., Williams, R., Benfield, M., Flood, P. R., Sell, A. F., Mazzocchi, M. G., Buttino, I. & Sieracki, M. (2006). Automatic image analysis of plankton: future perspectives. *Mar Ecol Prog Ser* 312:297–309. DOI:10.3354/meps312297
4. Sieracki, C. K., Sieracki, M. E. & Yentsch, C. S. (1998). An imaging-in-flow system for automated analysis of marine microplankton. *Mar Ecol Prog Ser* 168:285–296. DOI:10.3354/meps168285
5. Starkuviene, V., Liebel, U., Simpson, J. C., Erfle, H., Poustka, A., Wiemann, S. & Pepperkok, R. (2004). High-Content Screening Microscopy Identifies Novel Proteins With a Putative Role in Secretory Membrane Traffic. *Genome Research* 14:1948–1956. DOI:10.1101/gr.2658304
6. Shapiro, H. M. (Wiley-Liss: New York, 2003). *Practical Flow Cytometry*.
7. Di Carlo, D. & Lee, L. P. (2006). Dynamic Single-Cell Analysis for Quantitative Biology. *Analytical Chemistry* 78:7918–7925. DOI:10.1021/ac069490p
8. Di Carlo, D., Irimia, D., Tompkins, R. G. & Toner, M. (2007). Continuous inertial focusing, ordering, and separation of particles in microchannels. *Proceedings of the National Academy of Sciences* 104:18892–18897. DOI:10.1073/pnas.0704958104
9. Gossett, D. R. & Di Carlo, D. (2009). Particle Focusing Mechanisms in Curving Confined Flows. *Analytical Chemistry* 81:8459–8465. DOI:10.1021/ac901306y
10. Hur, S. C., Tse, H. T. K. & Di Carlo, D. (2010). Sheathless inertial cell ordering for extreme throughput flow cytometry. *Lab Chip* 10:274. DOI:10.1039/b919495a
11. Bird, J. C., de Ruitter, R., Courbin, L. & Stone, H. A. (2010). Daughter bubble cascades produced by folding of ruptured thin films. *Nature* 465:759–762. DOI:10.1038/nature09069

12. Basiji, D. A., Ortyn, W. E., Liang, L., Venkatachalam, V. & Morrissey, P. (2007). Cellular Image Analysis and Imaging by Flow Cytometry. *Clinics in Laboratory Medicine* 27:653–670. DOI:10.1016/j.cll.2007.05.008
13. McGrath, K. E., Bushnell, T. P. & Palis, J. (2008). Multispectral imaging of hematopoietic cells: where flow meets morphology. *J. Immunol. Methods* 336:91–97. DOI:10.1016/j.jim.2008.04.012
14. Nobile, C. *et al.* (2010). HIV-1 Nef inhibits ruffles, induces filopodia, and modulates migration of infected lymphocytes. *J. Virol* 84:2282–2293. DOI:10.1128/JVI.02230-09
15. Pepperkok, R. & Ellenberg, J. (2006). High-throughput fluorescence microscopy for systems biology. *Nat Rev Mol Cell Biol* 7:690–696. DOI:10.1038/nrm1979
16. Lin, G., Bjornsson, C. S., Smith, K. L., Abdul-Karim, M.-A., Turner, J. N., Shain, W. & Roysam, B. (2005). Automated image analysis methods for 3-D quantification of the neurovascular unit from multichannel confocal microscope images. *Cytometry A* 66:9–23. DOI:10.1002/cyto.a.20149
17. Simagis Live Technology Use Cases - Simagis Live. at <<http://live.simagis.com/cases>>
18. Owens, J. D., Luebke, D., Govindaraju, N., Harris, M., Krüger, J., Lefohn, A. E. & Purcell, T. J. (2007). A Survey of General-Purpose Computation on Graphics Hardware. *Computer Graphics Forum* 26:80–113. DOI:10.1111/j.1467-8659.2007.01012.x
19. Govindaraju, N. K., Lloyd, B., Wang, W., Lin, M. & Manocha, D. (2004). Fast computation of database operations using graphics processors. *Proceedings of the 2004 ACM SIGMOD international conference on Management of data* 215–226doi:10.1145/1007568.1007594. DOI:10.1145/1007568.1007594
20. Michalakes, J. & Vachharajani, M. (2008). GPU acceleration of numerical weather prediction. *Parallel and Distributed Processing, 2008. IPDPS 2008. IEEE International Symposium on* 1–7doi:10.1109/IPDPS.2008.4536351. DOI:10.1109/IPDPS.2008.4536351
21. Manavski, S. A. (2007). CUDA Compatible GPU as an Efficient Hardware Accelerator for AES Cryptography. *Signal Processing and Communications, 2007. ICSPC 2007. IEEE International Conference on* 65–68doi:10.1109/ICSPC.2007.4728256. DOI:10.1109/ICSPC.2007.4728256

22. Stone, S. S., Haldar, J. P., Tsao, S. C., Hwu, W. -m. W., Sutton, B. P. & Liang, Z.-P. (2008). Accelerating advanced MRI reconstructions on GPUs. *Journal of Parallel and Distributed Computing* 68:1307–1318. DOI:10.1016/j.jpdc.2008.05.013
23. Fung, J. & Mann, S. (2008). Using graphics devices in reverse: GPU-based Image Processing and Computer Vision. *Multimedia and Expo, 2008 IEEE International Conference on* 9–12doi:10.1109/ICME.2008.4607358. DOI:10.1109/ICME.2008.4607358
24. Mueller, K. & Fang Xu (2006). Practical considerations for GPU-accelerated CT. *Biomedical Imaging: Nano to Macro, 2006. 3rd IEEE International Symposium on* 1184–1187doi:10.1109/ISBI.2006.1625135. DOI:10.1109/ISBI.2006.1625135
25. Hefenbrock, D., Oberg, J., Nhat Thanh, Kastner, R. & Baden, S. B. (2010). Accelerating Viola-Jones Face Detection to FPGA-Level Using GPUs. *Field-Programmable Custom Computing Machines (FCCM), 2010 18th IEEE Annual International Symposium on* 11–18doi:10.1109/FCCM.2010.12. DOI:10.1109/FCCM.2010.12
26. Ryoo, S., Rodrigues, C. I., Bagsorkhi, S. S., Stone, S. S., Kirk, D. B. & Hwu, W. W. (2008). Optimization principles and application performance evaluation of a multithreaded GPU using CUDA. *Proceedings of the 13th ACM SIGPLAN Symposium on Principles and practice of parallel programming* 73–82doi:10.1145/1345206.1345220. DOI:10.1145/1345206.1345220
27. Ryoo, S., Rodrigues, C. I., Stone, S. S., Bagsorkhi, S. S., Ueng, S.-Z., Stratton, J. A. & Hwu, W. W. (2008). Program optimization space pruning for a multithreaded gpu. *Proceedings of the 6th annual IEEE/ACM international symposium on Code generation and optimization* 195–204doi:10.1145/1356058.1356084. DOI:10.1145/1356058.1356084
28. Sonka, M., Hlavac, V. & Boyle, R. (Thompson Learning: 2008). *Image processing, analysis, and machine vision*.

Chapter 5

Mechano Phenotyping for the Diagnosis of Malignant Pleural Effusions

The utility of mechanical biomarkers for cancer diagnostics was briefly explored in Chapter 3 with promising results. Now coupled with increased robustness attributed to the improvements in data processing (chapter 4), the work here extends the deformability cytometry platform for the application of diagnosing malignant pleural effusions.

Pleural effusions are valuable sources of diagnostic information. In a healthy individual the amount of pleural fluid (PF) is between 7 and 16 mL of acellular liquid, however systemic imbalances and disease may lead to an abnormal accumulation fluid containing disseminated cells (up to 2L).^{1,2} As such pleural fluid samples can provide insight into patient health such as the status of infections, inflammatory processes, and malignant diseases. The process of thoracentesis, the procedure of removing pleural effusions, is performed to relieve patient discomfort in the chest cavity and to provide clinicians a fluid biopsy to determine etiology.

The examination of pleural effusions for malignancies in clinical settings relies on cytological analysis as the gold standard. The cytopathologist examines cells from cell smears and cell blocks and identifies features of cytoplasmic and nuclear morphology suggestive of malignancy. Clinical outcomes in diagnosis of malignant pleural effusions include: negative for malignant cells (NFMC), acute inflammation (AI), chronic/mixed inflammation (CMI), and malignant pleural fluid (MPF). Pathological analysis of each specimen spans minutes to tens of minutes depending on the complexity of the biological sample. Difficulties in morphological identification include “biological noise” arising from similar morphology of reactive mesothelial cells (cells derived from the mesothelium membrane) and a high density of leukocyte

populations, which both can mask possible epithelial or hematopoietic malignancies^{3,4}. As such, the sensitivity for malignant pleural effusions spans a wide range between 40-90%.⁵ This variability is due to: 1) the source of the malignancy (e.g., mesotheliomas: 4-77% sensitivity)⁶⁻⁸, 2) paramalignancies where the volume of the sample analyzed on cell smears or blocks is unable to capture rare malignant subpopulations within the field-of-view, 3) specimen quality (cellularity) and number of specimens, and 4) experience of the cytopathologist.^{4,5} Due to these difficulties, conclusive diagnosis of pleural effusions often requires follow-up molecular-label-assisted-techniques such as biochemical surface markers characteristic of disease phenotype using flow cytometry⁹⁻¹¹ and immunohistochemistry^{12,13}, disease specific genetic signatures by fluorescence in situ hybridization (FISH)^{12,14}, as well as additional invasive follow-up biopsies to confer findings. However, even with these drawbacks, cytological analysis of pleural fluids is an attractive technique when considering the level of sensitivity and specificity relative to degree of time investment.

Sample preparation of pleural effusions for cytological analysis involves numerous processing steps, staining reagents, pre-screening reads by cytotechnicians prior to the cytopathologist reading. Even while many of these protocols are now automated, sample preparation can take on the order of 1-2 hours in batch and still require some manual steps. The majority of pleural effusion samples are identified to be negative for malignancies (>80%). Thus a simple, quick, and automated pre-screening tool to identify high-risk patients would be greatly beneficial to maximize the use of available resources, reduce sample processing burdens, and decrease the time to final diagnosis for treatment intervention.

To achieve this benefit an approach with reduced labeling and sample preparation requirements would be ideal, avoiding time and cost associated with repeated solution exchange

operations and reduced need for follow-up reagents for conventional molecular biomarkers and stains. Label-free biomarkers, such as the mechanical properties of single cells or the mechanophenotype, have shown promise in clinical diagnostics. Label-free mechanophenotyping has shown that the mechanical properties of cancer cell lines drastically differ from their benign counterparts in a laboratory setting. While it has long been known that tumors are stiffer than neighboring healthy tissue^{15,16}, it has recently been reported that individual cancer cells are softer, and this deformability may confer their ability to migrate through tissue. Several methods have been developed or adapted to probe mechanical properties of cells: atomic force microscopy (AFM)^{15,17,18}, micropipette aspiration^{19,20}, cell transit analysis^{21–25}, microfluidic optical stretching^{16,26}, and hydrodynamic forces²⁷. Yet prior technology was limited to small clinical studies of a few cells from a few patients due to the technological complexity. One group has previously analyzed biophysical signatures of cells in PF. AFM analysis of malignant cells isolated from malignant pleural fluids demonstrated that these subpopulations are mechanically softer than the native cells.¹⁵ However, the technological complexity requiring user intervention to select morphologically malignant cells limits the systems throughput. Yet this initial work showing differences indeed exists in subpopulations of clinically relevant biological samples, gives this work precedent to further the applicability of biophysical markers as a diagnostic marker.

In this study, we evaluate a technique previously developed and validated by our group – Deformability Cytometry (DC)²⁸ – to measure mechanical properties of single cells in a high-throughput manner (>1,000 cells/sec) towards the diagnoses of malignant pleural effusions (Fig. 1). Briefly, the cells are accelerated upwards of 3 m/s, then rapidly decelerated by an opposing wall of fluid which causes the velocity of the cell to approach 0 m/s over a 200 μm distance with

a period of 100 μ s. In this process the cells are subjected to fluid stress forces upwards of 1 μ N. Using the quantitative metrics of cell deformability (D - maximum ratio of major over minor axis over the whole deformation series) and initial size, 2D scatter plots are generated for analysis. Additionally, as this technique screens cells at throughputs comparable to flow cytometry, this high-throughput capacity enables quantitative population analysis of the biophysical characteristics. Analysis of subpopulation characteristics can then be correlated to the cytological diagnosis and final clinical outcome. DC is able to confer high correlation to cytology outcomes of negative for malignant cells (NFMC), acute inflammation (AI), chronic/mixed inflammation (CMI), and malignant pleural fluids (MPF). This platform is similar in operation and analysis to conventional flow cytometry, but without the extensive sample preparation steps - each sample yielding high density quantitative profiles is processed within 5 minutes. In this study of 119 patients, averaging over 3,000 single-cell measurements per patient, DC provides the advantages of both high cell counts per patient and large patient samples for confidence in sampling heterogeneous populations, and confidence in establishing common outcome profiles, respectively. The sensitivity and specificity of DC is promising as a label-free method used in a pre-screening role. As a complementary method to slide-based cytology and follow-up techniques, DC has the capabilities to dramatically increase diagnostic accuracy and decrease healthcare costs.

Results and Discussion

Distinct deformability cytometry profiles correlated with separate clinical outcomes

During cytological analysis of pleural effusions the cytopathologist analyzes slides prepared with cells from the effusions and notes morphological features including nuclear-to-cytoplasmic ratio, nuclear shape, nucleation level, the density of nuclei (chromatin irregularity), the density of cytoplasm, cell-cell junctions, the shape of cytoplasmic and nuclear membranes, granules, cell cycle states (e.g., mitosis), cell size distribution, clustering of cells, and concentration of cells. With this information, the cytopathologist identifies cell subpopulations which are representative of disease states. Previously we have observed biomechanical changes *in vitro* models of diseases typically manifesting in pleural fluids and thus expected to find correlations in clinical samples. We performed DC and cytological analysis on 119 patient samples. In order to correlate the two analysis methods we engaged in both bottom-up – isolating predominant subpopulations indicative of disease states and measuring them alone – and top-down approaches – grouping DC datasets by cytological diagnosis and searching for similarities.

In samples designated as negative for malignant cells (NFMC) – without confounding inflammatory diseases – by cytology, the cellular composition is predominately made up of non-activated inflammatory cells and benign mesothelial cells. Comparative analysis of these samples by DC displays the major feature of a high density population with small size ($<12\ \mu\text{m}$), rigid deformability ($D < 1.4$), and with a minimal scattering in both size and deformability.

Characteristic DC profiles of NFMC patients – patients 1-5 – are shown in Fig. 2. The median deformability of this main leukocyte population is 1.32 (n=21). To confirm this population as leukocytes, isolated healthy donor leukocytes from peripheral blood were also measured and were found to have be predominantly small and rigid (Fig 2b). Another feature of PF samples is

a large sized mesothelial subpopulation with a low deformability measure. For example in patient #4 the DC profile shows a significant population between 15 – 20 μm with a deformability <1.4 . This population was confirmed by cytology findings to correspond to benign or reactive mesothelial cells. This feature appears in specimens with the reactive mesothelial (RM) cytology outcome.

In cases of infections, tissue inflammation (due to cirrhosis, kidney failure, heart failure), or leukemia, the PF is populated by increased numbers of leukocytes. Analysis for malignancy in cases where inflammation is also present are difficult by cell smears or cell blocks as dense leukocyte populations can obscure malignant cells of interest. Additionally, a high density of leukocytes indicates a possibility for leukemia. However, morphological analysis of leukemia cells is difficult, with sensitivities between 30-50%^{29,30}, and relies heavily on flow cytometry as a follow-up procedure. Activated leukocytes in these samples pose a significant diagnostic management challenge.

Notably, leukocytes are shown to undergo drastic architectural changes in response to activation, with corresponding changes in mechanical properties.^{31,32} Activated neutrophils and lymphocytes undergo structural chromatin reorganization and decondensation potentially important for up-regulation of activation response pathways. The associated mechanical changes are also found in the mechanophenotype we measure. Deformability cytometry profiles for acute inflammation (AI) and chronic/mixed inflammation (CMI) samples both differ from NFMC profiles. Acute inflammation is a response to infections characterized by activation of the neutrophil population. Activated neutrophils are known to have cytoplasmic and nuclear shape changes resulting in globular nuclei and increased formation of lamellipodia which make it difficult to identify malignancies by conventional cell smears and cell blocks alone as features

mimics malignant phenotypes (Fig. 3B), thus requiring specific immuno-labels for confirming diagnoses. However, deformability cytometry analysis of these cases reveal a distinct profile that possesses a small (<12 μm) population with an increased subpopulation of highly deformable cells with mean proportion of cells above deformability of 1.6 to be 16.6%, which is ~12x higher when compared to NFMC outcomes (1.4%). The median deformability of AI specimens is 1.56 (n=30). Characteristic DC profiles of AI patients – patients 6-10 – are shown in Fig. 3. This change from rigid non-activated leukocytes agrees with *in vitro* observations as neutrophils are activated by short incubation with tetradecanoyl-Phorbol-13-acetate (TPA) (Fig. 3C).

In CMI cases, mononuclear cells such as lymphocytes and macrophages can be the main cellular constituent of samples. An increase in size is a key indicator of lymphocyte activation. Additionally, activated cells have globular nuclei and undergo morphological changes such as increases in size. However, similar to AI cases, conventional cell smears and cell blocks have difficulty ruling out malignancy due to the CMI background (Fig. 4B) and frequently require follow-up procedures to confirm diagnoses. In DC profiles, CMI cases are observed to have a slightly larger size spanning 8 – 15 μm and a large distribution of deformability (D: 1.0 – 3.0). Pooling all CMI samples, the mean proportion of cell less than 12 μm and above a deformability of 1.6 is 24.7%, comparatively to NFMC and AI this is an 18x and 1.5x increase in region density, respectively. The median deformability in CMI specimens is 2.0 (n=39). Characteristic DC profiles of CMI patients – patients 11-15 – are shown in Fig. 4. *In vitro* activation of peripheral blood mononuclear cells by phytohemagglutinin (PHA) reveals profile features similar to those of samples with a CMI outcome (Fig. 4C).

Deformability cytometry profile features accurately identify malignant pleural fluids

Malignant pleural fluid (MPF) typically contain a subpopulation of cells residing in the large ($>17 \mu\text{m}$) and highly deformable ($D>1.4$) upper right quadrant (Fig. 5). However, MPF cases are also diverse compared to NFMC, AI, and CMI cases. This may be due to the wide range of origins of malignancy that accumulate in the PF. The 17 MPF cases include breast adenocarcinoma (N=1), ovarian adenocarcinoma (N=3), mesothelioma (N=1), soft tissue sarcoma (N=1), pancreatic adenocarcinoma (N=1), non-small cell lung carcinoma (N=1), gastrointestinal carcinoma (N=7), lymphoma (N=1), and unknown origin (N=1). Interestingly, in a majority of these cases DC profiles indicated features of AI or CMI concurrently with an increased percentage of large and deformable cells, which are seldom noted in cytology diagnoses.

Algorithmic diagnosis using characteristic profile features

Using pooled DC profiles associated with each clinical outcome, unknown patient samples can be algorithmically analyzed and a DC-based diagnosis given based on unique statistically significant features. The quantification of cells within the large ($>17 \mu\text{m}$) and deformable ($D: >1.4$) quadrant across MPF samples spans 3% – 31% with a mean of 23%. In NFMC samples the analysis of the same quadrant spans 0% - 26% with a mean of 2%. Using this quadrant analysis alone, DC can achieve a sensitivity of 88% and a specificity of 71% by a simple gating threshold established by using the upper 95% confidence limit for the mean proportion of NFMC samples in this upper right region (6%) (Fig. 6A). To further increase the sensitivity of the assay, we examined the similarity of profile features to standard profiles of NFMC, AI, and CMI. Standard curves for each of the pooled outcomes are created by binning

size, and deformability at the cumulative sum threshold of the top 90% of bins describing the dataset then taking the median (Fig. 6B). Calculating the root mean squared error (RMSE) of individual profiles against each standard profile gives a metric of similarity to the non-malignant profile types. These metrics can also be used to further stratify cases for inflammatory profiles of acute or chronic/mixed inflammation. The detailed algorithm is described in the supplementary information. While DC could be implemented in the clinical workflow in various manners, diagnostic methods which possess high sensitivity can have a profound effect on efficiency. We propose two operational modes: high sensitivity – DC-A – mode and high specificity – DC-B – mode. Tuned for high sensitivity – DC-A – with a sensitivity of 100% and specificity of 69%. Alternatively, the decision analysis algorithm tuned for high specificity – DC-B – can be weighted to achieve 100% specificity and 35% specificity (Fig. 6C). These two operational modes confer an area under the curve (AUC) of 0.91. This capability is only possible since DC provides objective quantitative analysis of each sample. This performance can assist cytology in reducing follow-up procedures. Without DC 89% of MPFs required follow-up (flow cytometry, immunohistochemistry, or additional biopsies) and 38% of samples with outcomes that were NFMC required follow-up (Fig. 6D).

Implementing DC as an adjunct to cytology analysis will reduce cytology and follow-up workload. Using the DC-A criterion, which has a high negative predictive value (1.00) in a pre-screening role, this would identify 58 samples as true NFMC (69%) without needing to undergo cytology analysis. Additionally, this eliminates 21 follow-up procedures (44%) that would have been ordered following cytology alone. The remaining 43 cases would require cytology because of the lower positive predictive value (0.40). Following cytology-based stratification of conclusive cases and cases requiring follow-up analysis, DC decision analysis can further reduce

the workload of follow-up orders by cytology using the DC-B algorithm for high specificity. The DC-B method screens out MPF cases as this method has a high positive predictive value (1.00) (Fig. 6E). Employing both analysis methods (DC-A, and DC-B) adjunct to cytology for the cases we have already studied, would ultimately reduce reduces the workload of samples handled and samples requiring follow-up analysis by 56% (Fig 6F).

We also investigated the performance of using the size parameter independently for diagnosis (S. Fig 1). Setting the size threshold of 17 μm and using the 95% upper CI limit of the mean proportion (14%), this method achieves a sensitivity of 65% and specificity of 87%. This result suggests that differential size counts alone have some diagnostic value, but complementing this metric with the deformability parameter increases diagnostic accuracy.

Case study: atypical cell diagnoses

The ability of deformability cytometry to adjust to a high sensitivity mode can aid in cytological analysis is particularly apparent in correctly identifying ambiguous samples with “atypical cells” (AC) that always require follow-up. In such cases, DC diagnosis of MPF or NFMC can reduce the number of cases requesting follow-up procedures. Difficulties in cytology for diagnosis of these cases are due to difficult to interpret cellular morphology compounded with patient's history of prior malignancies or pre-malignancies. Follow-up procedures including flow cytometry, immunohistochemistry, and further biopsies are always ordered for samples receiving this diagnosis. Of the initial AC diagnoses, the DC-A decision analysis was able to conclusively diagnose 70% (X of Y) of AC cases correctly as MPF or NFMC when compared to the final clinical outcome (Fig. 7). AC cases with large and highly deformable cells and with minimal profile similarities to pooled cases were identified to be MPF matching final outcome

diagnoses with 100% sensitivity (Fig. 7, pt. 1-4). In NFMC cases, AC profiles with a small and rigid subpopulation were correlated to the negative outcome with 50% specificity (Fig. 7, pt. 5-10). AC cases with chronic inflammation features were also quantitatively identified in patient samples (Fig. 7, pt. 7, 9, 10). Benefits of correctly identifying these inconclusive samples can be realized by earlier disease treatment and management, as well as reduced costs associated with follow-up procedures as discussed in Figure 6.

Case study: differing diagnoses for patients with concurrent disease

PF samples from 18 patients with known concurrent malignancies or tumors were considered separately from the main analysis set. These cases all received a NFMC score by cytology and cytology follow-up, however when assayed by DC the profile features are found to have enough variability from standard outcome profiles that the DC-A decision analysis algorithm categorized 15 of 18 cases as MPF. Profiles feature irregularities and instances of large and highly deformable cells (Fig. 8). Samples from patients with concurrent diseases, including leukemias (Fig. 8 pt. 1-4, 8), mesothelioma (Fig. 8 pt. 7), small cell carcinomas (Fig. 8 pt. 5), and adenocarcinomas (Fig. 8 pt. 6, 9, 10), were assayed. The majority of these samples also underwent additional follow-up procedures to verify cytology findings, including flow cytometry and immunohistochemistry. However, even with follow-up procedures cytology did not identify cells consistent with the concurrent disease. The appearance of malignant DC profiles in these patients with concurrent disease is suggestive of the ability of DC to identify malignant cell populations not easily identified by cytology and standard immunolabeling-based follow-up.

Case study: mesothelioma

The low sensitivity of cytology (40%) to mesotheliomas is due to limited morphological differences between malignant and benign mesothelial cells.^{33,34} However, given biophysical differences between transformed and healthy cells we hypothesize this disease can be identified by DC. Samples in which reactive mesothelial cells were observed by cytology had corresponding deformability cytometry profiles with a population of large (>15 μm) cells with a moderate deformability (D: 1.2-1.4). This specific pattern is observed in 100% (25 of 25) of all cases with noted benign or reactive mesothelial subpopulations. In a confirmed mesothelioma case, the DC profile (Fig. 9) displays an absence of these large moderately deformable cells but the presence of large softer population (D: 1.4-2.0). As we only collected one sample with a mesothelioma outcome, further investigation is needed for this disease type.

Case study: leukemia

Five cases examined also were associated with leukemia or lymphoma outcomes (Fig. 10). These PF samples were harvested from patients with concurrent leukemia or near future (<1 year) diagnoses of leukemia. Leukemia disease types assayed include acute myeloid leukemia (AML), chronic myelogenous leukemia (CML), myelodysplastic syndrome (MDS), and lymphoma. In the case of AML, the DC profile is uniquely distinctive showing a larger size and increased deformability shift in the major leukocyte population. In the first AML case, this DC assayed this specimen 3 months prior to a follow-up procedure that confirmed the disease. Comparing this profile to in vitro HL-60 myeloid leukemia cell lines shows a similar characteristic features – a highly deformable population at the 13-16 μm size range. The chronic myelogenous leukemia case had similarities to the second acute myeloid leukemia. Cytology

analysis suggested this second population of large (16-25 μm) and moderate deformability (1.2-1.8), are a subpopulation of histiocytes. However, the DC profiles rarely observed such a distinctive second population in CMI or NFMC cases. Lastly, the myelodysplastic syndrome and lymphomas have large scatters into the large and highly deformable regions, with feature similar to CMI profiles.

Case study: inflammation states

Mechnophenotyping also exhibits sensitivity to inflammation states. Both AI and CMI responses have distinctive profile features that can be used to monitor inflammatory response.²⁸ Figure 11 examines inflammatory disease DC profiles in detail. In PF of patients with diseases triggering an AI response, including sepsis, acute pneumonia, and tissue injury; the corresponding DC profile shows features of AI - small populations with scatter in the deformability measurement (Fig. 11A). In PF of patients with chronic kidney and liver failures and chronic pneumonia, a chronic inflammatory response is elicited. DC profiles of these patients' PF exhibit similarities to other CMI cases. Note the profiles lack specificity for the originating disease; however, the differences between acute and chronic inflammation are distinctive. This ability to distinguish between AI and CMI cases suggests utility of this system for clinical diagnoses beyond malignancy diagnosis. The sensitivity of AI diagnosis was: 80% while that of CMI diagnosis was 92% using a threshold analysis based on similarities of profile features to the pooled AI or CMI cases.

Conclusion

Thoracentesis procedures are performed at a rate of greater than 1.5 million per year in the United States³⁵. Malignant pleural fluids are drained to relieve patients of discomfort and are also recognized for having clinical diagnostic value: to deduce etiology, diagnose progression of malignant diseases and monitor patient relapse. Conventionally, PF samples are analyzed by cytology with follow-up procedures including flow cytometry, immunohistochemistry, and further biopsies as required to reach a diagnosis. The burden of follow-up procedures and biopsies is a significant cost to the healthcare system. An accurate, low-cost, automated technique to pre-screen samples such that only a small subset of suspicious samples are further analyzed by manual approaches has the potential to reduce healthcare costs. Deformability cytometry can fill this role by providing a high-throughput label-free measurement of disease states with quantitative metrics indicating the confidence in the diagnostic prediction. In using this system in prescreening roles for pleural fluid analysis, this tool is predicted to eliminate approximately 56% of the workload for cytology and related follow-up procedures. Notably, the specimens used for this dataset were analyzed at the UCLA Department of Pathology & Laboratory Medicine by highly experienced staff including cytopathologist, cytotechnicians, and lab technicians. Advantages of DC as a pre-screening tool can be expected to have even higher workload reduction impact in limited resource hospitals. Further benefits of DC quantification of specimens are advantages in archiving patient data compared to conventional slide based analysis. Currently slides are rarely imaged and digitally archived because of the large memory requirements for storing imaging data, whereas DC profiles are discrete representations of patient data in an information-rich format, easily stored and interpretable. Lastly, as DC profiles have readily recognizable disease specific features it will enable increased transparency of

patient data facilitating clinician collaborations. Combined with established label based methods, this technique has the potential to improve the speed and accuracy of cancer diagnosis, while simultaneously reducing costs to the healthcare system.

Material and Methods

Pleural Fluid preparation and analysis

Patient samples were initially collected for DC analysis from the UCLA Cytopathology Lab which arrived from patients at clinics from UCLA Ronald Reagan, UCLA Santa Monica, and other regional hospitals. Samples provided by cytopathology were remnants from thoracentesis following cytological examination and usually consisted of 10-50 mL. Patient pleural fluids samples harvested the within 24 hours of thoracentesis were obtained from Department of Pathology at UCLA processing patient samples from Ronald Reagan UCLA Medical Center, and Santa Monica UCLA Medical Center. For each sample cell blocks and cell smears were prepared by conventional methods for cytological analysis. Preparation for DC mechanical phenotyping samples were first processed to remove red blood cells and debris by a hypotonic lysis buffer (Roche, X). The remaining cells were resuspended in PBS at density between 200,000 and 300,000 cells/mL prior to DC assay.

Microfluidic device fabrication and device dimensions

Microfluidic devices were designed in AutoCAD (Autodesk, San Rafael, California, USA) and printed to transparency photomasks (CAD/Art Services, Inc., Bandon, Oregon, USA). Transferring the designs on the photomasks to a replica mold by spinning negative photoresist, SU-8 50 (MicroChem, Newton, Massachusetts, USA)] on a 4 inch silicon wafer at 4000 rotations per minute. The coated wafer was soft baked at 65°C for 5 minutes then 95°C for 15 minutes. The wafer was then exposed under near UV at 8.0 mW/cm² for 30 seconds. A post exposure bake of the wafer was carried out at 65°C for 2 minutes then at 95°C for 3.5 minutes.

The unexposed photoresist was developed in SU-8 Developer (MicroChem) until an isopropyl alcohol rinse produced no white film. The height of the resulting features was characterized by a surface profiler. The height and width of the immediately before the extensional flow junction was 28 μm and 67 μm , respectively. Devices were then casted using Sylgard 184 Silicone Elastomer (Dow Corning, Midland, Michigan, USA), polydimethylsiloxane (PDMS), mixed 10 parts base to 1 part curing agent. The poured mold was degassed by 30 minutes followed by a 3 hour curing at 65°C. Devices were then cut from the mold, input and output punched, air plasma cleaned for 30 second, and bonded to plasma activated glass slide. Devices were then placed in the 65°C oven for 3 hours prior to use.

Device operation

Pleural fluid cell suspensions were prepared as described above. At the optimal cell density between 200,000 and 500,000 cells/mL cell to cell collision events are minimized. The suspension were loaded into 3 mL plastic syringes (BD, X), connected with a 25 gauge luer stub (Instech Laboratories, Inc., Plymouth Meeting, Pennsylvania, USA) and terminated with a short length of PEEK tubing (Upchurch Scientific, Oak Harbor, Washington, USA) with an inner diameter of 0.02 inches and an outer diameter of 0.0313 inches. Equal tubing lengths were inserted into the outlets with free ends directed into a waste receptacle. The syringe was loaded onto a PHD 2000 syringe pump (Harvard Apparatus, Holliston, Massachusetts, USA) and set to inject at a flow rate optimized for the device. A volumetric flow rate of 900 $\mu\text{L}/\text{min}$ was optimal for prepared pleural fluid samples. At the start of each run, devices was primed for 20 seconds at the operational flow rate to allow for the fluidic capacitance to stabilize. Cells are stretched when it reached the center of the extensional flow.

Data acquisition and processing

Video data was captured using a Vision Research Phantom v7.3 high speed camera at 140,000 fps, with a 1 us exposure. Videos were contrast enhanced prior to image analysis. The automated image analysis is built using MATLAB v2009a (MathWorks, Natick, Massachusetts, USA) and processed on the UCLA Hoffman 2 Cluster. We have previously described the image analysis process (PNAS paper). Briefly, for each cell the size is extracted upstream of the junction tracked and upon reaching the junction proximity and until it tracks out of the field-of-view deformability measurements are obtained. Diameters of the cell are extracted by a polar to Cartesian coordinate transformation where major and minor axis of the cells are extracted at $90^\circ \pm 30^\circ$ and $0^\circ \pm 30^\circ$, respectively. The deformability parameter reported here is defined as the ratio of major to minor axis. Post-processing scatter plots were created using dscatter function (Creator: X, MathWorks File Exchange)

Statistical and decision analysis

Sample analysis for characterization of NFMC, AI, and CMI used 90 of 119 samples. The remaining 29 samples were of MPF (n=17) or had both AI and CMI disease conditions reported (n=12).

Standard clinical outcome profiles were created by pooling 10 representative patient cases for each clinical outcome: NFMC, AI, CMI, and MPF. In creating the standard clinical outcome profiles, the cell counts per patient case were normalized. Upper right quadrant gating was created by using the 95% confidence interval of the mean on NFMC cases. The DC-A and DC-B decision analysis was trained on nine parameters based on DC profile features. The

algorithm assigns threshold based scores to each condition, where the scores sum determines a MPF or NFMC diagnosis (S. Fig. 2).

Specimen selection criterion

In the main sample set of 119, we omitted from the analysis 5 malignant samples collected over a 5 week span due to specimen collection error. Analysis of these samples had 0% sensitivity for malignant pleural fluids with DC-A. We suspect this is due to sedimentation as larger cells were not observed in high frequency in any of the confirmed malignant samples as we expected from the cytology cell smears. Additionally, 28 samples beyond the 24 hours cut-off criteria were omitted due to sample degradation. Some samples do maintain cellular integrity up to 48 hours, but degrade substantially beyond this time point (S. Fig 1). From this main set of 119 samples, 101 samples were analyzed in which cytology + follow-up procedures agreed well with concurrent disease states. Within the main set, 18 samples had cytology + follow-up procedures discordant with underlying disease states, and were analyzed separately (Fig. 8).

Figures

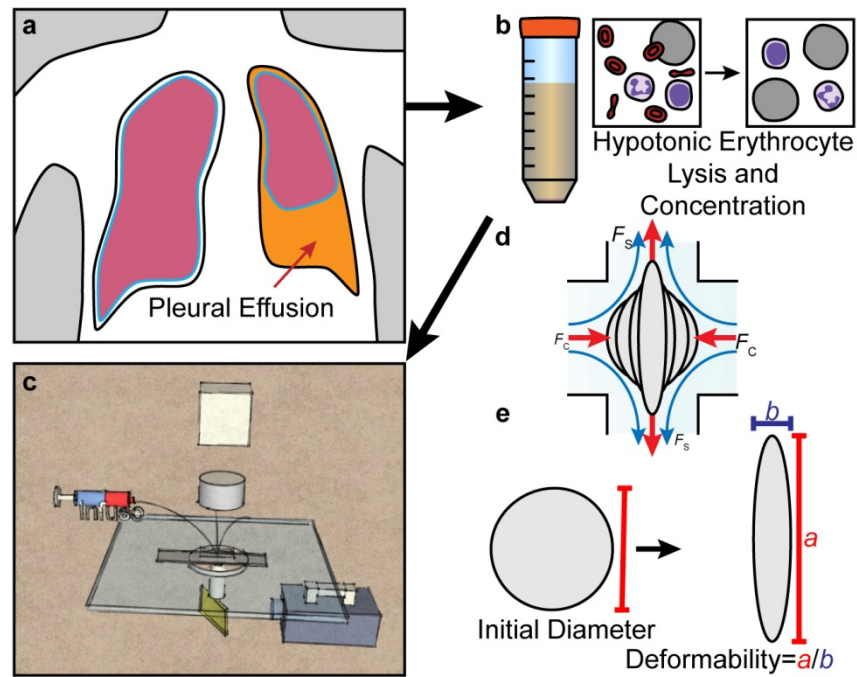


Figure 1 Deformability Cytometry device operations. (A) Pleural fluid samples are collected from the pleural cavity. (B) Sample is then prepared for DC assay by RBC hypotonic lysis and concentration. (C) The sample is driven through the DC device and data is recorded by high-speed imaging. (D) The deformation contributed by F_c (compressive stress) and F_s (shear stress) forces on the cells. (E) The reported parameters are the size (initial diameter) and deformability (D : the ratio of major/minor axes) extracted from the video data.

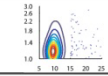
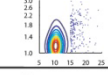
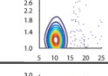
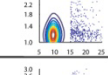
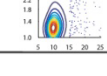
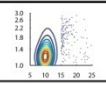
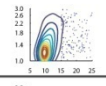
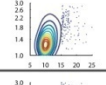
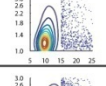
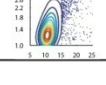
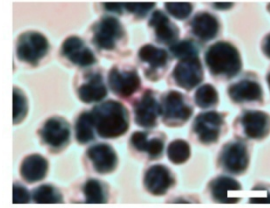
Pt. #	Cytology Analysis		DC Analysis	
	Technique	Cytology Outcome	Def. Size	DC Outcome
1	CS, CB	NFMC		NFMC
2	CS, CB, IHC, FC	NFMC		NFMC
3	CS, CB, FC	NFMC		NFMC, AI
4	CS, CB, FC	NFMC, RM		NFMC
5	CS, CB	NFMC		NFMC, AI

Figure 2 Cases that are negative for malignant cells (NFMC) exhibit a dominant non-activated leukocyte population. Comparative table of cytology methods and cytology outcomes and DC analyses and outcomes of 5 NFMC patients. Note additional follow-up performed by flow cytometry and immunohistochemistry in patients 2-4. CS – Cell Smear, CB – Cell Block, IHC, Immunohistochemistry, FC – Flow Cytometry, RM – Reactive Mesothelial Cells, AI – Acute Inflammation.

A

Pt. #	Cytology Analysis		DC Analysis	
	Technique	Cytology Outcome	Def. Size	DC Outcome
6	CS, CB	NFMC, AI (Pneumonia)		NFMC, AI
7	CS, CB	NFMC, AI (Pneumonia)		NFMC, AI
8	CS, CB, IHC	NFMC, AI (Pneumonia)		NFMC, AI
9	CS, CB	NFMC, AI (Unknown)		NFMC, AI
10	CS, CB	NFMC, AI (Pneumonia)		NFMC, AI

B



C

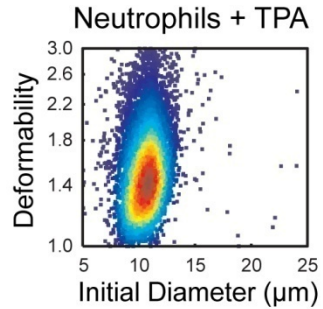
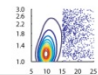
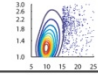
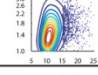
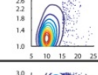
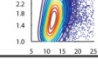
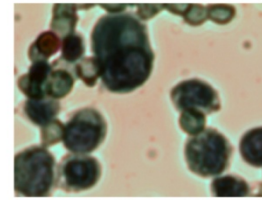


Figure 3 Acute inflammation (AI) cases exhibit activated neutrophil populations with increased spread in deformability. (A) Comparative table of cytology methods and outcomes and DC analyses and outcomes of 5 AI patients. (B) Cell smears and cell blocks of neutrophil dense samples. Scale bar 10 μm . (C) Activation of healthy donor neutrophils generates a biomechanical change similar to that seen in AI patient samples. CS – Cell Smear, CB – Cell Block, IHC, Immunohistochemistry, RM – Reactive Mesothelial, AI – Acute Inflammation.

A

Pt. #	Cytology Analysis		DC Analysis	
	Technique	Cytology Outcome	Def. / Size	DC Outcome
11	CS, CB	NFMC, CMI (Pneum.), RM		NFMC, CMI
12	CS, CB	NFMC, CMI (KD)		NFMC, CMI
13	CS, CB, IHC, FC	NFMC, CMI (Unkwn.), RM		NFMC, CMI
14	CS, CB, IHC, FC	NFMC, CMI (Unkwn.)		NFMC, CMI
15	CS, CB, FC	NFMC, CMI (Unkwn.)		NFMC, CMI

B



C

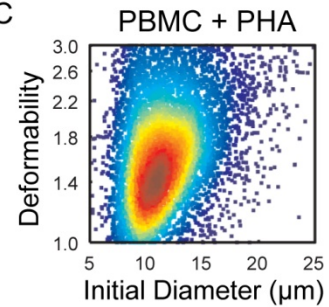


Figure 4 Chronic/mixed inflammation (CMI) cases exhibit more deformable activated lymphocyte populations. (A) Comparative table of cytology methods and outcomes and DC analyses and outcomes for 5 CMI patients. Note additional follow-up procedures in patients 13-15. (B) Cell smears and cell blocks of lymphocyte-dense samples. (C) PHA activation of healthy donor lymphocytes generates a similar profile as seen CMI patient samples. CS – Cell Smear, CB – Cell Block, IHC, Immunohistochemistry, RM – Reactive Mesothelial, CMI – Chronic/mixed Inflammation.

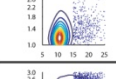
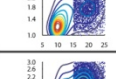
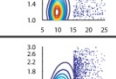
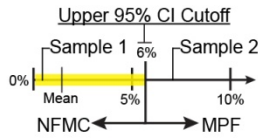
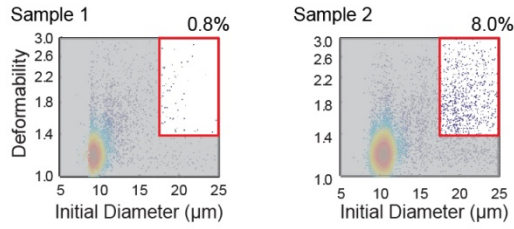
Pt. #	Cytology Analysis		DC Analysis	
	Technique	Cytology Outcome	Def. / Size	DC Outcome
16	CS, CB, IHC	MPF		MPF
17	CS, CB, IHC	MPF		MPF, AI, CMI
18	CS, CB, IHC	MPF		MPF, AI, CMI
19	CS, CB	MPF		MPF
20	CS, CB, IHC	MPF		MPF, CMI
21	CS, CB	MPF		MPF
22	CS, CB, IHC	MPF		MPF
23	CS, CB, IHC	MPF		MPF
24	CS, CB	MPF, AI (Pneum.), RM		MPF, AI
25	CS, CB, IHC	MPF, AI (Unkwn.), RM		MPF, CMI

Figure 5 Malignant pleural fluid (MPF) cases exhibit large and highly deformable subpopulations along with smaller and stiffer leukocyte populations using the DC-A analysis. CS – Cell Smear, CB – Cell Block, IHC, Immunohistochemistry, RM – Reactive Mesothelial, AI – Acute Inflammation, CMI – Chronic/mixed Inflammation.

A Large & Highly Deformable Quadrant Gating

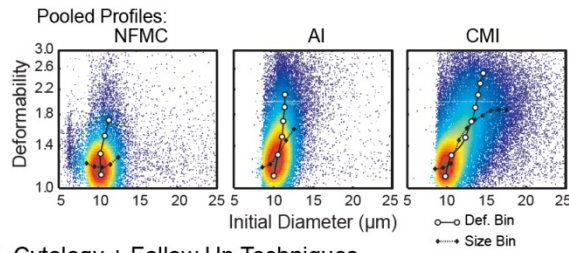


Cyto. + Follow up

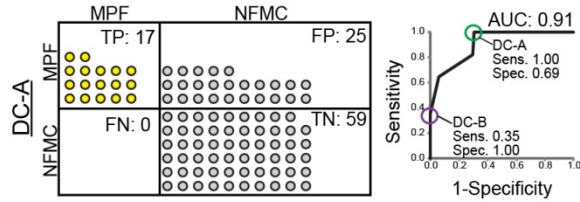
	MPF	NFMC
DC MPF	15	24
NFMC MPF	2	60

Sensitivity: 88% Specificity: 71%

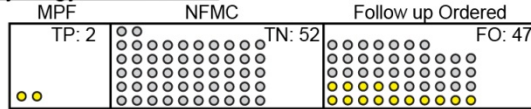
B Standard Curve Fit



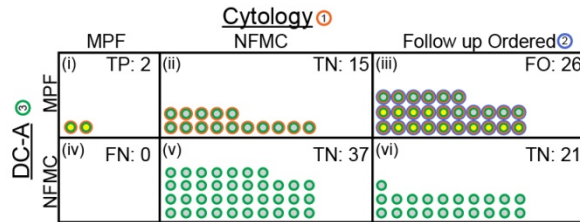
C Cytology + Follow Up Techniques



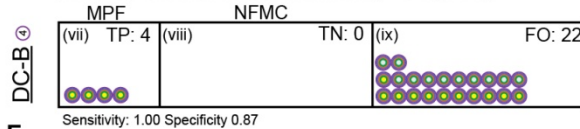
D Cytology Performance



E DC-Assisted Cytology Performance



Follow up Ordered Cases Examined by DC-B (N=26)



F Workload Analysis

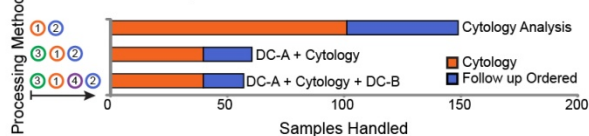


Figure 6 Algorithmic decision analysis for identifying malignant pleural fluids and hypothetical cytology workload reduction workload reduction. (A) Strategy using quadrant analysis for large ($>17\ \mu\text{m}$) and highly deformable cells ($D>1.4$) (B) Standard curve of pooled common outcome profiles, $N=6$ patient samples for each standard profile. (C) Deformability cytometry decision analysis performance. DC compared to gold standard of cytology and follow-up procedures. Receiver operating curve shows two operational points, DC-A and DC-B, to leverage high sensitivity or high specificity detection. (D) Cytology standalone performance without follow-up procedures. (E) DC performance by first pre-screening with the high sensitivity DC-A analysis method, followed by cytology stratification of samples. High specificity DC-B analysis reexamines follow-up requests by cytology. (F) Total workload reduction of 56% using DC to pre-screen samples pre-cytological analysis and pre-follow-up analysis. TP – True Positive, TN – True Negative, FN – False Negative, FO – Follow-up Ordered.

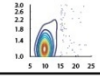
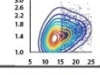
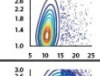
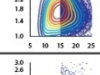
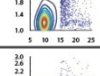
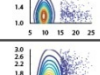
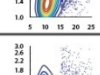
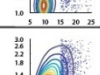
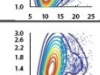
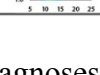
Pt. #	Cytology Analysis		DC Analysis		Final Outcome
	Technique	Cytology Outcome	Def. Size	DC Outcome	
26	CS, CB, IHC	AC		MPF	MPF
27	CS, CB, Bx, IHC	AC		MPF	MPF
28	CS, CB, FC	AC		MPF, AI	MPF
29	CS, CB, IHC	AC		MPF	MPF
30	CS, CB, FC	AC		NFMC	NFMC, RM
31	CS, CB, IHC	AC		NFMC	NFMC, RM
32	CS, CB, IHC	AC		NFMC, AI, CMI	NFMC, CMI, RM
33	CS, CB, IHC	AC		MPF	NFMC, RM
34	CS, CB, IHC	AC		MPF, CMI	NFMC, CMI
35	CS, CB, IHC	AC		MPF, CMI	NFMC, CMI, RM

Figure 7 Cases receiving Atypical cell (AC) diagnoses by cytology. DC-A decision analysis diagnoses these cases with 70% accuracy when compared to final clinical outcomes arrived at post- follow-up procedures.

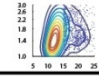
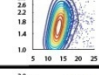
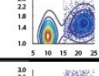
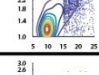
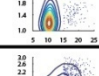
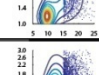
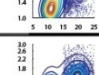
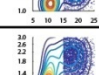
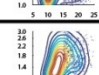

Pt. #	Concurrent Disease	Cytology Analysis		DC Analysis	
		Technique	Cytology Outcome	Profile	DC Outcome
36	MDS	MBx, CS, CB, FC	NFMC, CMI, RM		MPF, CMI
37	AML	CS, CB, FC	NFMC, CMI		MPF
38	AML	MBx, CS, CB, IHC, FC	NFMC, CMI		MPF
39	Myeloma	CS, CB	NFMC, CMI, RM		MPF, CMI
40	Small cell carcinoma	CS, CB	NFMC		MPF, AI
41	GI carcinoma	CS, CB, IHC	NFMC		MPF
42	Mesothelioma	CS, CB, IHC	NFMC, CMI, RM		MPF, CMI
43	Myelogenous leukemia	CS, CB, IHC, FC	NFMC		MPF
44	Prostate cancer	CS, CB, IHC	NFMC		MPF
45	Breast cancer	CS, CB, IHC	NFMC, CMI		MPF

Figure 8 Concurrent disease cases. Cytology and DC outcomes were discordant when known concurrent malignant disease was present. MBx – multiple biopsies.

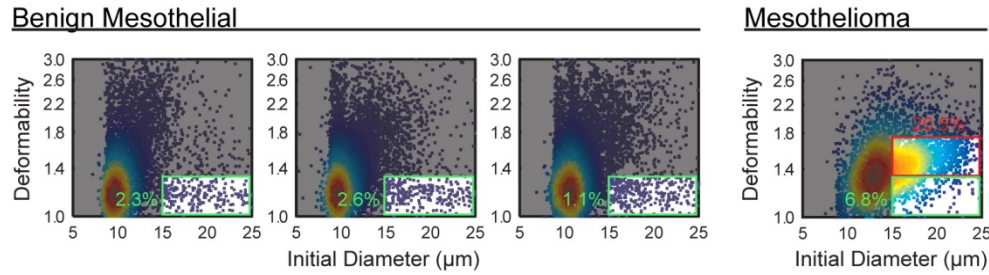


Figure 9 Comparison between benign and malignant mesothelial subpopulations. Benign cases exhibit a subpopulation residing in large (15 - 25 μm) and stiff ($D: < 1.4$) region. Malignant mesothelioma case shifts the large subpopulation to $D: 1.4 - 1.8$.

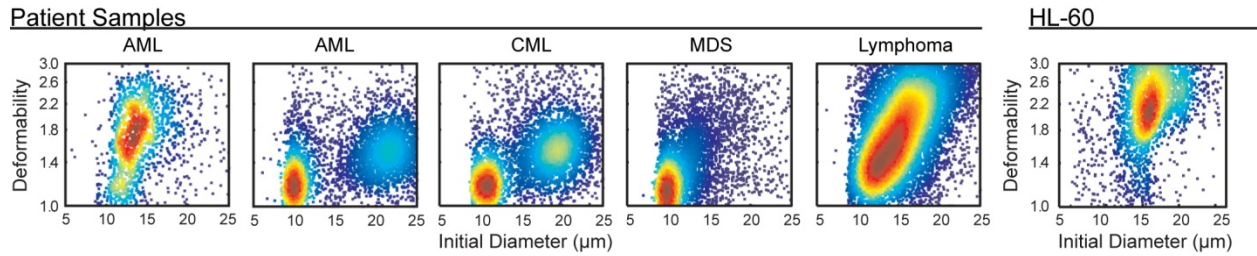


Figure 10 Pleural fluids with leukemia and lymphoma diseases. AML: Acute myeloid leukemia, CML, chronic myelogenous leukemia, MDS: myelodysplastic syndrome.

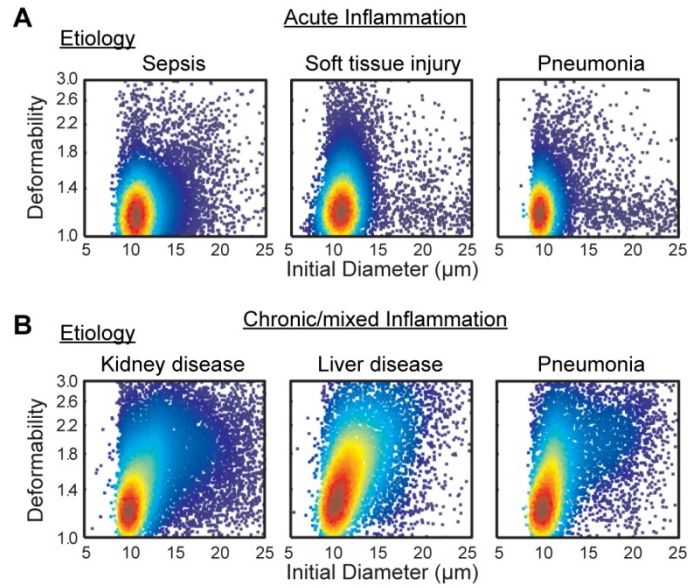
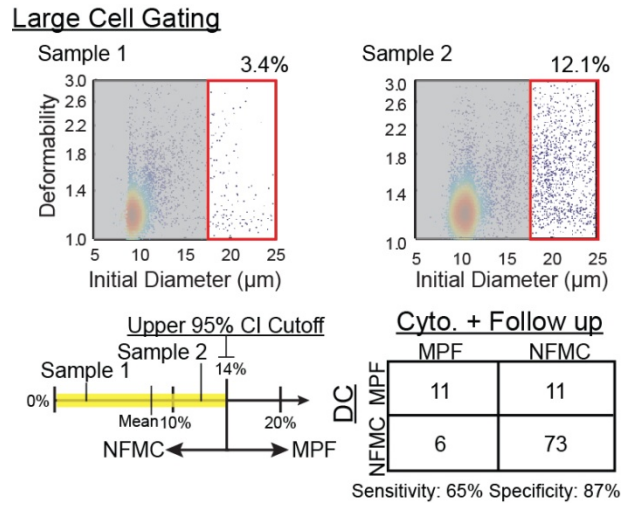
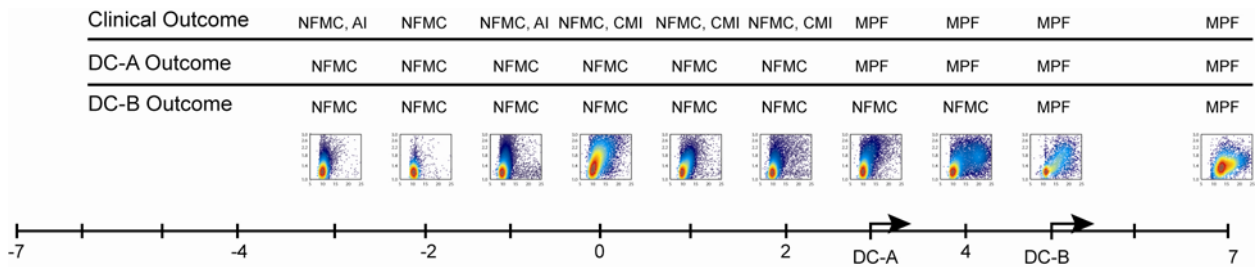


Figure 11 DC profiles of disease states associated with acute and chronic inflammatory responses. (A) Sepsis, soft tissue injury, and acute pneumonia, induces acute inflammatory responses, while DC profiles have characteristic features of acute inflammation. (B) Chronic diseases such as kidney and liver failure, chronic pneumonia, result in chronic inflammatory responses, in which DC profiles have characteristic features of chronic/mixed inflammation.

Supplementary Figures



Supplementary Figure 1 Large cell gating analysis. Profiles are gated at the $> 17 \mu\text{m}$ region. The threshold limit (14.1%) for determining NFMC or MPF uses the upper 95% confidence interval limit of the mean (8.3%).



Supplementary Figure 2 DC points based diagnosis. The points per case is determined by how each individual profile fits to standard cases. For DC-A, the points threshold is set at 2 where scores above than this value is marked as MPF.

Bibliography

1. Froudarakis, M. E. (2008). Diagnostic Work-Up of Pleural Effusions. *Respiration* 75:4–13. DOI:10.1159/000112221
2. Sahn, S. A. (1988). The Pleura. *Am. J. Respir. Crit. Care Med.* 138:184–234. DOI:10.1164/ajrcm/138.1.184
3. Bedrossian, C. W. M. (1998). Diagnostic problems in serous effusions. *Diagnostic Cytopathology* 19:131–137. DOI:10.1002/(SICI)1097-0339(199808)19:2<131::AID-DC14>3.0.CO;2-G
4. Light, R. W. (1997). Diagnostic principles in pleural disease. *Eur Respir J* 10:476–481
5. Sahn, S. A. (2008). The Value of Pleural Fluid Analysis. *The American Journal of the Medical Sciences* 335:7–15. DOI:10.1097/MAJ.0b013e31815d25e6
6. Antman, K. H., Blum, R. H., Greenberger, J. S., Flowerdew, G., Skarin, A. T. & Canellos, G. P. (1980). Multimodality therapy for malignant mesothelioma based on a study of natural history. *The American Journal of Medicine* 68:356–362. DOI:10.1016/0002-9343(80)90103-5
7. Elmes, P. C. & Simpson, M. J. C. (1976). The Clinical Aspects of Mesothelioma. *QJM* 45:427–449
8. Light, R. W., Erozan, Y. S. & Ball, W. C. (1973). Cells in Pleural Fluid: Their Value in Differential Diagnosis. *Archives of Internal Medicine* 132:854–860. DOI:10.1001/archinte.1973.03650120060011
9. Moriarty, A. T., Wiersema, L., Snyder, W., Kotylo, P. K. & McCloskey, D. W. (1993). Immunophenotyping of cytologic specimens by flow cytometry. *Diagnostic Cytopathology* 9:252–258. DOI:10.1002/dc.2840090303
10. Rijken, A., Dekker, A., Taylor, S., Hoffman, P., Blank, M. & Krause, J. R. (1991). Diagnostic value of DNA analysis in effusions by flow cytometry and image analysis. A prospective study on 102 patients as compared with cytologic examination. *Am. J. Clin. Pathol.* 95:6–12
11. Saha, I., Dey, P., Vhora, H. & Nijhawan, R. (2000). Role of DNA flow cytometry and image cytometry on effusion fluid. *Diagn. Cytopathol.* 22:81–85

12. Fetsch, P. A. & Abati, A. (2001). Immunocytochemistry in effusion cytology. *Cancer Cytopathology* 93:293–308. DOI:10.1002/cncr.9044
13. King, J. E., Thatcher, N., Pickering, C. a C. & Hasleton, P. S. (2006). Sensitivity and specificity of immunohistochemical markers used in the diagnosis of epithelioid mesothelioma: a detailed systematic analysis using published data. *Histopathology* 48:223–232. DOI:10.1111/j.1365-2559.2005.02331.x
14. Kipp, B. R. *et al.* (2004). A Comparison of Routine Cytology and Fluorescence in situ Hybridization for the Detection of Malignant Bile Duct Strictures. *The American Journal of Gastroenterology* 99:1675–1681. DOI:10.1111/j.1572-0241.2004.30281.x
15. Cross, S. E., Jin, Y.-S., Rao, J. & Gimzewski, J. K. (2007). Nanomechanical analysis of cells from cancer patients. *Nat Nano* 2:780–783. DOI:10.1038/nnano.2007.388
16. Remmerbach, T. W., Wottawah, F., Dietrich, J., Lincoln, B., Wittekind, C. & Guck, J. (2009). Oral Cancer Diagnosis by Mechanical Phenotyping. *Cancer Res* 69:1728–1732. DOI:10.1158/0008-5472.CAN-08-4073
17. Lekka, M. & Laidler, P. (2009). Applicability of AFM in cancer detection. *Nat Nano* 4:72. DOI:10.1038/nnano.2009.004
18. Rosenbluth, M. J., Lam, W. A. & Fletcher, D. A. (2006). Force Microscopy of Nonadherent Cells: A Comparison of Leukemia Cell Deformability. *Biophysical Journal* 90:2994–3003. DOI:10.1529/biophysj.105.067496
19. Pajerowski, J. D., Dahl, K. N., Zhong, F. L., Sammak, P. J. & Discher, D. E. (2007). Physical plasticity of the nucleus in stem cell differentiation. *Proceedings of the National Academy of Sciences* 104:15619–15624. DOI:10.1073/pnas.0702576104
20. Hochmuth, R. M. (2000). Micropipette aspiration of living cells. *Journal of Biomechanics* 33:15–22. DOI:10.1016/S0021-9290(99)00175-X
21. Rosenbluth, M. J., Lam, W. A. & Fletcher, D. A. (2008). Analyzing cell mechanics in hematologic diseases with microfluidic biophysical flow cytometry. *Lab Chip* 8:1062. DOI:10.1039/b802931h

22. Bow, H., Pivkin, I. V., Diez-Silva, M., Goldfless, S. J., Dao, M., Niles, J. C., Suresh, S. & Han, J. (2011). A microfabricated deformability-based flow cytometer with application to malaria. *Lab Chip* 11:1065–1073. DOI:10.1039/c0lc00472c
23. Chen, J. *et al.* (2011). Classification of cell types using a microfluidic device for mechanical and electrical measurement on single cells. *Lab Chip* 11:3174–3181. DOI:10.1039/C1LC20473D
24. Abkarian, M., Faivre, M. & Stone, H. A. (2006). High-speed microfluidic differential manometer for cellular-scale hydrodynamics. *PNAS* 103:538–542. DOI:10.1073/pnas.0507171102
25. Katsumoto, Y., Tatsumi, K., Doi, T. & Nakabe, K. (2010). Electrical classification of single red blood cell deformability in high-shear microchannel flows. *International Journal of Heat and Fluid Flow* 31:985–995. DOI:10.1016/j.ijheatfluidflow.2010.02.019
26. Guck, J. *et al.* (2005). Optical Deformability as an Inherent Cell Marker for Testing Malignant Transformation and Metastatic Competence. *Biophysical Journal* 88:3689–3698. DOI:10.1529/biophysj.104.045476
27. Forsyth, A. M., Wan, J., Ristenpart, W. D. & Stone, H. A. (2010). The dynamic behavior of chemically ‘stiffened’ red blood cells in microchannel flows. *Microvascular Research* 80:37–43. DOI:10.1016/j.mvr.2010.03.008
28. Gossett, D. R., Tse, H. T. K., Lee, S. A., Ying, Y., Lindgren, A. G., Yang, O. O., Rao, J., Clark, A. T. & Carlo, D. D. (2012). Hydrodynamic stretching of single cells for large population mechanical phenotyping. *PNAS* 109:7630–7635. DOI:10.1073/pnas.1200107109
29. Antony, V. B., Loddenkemper, R., Astoul, P., Boutin, C., Goldstraw, P., Hott, J., Rodriguez Panadero, F. & Sahn, S. A. (2001). Management of malignant pleural effusions. *European Respiratory Journal* 18:402–419
30. Pettersson, T. & Riska, H. (1981). Diagnostic Value of Total and Differential Leukocyte Counts in Pleural Effusions. *Acta Medica Scandinavica* 210:129–135. DOI:10.1111/j.0954-6820.1981.tb09788.x
31. Brown, M. J., Hallam, J. A., Colucci-Guyon, E. & Shaw, S. (2001). Rigidity of Circulating Lymphocytes Is Primarily Conferred by Vimentin Intermediate Filaments. *The Journal of Immunology* 166:6640–6646

32. Worthen, G., Schwab, B., Elson, E. & Downey, G. (1989). Mechanics of stimulated neutrophils: cell stiffening induces retention in capillaries. *Science* 245:183–186. DOI:10.1126/science.2749255
33. Renshaw, A. A., Dean, B. R., Antman, K. H., Sugarbaker, D. J. & Cibas, E. S. (1997). The Role of Cytologic Evaluation of Pleural Fluid in the Diagnosis of Malignant Mesothelioma. *Chest* 111:106–109. DOI:10.1378/chest.111.1.106
34. Sahn, S. A. (1998). Malignancy metastatic to the pleura. *Clin. Chest Med.* 19:351–361
35. Light, R. W. (Lippincott Williams & Wilkins: 2007). *Pleural Diseases*.